NONLINEAR PREDICTION OF THERMALLY INDUCED ROTOR

INSTABILITY (MORTON EFFECT) AND EXPERIMENT VERIFICATION

A Dissertation

by

XIAOMENG TONG

Submitted to the Office of Graduate and Professional Studies of
Texas A&M University
in partial fulfillment of the requirements for the degree of

DOCTOR OF PHILOSOPHY

Chair of Committee,	Alan Palazzolo
Committee Members,	Won-Jong Kim
	Steve Suh
	Jeffrey Falzarano
Head of Department,	Andreas A. Polycarpou

May 2018

Major Subject: Mechanical Engineering

ABSTRACT

The Morton effect (ME) is a thermally induced rotor instability problem that most commonly appears in rotating shafts with large overhung masses and supported by fluid film bearings. The time-varying thermal bow, due to the asymmetric journal temperature distribution, may cause intolerable synchronous vibrations that exhibit a hysteresis behavior with respect to rotor speed. First discovered by Morton in the 1970s, and theoretically analyzed by Keogh and Morton in the 1990s, the ME is still not fully understood by industry and academia experts. Traditional rotordynamic analysis generally fails to predict the potential existence of ME induced instability in the design stage or troubleshooting process, and the induced excessive rotor vibrations cannot be effectively suppressed through conventional balancing, due to the continuous fluctuation of vibration amplitude and phase angle.

The early ME prediction methodologies adopt three assumptions which simplify the ME analysis and meanwhile reduce its accuracy in predicting the ME response. (1) The ME is assumed to be static and speed-dependent and thus its stability can be analyzed with the classic control theories in the frequency (speed) domain. Nevertheless, the ME is proven to be highly transient and process-oriented, and not only the operating speed but also the transient speed acceleration can cause instability. (2) The thermal bow effect is only considered at the rotor overhung side and is simplified with thermal imbalance, which neglects the ME induced thermal bending moment. (3) Early ME prediction only focuses

on the single rotor-bearing side and neglects the coupled effect on rotordynamics and bearing behavior from the other side.

The assumptions above are abandoned in the current dissertation and replaced with the high-fidelity transient finite element analysis (FEA). The FEA is based on the recent thermo-elasto-hydro-dynamic bearing analysis and featured with (1) the nonlinear transient prediction of ME in the time domain through numerical integration, (2) analyzing both rotor-bearing sides to simultaneously account for the overall thermal bow effect, and thus the coupled rotordynamics effect from both rotor-bearing sides can be considered, and (3) the bowed rotor method, which also considers the thermal bow at the rotor midspan besides the rotor ends. The thermal bending moment is also included in the rotordynamics model, making this method more accurate than the traditional thermal imbalance method.

Moreover, the ME testing rig is designed to measure the temperature distribution with 20 sensors across the journal circumference and record the peak-peak temperature difference (ΔT) with respect to various operating conditions. Supply oil temperatures of 28℃, 41℃ and bearing eccentricity of 0, 32%C_b are tested with rotating speed up to 5500 rpm. The journal ΔT is found to increase almost linearly with speed up to 5500 rpm, slightly increase with eccentricity from 0 to 32%C_b, and decrease by nearly 20% by raising the supply temperature from 28℃ to 41℃ due to reduced viscosity. The proposed high-fidelity ME analysis is applied to predict the journal temperature distribution against the measurements, and predictions are also compared with the simplified ME analysis proposed in earlier literature. The high-fidelity model demonstrates a better accuracy in predicting the maximum rotor temperature Max(T), the peak-peak temperature difference

$\text{Max}(\Delta T)$, and the phase lag between the high spot and hot spot compared with the simplified ME analysis.

DEDICATION

The dissertation is dedicated to my parents, Mr. Biao Tong and Ms. Jiang Shen, who raised me up and gave me the spirit, courage, curiosity and optimism to finish my Ph.D. career.

ACKNOWLEDGEMENTS

CONTRIBUTORS AND FUNDING SOURCES

Contributors

The work was supervised by a dissertation committee consisting of Professors Alan Palazzolo and Won-Jong Kim and Steve Suh of the Department of Mechanical Engineering and Professor Jeffrey Falzarano of the Department of Ocean Engineering.

All work for the dissertation was completed independently by the student.

Funding Sources

NOMENCLATURE

ME   Morton effect

NDE   Non-drive end

DE   Drive end

DS   Disk skew

SM   Separation margin

MCOS   Maximum continuous operating speed

RB   Residual bow

SOWM   Single-overhung-wise method

TR   Thermal rotor

$A_{\text{n\_tbow}}$ Amplitude of the nodal thermal bow

$A_{\text{n\_pbow}}$ Amplitude of the nodal permanent bow

a_{mn} Coefficient of Fourier series

C_b Radial bearing clearance

C_p Radial pad clearance

$\boldsymbol{C}_B$ Damping matrix of the fluid film bearing

$\boldsymbol{C}_R$ Rotor damping matrix

C_{rot} Rotor damping matrix including linear bearing/coupling damping

F Global resultant force vector

$\hat{F}$ Complex force vector

F_{all}	Relative resultant force vector
$\boldsymbol{F}_{im}$	Mechanical imbalance force
F_{gyro}	Gyroscopic force
$\boldsymbol{F}_{\text{brg}}$	Fluid film bearing force
F_{ext}	External forces on the rotor
h_{min}	Minimum film thickness in the fluid film bearing
h_0	Allowed minimum film thickness in the fluid film bearing
h	Film thickness in the fluid film bearing
I_p	Polar moment of inertial
I_t	Transverse moment of inertial
$\boldsymbol{K}_R$	Rotor stiffness matrix
$\boldsymbol{K}_B$	Stiffness matrix of fluid film bearing
K_{rot}	Rotor stiffness matrix including linear bearings/couplings stiffness
$\boldsymbol{M}_R$	Rotor mass matrix
M_{rot}	Global rotor mass matrix
R_{brg}	Journal radius
ΔT	Temperature difference across the journal circumference
T_A	Steady component of journal temperature
$T_J(r, \theta, \tau)$	Journal temperature (radius, circumference, time)
T_{max}	Maximum temperature in lubricant
T_0	Allowed maximum temperature in lubricant

TPJB	Tilting pad journal bearing
T_{ref}	Reference temperature
$\max(T)$	Peak journal circumferential temperature relative to supply temperature
$\max(\Delta T)$	Peak-peak temperature difference across the journal circumference
U	Nodal absolute displacement including bow vector and skewed angle
U_{bow}	Resultant bow vector
U_{tbow}	Thermal bow vector
U_{pbow}	Permanent bow vector
U_{skew}	Skewed angle vector
U_r	Relative displacement vector
$\widehat{U}_r$	Complex relative displacement vector
$\widehat{U}_{\text{bow}}$	Complex rotor bow vector
$\widehat{U}_{\text{skew}}$	Complex disk skew vector
x_n	Nodal displacement in x direction
y_n	Nodal displacement in y direction
$x_{\text{n\_bow}}$	Nodal bow displacement in x direction
$y_{\text{n\_bow}}$	Nodal bow displacement in y direction

Greeks

μ	Lubricant viscosity

μ_{ref}	Viscosity at reference temperature
$\widetilde{\mathbf{\Psi}}_{Ct}$	Rotor thermal bow
$\widetilde{\mathbf{\Psi}}_{Cb}$	Initial rotor bow
$\boldsymbol{\chi}_T$	Transient rotor deflection
$\boldsymbol{\chi}_B$	Transient rotor bow due to Morton effect
Ω	Rotor speed
ω	Spinning speed
θ_p	Pivot angular position
θ_{xn}	Nodal angular displacement in x direction
θ_{yn}	Nodal angular displacement in y direction
θ_{xn_bow}	Nodal bow angle in x direction
θ_{yn_bow}	Nodal bow angle in y direction
φ_{n_tbow}	Phase of the nodal thermal bow
φ_{n_pbow}	Phase of the nodal permanent bow
Φ_{n_tbow}	Amplitude of the nodal thermal bow angle
Φ_{n_pbow}	Amplitude of the nodal permanent bow angle
ψ_{n_tbow}	Phase of the nodal thermal bow angle
ψ_{n_pbow}	Phase of the nodal permanent bow angle
ϕ	Phase lag between the hot spot and high spot
λ	Mixing coefficient

TABLE OF CONTENTS

LIST OF FIGURES

Page

xix

LIST OF TABLES

1 INTRODUCTION[*]

Most high performance commercial machinery operates on fluid-film bearings due to the lifetime requirements as well as combinations of large rotor diameter and high running speed. The wedge-shaped lubricant film develops pressure to lift the rotating shaft and generates heat due to viscous shearing. The rising temperature of the lubricant reduces its viscosity and also heats the journal and bearing, which induces thermal expansion and affects the operating bearing clearance C_b [1, 2]. The shaft has long been assumed to be isothermal until recently, and engineers find that under certain conditions significant temperature difference (ΔT) can develop across the journal circumference, bending the shaft and leading to potential instability with excessive vibrations. This section is dedicated to give a detailed introduction of Morton effect causes, practical solutions in real cases, measurements and prediction.

1.1   Causes of Morton Effect

The thermal-hydrodynamic analysis of the journal bearing was experimentally performed by Dowson and March in 1966 [3], and the cyclic change of shaft surface temperature varied between 1^oC to 2^oC. However, the rotor was still assumed to be an isothermal component within the bearing due to the small temperature variation. The pioneering works of Morton [4] and Hesseborn [5] found that the rotor asymmetrical

---

[*] Reprinted with permission from "A Review of the Rotordynamic Thermally Induced Synchronous Instability (Morton) Effect" by Tong, X., Palazzolo, A, and Suh, J., 2017. ASME. Appl. Mech. Rev., 69(6): 060801. Copyright 2017 by ASME.

heating may bend the rotor and cause thermally induced instability (Morton effect) under certain conditions. Since then, the Morton effect (ME) has been frequently reported and analyzed, especially in the overhung shaft supported by fluid film bearings. Note that early literature in rotordynamics also covered examples of rub-induced spiral vibration effects, where synchronous vibration amplitude and phase varied slowly with time. The source of the spiral vibrations in these papers [6-9] was a direct contact rub of the shaft with seals or bearings causing localized, asymmetric heating of the shaft. The ME is distinguished from this by the heating source being the lubricant film in a bearing. Fig. 1-1 illustrates the ME publication quantity from 1975 to 2016, which has integrated the summary of de Jongh [10] and Panara [11] and indicates a clear upswing in academic research.
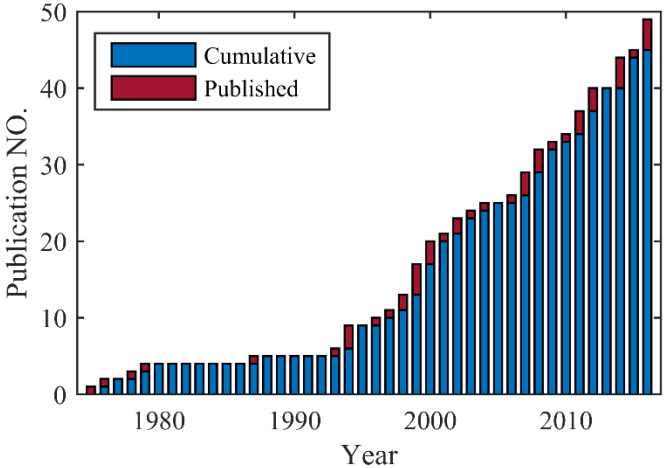
Fig. 1-1 Rotor thermal instability technical publications.

The Morton effect (ME) is in essence caused by the non-uniform viscous shearing inside the fluid film bearing, which leads to the development of temperature difference (ΔT) across the journal circumference, although the traditional bearing literature generally assumes that the rotor is isothermal. As shown in Fig. 1-2, the rotor has zero-ΔT across the journal circumference initially. Due to the mechanical imbalance or rotor residual bows, the journal may execute synchronous orbiting inside the fluid film bearing. The high spot, which has the minimum time-averaged film thickness in one orbit generally experiences more oil viscous shearing than other locations across the journal circumference. Step 1 in Fig. 1-2 illustrates a forward case for the synchronous orbit, although the backward orbit may also lead to non-even viscous shearing but with less intensity. This non-uniform viscous shearing will heat the rotor unevenly and cause ΔT across the journal circumference, as shown in Step 2. The hot spot, characterized with the highest temperature, is close to the high spot but is reported to lag the high spot in a range of 0° to 60° [12, 13]. The rotor ΔT will generate thermal bow in the shaft, and when the shaft is featured with big overhung wheels or couplings, the thermal bow can cause large equivalent imbalance, shown in Step 3. Under certain conditions, the resultant imbalance from both mechanical and thermal aspects will increase the journal orbit and cause higher journal ΔT, acting like a positive feedback loop until the rotor is tripped with excessive vibration. Most instability cases caused by the ME are reported in overhung machines supported by fluid-film bearings, and Table 1-1 gives an overview of different rotor types based on de Jongh's summary [10] and recent case studies.
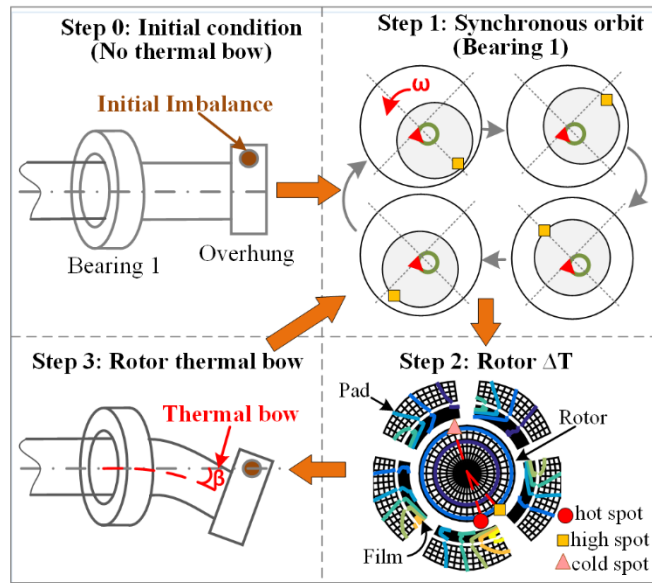
Fig. 1-2 Causes of Morton Effect.

Table 1-1 Rotor configurations from case studies

Rotor Configuration	Description	Cases
1.	2 overhung couplings (drive-through)	de Jongh [12]
2.	Single overhung wheel	Berot [14], Kocur [15], de Jongh [16], Kirk [17], Lorenz [18], Panara [11]
3.	Double overhung wheels	Faulkner [19], Schmied [20]
4.	1 overhung coupling	Kocur [15]
5.	Integrally geared, 1 overhung wheel	Carrick [21]
6.	Integrally geared, 2 overhung wheels	Marscher [22]

1.2   Symptoms of Morton Effect

Most ME induced instability cases are reported in the overhung machines supported by fluid film bearings, however, Guo et al. [23] argued that theoretically the

4

mid-span rotor could also experience similar problems. Based on published case studies, the ME symptoms are summarized below.

1.2.1 Spirals in the 1X Filtered Polar Plot

Spiral vibration is one of the most recognizable features in the thermally induced instability problems. The spiral vibration is typically caused by the rotor ΔT, which may result in a fluctuating amplitude with continuously changing phase angle [14, 16, 20, 22]. The time period for a 360° phase angle change may last several minutes [20, 22], and thus makes it almost impossible to balance the shaft. Note that the spirals can also be caused by the light rubs between a rotor and a stator such as a labyrinth, and this phenomenon is called the "Newkirk effect" [6, 24]. In both ME and Newkirk effect, the 1X polar plot will show similar spiral vibrations at constant rotor speed due to a moving hot spot and consequent thermal shaft bending, making it quite difficult to distinguish one from the other. However, there are still some differences, e.g. generally, the ME only occurs in the fluid film bearing-supported system, while the Newkirk effect doesn't have this limitation. Also, due to the lubricant convection effect in the bearing, the hot spot in the ME usually lags the high spot, however, this cannot be practically recognized based on the rotor symptoms. Moreover, engineers argue that removing suspicious components including seals from the rotor is the most straightforward way to determine the existence of the Newkirk effect.

1.2.2 Hysteresis in the Coast-down Testing

Considering that the rotor thermal constant is much larger than the spinning revolution period [2, 25], the rotor temperature cannot change simultaneously with speed. If the journal ΔT has developed and the shaft has been thermally bent during the running up, when performing a quick coast-down testing, the rotor ΔT cannot instantaneously decrease, leading to hysteresis in its vibration profile, where the coast-down amplitude is much higher than the running-up.

1.2.3 Sensitivity to Running Conditions

Lots of case studies demonstrate that the ME can be quite sensitive to operating conditions. Slight adjustment of bearing clearance, oil temperature, overhung mass, etc., can effectively stabilize the ME or make it worse. Changing the operating conditions, on one hand, alters the system dynamic behaviors including critical speed locations, mode shapes and separation margin, and on the other hand, affects the system thermodynamics by changing the oil viscous shearing. Despite no universal adjusting criteria to cure the ME, published case studies and theoretical modeling results give valuable recommendations to help specify parameters for ME suppression. Childs [26], Tong [27, 28] and Suh [29] have conducted detailed parametric studies based on the published rotor models in terms of imbalance, bearing clearance, L/D ratio, etc.

1.3   Practical Solutions of Morton Effect

Early solutions of ME involves trial and error considering that ME is still a "not well known rotordynamic phenomenon" [10]. After realizing that it is in essence a thermally induced instability problem, great efforts are devoted to minimize the ΔT across the rotor circumference. Reported cures can be categorized into five groups.

(1) Retrofit the bearing geometries. This includes adjustment of bearing clearance, preload, pivot offset, L/D ratio, etc., and under certain situations, different bearing types can be selected. For example, de Jongh [16] reported that increasing the C_b from 0.19% to 0.22% (ratio defined by C_b/R_{brg}) could successfully suppress the vibration, while Corcoran [30] presented that reducing the C_b by 33% could suppress the rotor vibration but meanwhile caused overheating inside the bearing.

(2) Change the supplied lubricant properties, including oil temperature, viscosity. For example, Marscher and Illis [22] increased the oil temperature from 125^oF to 128^oF to reduce the oil viscous shearing.

(3) Optimize the rotor structure including overhung mass adjustment, rotor stiffening, imbalance reduction, etc. For example, Schmied [20] stiffened the rotor to increase the separation margin, and reduced both the bearing width and oil viscosity to reduce the heat generation.

(4) Install isolation components to prevent the heat flux into the journal, such as installing a heat barrier sleeve. For example, to solve the thermal bow induced instability problem in one offshore compressor, de Jongh [16] mounted a heat barrier sleeve on the

journal surface. Air gap was intentionally designed inside the sleeve to prevent the heat flow into the journal.

(5) Change the bearing loading condition and operating eccentricity. For example, varying mesh force in gear compressor pinions may change bearing loads significantly, which will affect the rotordynamic response. The bearing orbit is more centered in lightly loaded bearings and is believed to induce larger rotor ΔT by Kirk [31]. Schmied analyzed a relatively lightly loaded bearing with the ME instability in [20] but also mentioned that the hot spot induced spiral vibrations had been observed in highly loaded bearing with elliptic off-centered journal orbits. Tong and Palazzolo have also experienced ME instability in an integrally geared compressor, where the bearings were heavily loaded and the operating speed was quite low.

Some solutions are consistent among cases, while others can be exactly contradictory. Despite effectiveness in individual case, no universal guidelines have been proposed to help avoid the ME in the design or trouble shooting process. A dedicated section in the 2nd version of the American Petroleum Institute (API) rotordynamic tutorial [32] states "while synchronous thermal instability fits the classical definition of an unstable system, rotor stability codes are currently not used to predict its existence", indicating that the solutions are still under discussion in both academic and industrial field. Table 1-2 summarizes the ME solutions from case studies and theoretical predictions. Note that the solutions are based on each individual case and sometimes can be quite different or even contradictory between cases. For example, a lighter coupling mass was reported to suppress the ME [11, 12, 15], while Corcoran eliminated the ME by installing

a heavier coupling [30]; Marscher [22] and Tong [27] reported that increasing the supplying oil temperature could cure the ME, while Suh [29] found that decreasing the oil temperature was better; de Jongh [16] reported that increasing the C_b could mitigate the ME, while Corcoran [30] reported the opposite.

Table 1-2 Solutions of Morton Effect

Cases	Solution categories	Solution details
1994, de Jongh [12]	3	Reduce the coupling mass by 5 kg
1997, Faulkner [19]	1,5 (bearing undercut)	Add an undercut in the loaded bearing surface to increase operating eccentricity.
1997, Corcoran [30]	3	Install a heavier coupling; reducing C_b by 33% can suppress the vibration but meanwhile cause bearing overheating.
1998, de Jongh [16]	4	Install a heat barrier sleeve on the NDE journal surface
1999, Berot [14]	1	Reduce bearing L/D from 0.39 to 0.33 to make the stiffness orthotropic, orbit less circular and eccentricity higher.
2000, Kocur [15]	4 (1st case) 3 (2nd case)	Install the shaft barrier sleeve (1st); Reduce the coupling mass (2nd);
2003, Kirk [17]	1	Increase the C_b by 33%; reduce bearing L/D ratio from 0.476 to 0.25
2007, Marscher[22]	2	Increase oil temperature from 51.7^oC to 53.3^oC.
2008, Schmied [20]	1,2,3	Stiffen the rotor by increasing diameter; reduce bearing L/D from 0.6 to 0.4; reduce oil viscosity from 46 cSt to 32 cSt.
2011. Lorenz [18]	1	Replace the partial arc bearing with the 4-lobe fixed pad bearing.
2013, Kirk [33]	1,3,5	Modify bearings to run more eccentric; reduce bearing L/D ratio; reduce overhung mass and length.
2015, Panara [11]	3	Reduce overhung mass
2012, Childs [26]	1,2,3	Reduce imbalance and lubricant viscosity; increase bearing L/D ratio
2014, Suh [29]	1,2	Reduce supply oil temperature, pivot stiffness; increase C_b.
2016, Tong [27]	1,2,4	Increase pivot offset; reduce mixing coefficient by direct lubrication; increase oil temperature; install heat barrier sleeve
2016, Tong [28]	1	Change bearing type; use 0.6 pivot offset; reduce bearing L/D ratio

1.4 Morton Effect Modeling and Prediction

Meanwhile, researchers and engineers are dedicated to improve the ME prediction model, which often involves solving the multi-physics problem combining thermodynamics, rotordynamics and elastic mechanics. The theoretical analysis of the ME

was firstly established by Keogh and Morton in 1993 [34], where the differential heating and thermal bending of the journal were investigated. In particular, the relation between the journal orbit and the steady journal ΔT was established. Inspired by the classic control theory, the gain of the thermal bending development was introduced for stability analysis. In 1994, Keogh and Morton [35] incorporated the thermal bending into the rotordynamic model and performed the stability analysis over a speed range. The results demonstrated that a system designed to be satisfactory with existing criteria could be unstable due to the ME. Inspired by Keogh's research, in 1999 Larsson [36, 37] applied the ME instability analysis to a rotor system with 5-pad tilting pad bearings. Heat conduction and shaft bow were incorporated into the rotordynamics and results were presented as a frequency response of the shaft thermal bow. In 1999, Gomiciaga and Keogh [13] predicted the journal heat flux by orbit time averaging using CFD (Computational Fluid Dynamics) techniques. In 2004, Balbahadur and Kirk [31] employed the imbalance threshold criterion to replace the classic control theory for ME stability analysis in frequency domain. In 2010, Murphy and Lorenz [38] adopted the simplified ME analysis, where the interactions between vibrations, imbalance and journal ΔT were linearized with sensitivity coefficients. In 2012, Childs and Saha [26] calculated the journal temperature by adding the temperature components from the forward and backward orbits and predicted the rotor response by taking account of the initial imbalance, the bowed shaft moment and the thermal imbalance.

Most of the prediction methods above are based on the steady state analysis in the speed domain to identify the ME instability onset speed. However, considering that the

ME can be highly process-oriented, not only the operating speed but also the transient speed acceleration can trigger instability. For instance, de Jongh [16] mentioned that any speed increase of 1000 rpm within 10 seconds directly triggered the instability, however, in Ref. [12] for another compressor, he found that by quickly raising the rotor speed, it was possible to run through the unstable speed range. Therefore, a comprehensive transient method is needed to illustrate the ME response in time domain. In 2012, Lee and Palazzolo [39] adopted the staggered integration scheme for the transient ME analysis. In 2014, Suh and Palazzolo [40] improved the transient analysis with the 3D energy equation to account for the rotor temperature distribution along the axial direction. The rotor thermal bow was modeled with distributed thermal imbalance to replace the conventional lumped imbalance method. In 2015, Grigor'ev et al [41] applied the perturbation method to solve the oil pressure and temperature, and adopted the averaging method to solve the rotor and bearing dynamics. Large time steps in the numerical integration process were used to reduce the computational cost. In 2016, inspired by Suh's work, Tong and Palazzolo [42] adopted a more accurate bowed rotor method instead of simplifying the thermal bow with thermal imbalance. A more general rotor model with double overhung disks and multi-bearing capacity [43] was developed for both transient and steady state analysis. The detailed explanation of several typical methods mentioned above are categorized and discussed below. These numerical prediction methods provide a powerful tool to eliminate the potential ME induced instability in the design stage and also make it more convenient for trouble shooting. However, more case studies are needed to verify and calibrate the published prediction techniques due to the complicated nature of ME.

1.4.1 Feedback Analysis

Keogh and Morton [34, 35] proposed an analytical method with feedback mechanism to predict the ME instability, as shown in structure 1 of Fig. 1-3, where $G(s)$ is the gain parameter for bend development and defined by $\widetilde{\Psi}_{Ct}(s) = G(s)\widetilde{\Psi}_{Cb}(s)$, and $\text{Re}(G) > 1$ indicates instability of the system. $G(s)$ is speed dependent and should be accurately predicted by (1) modeling the rotor dynamic response χ_T with the bent shaft excitation χ_B, shown in Eq. 1-1, (2) solving the temperature distribution for a whirling journal, and (3) calculating the rotor thermal bending due to the ME induced ΔT using Dimarogonas's formula [6]. The temperature of the lubricant, bearing and shaft was evaluated by the orbit perturbation method, where the orbit was expressed in terms of superposition of the backward and forward components. Moreover, the journal temperature was decomposed into trigonometric series in Eq. 1-2 and only the first steady spatial harmonic of temperature would contribute to the rotor thermal bow, i.e., $m = 0, n = 1$. Short bearing theory, laminar flow, incompressible lubricant and an invariant viscosity were assumed. Axially averaged lubricant temperature, heat flux, and the resultant axially averaged energy equation were considered.

$$M_R \ddot{\chi}_T + (C_B + \Omega I_R)\dot{\chi}_T + (K_R + K_B)\chi_T = K_R \chi_B + F_{im}, \qquad \textit{Eq. 1-1}$$

where $\chi_T = \chi + \chi_B$.

$$T_J(r, \theta, \tau) = T_A + \sum_{-\infty}^{\infty} \sum_{-\infty}^{\infty} a_{mn} e^{i(n\theta + m\tau)} \qquad \textit{Eq. 1-2}$$
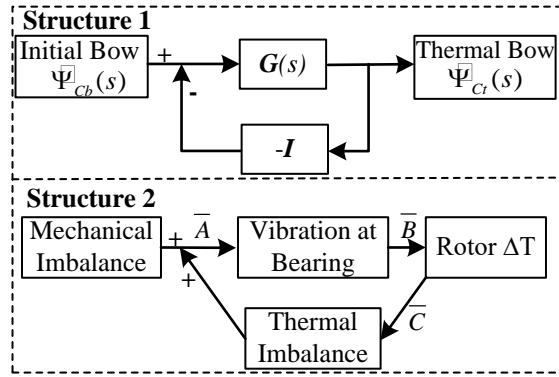
Fig. 1-3 Feedback diagram for Morton Effect prediction.

de Jongh [16] adopted a similar feedback mechanism modeling the thermal bow with thermal imbalance, which was the product of overhung mass and distance. The resultant imbalance was the vector sum of the mechanical and thermal imbalance and was used to calculate the rotor vibration at the bearing location. As shown in structure 2 of Fig. 1-3, the combination of three serial sub-functions $\overline{B}\overline{A}\overline{C}$ is equivalent to the overall $G(s)$ in structure 1: $\overline{A}$ is the influence between the imbalance and the vibration at bearing node, $\overline{B}$ is the influence between the vibration at bearing node and the rotor ΔT, and $\overline{C}$ is the influence between the rotor ΔT and the thermal imbalance. The transfer functions $\overline{A}$ and $\overline{C}$ were measured by software, while $\overline{B}$ was acquired from experiment [16]. This method was applied to a double overhung compressor by de Jongh [12] and the predicted instability onset speed was around 10,500 rpm, which agreed with observation. In 2010, Murphy and Lorenz [38] extended de Jongh's approach by acquiring $\overline{B}$ through numerical simulation rather than experiment. Specifically, one journal orbit was divided into 24 equally spaced points and the film temperature distribution with the shaft positioned at all

orbit points was calculated. Because the journal was whirling synchronously, these points actually represented 24 time steps within one orbit, i.e., $t = \left[0, \frac{T}{24}, \frac{2T}{24}, \ldots, \frac{23T}{24}\right]$, where T is the whirling period. The static journal surface temperature was calculated by averaging the film temperature profiles at all time steps. The phase lag between the high spot and hot spot was not determined and was instead acquired from other case studies. Murphy and Lorenz applied this method to a double overhung turboexpander [20] and predicted a ME instability onset speed which was close relative to the observed speed.

1.4.2 CFD Based Approach

In 1996, Tucker and Keogh [44] applied the CFD technique with finite volume method (FVM) to analyze the dynamic and thermal state in a hydrodynamic bearing with a whirling journal. The rotordynamic problem was not considered and the journal was assumed to be whirling with a pre-defined orbit size and eccentricity. Navier-Stokes equation and energy equation were solved simultaneously for both the lubricant flow velocity and temperature, and the heat flow in the solid components was determined by the diffusion equation. Fluid pressure in the cavitation area was calculated by employing the dynamic cavitation effects, which considered the time dependent reversed flow and also allowed the possibility of sub-ambient pressure. The heat flux and temperature were set to be continuous on the boundary surfaces of the lubricant/bearing and shaft/lubricant, and other surfaces of the shaft exterior to the bearing width were imposed with heat convection boundary conditions. Tucker and Keogh [44] firstly benchmarked the simulation with Lund's experiment [45] for the zero-orbit case and discovered that the journal surface was behaving as an isothermal element. However, for a centered circular

14

orbit, significant ΔT as high as $7^o C$ developed across the shaft with the orbit size of 0.58 C_b, and the axial variations of the shaft temperature were slightly higher than the zero-orbit case. In 1999, Gomiciaga and Keogh [13] extended Tucker's method to investigate the non-centered orbit case, and the heat input into the journal was obtained by orbit time averaging. The procedure was applied to a two-inlet circular bearing with backward and forward circular whirl over a range of operating speeds. The steady asymmetric heat input into the journal was found to have a sinusoidal component, which may cause a steady surface temperature differential across the journal. Gomiciaga and Keogh also concluded that (1) the journal ΔT generally increased with running speeds while the trend was slower at higher speed due to the reduced viscosity, (2) the journal ΔT increased linearly with the journal orbit size ϵ when $\epsilon < 0.2 C_b$, however, Childs et al. [26] showed that the relationship turned out to be quite nonlinear for larger ϵ. (3) The hot spot on the journal surface lagged the high spot for the forward whirl and leaded the high spot for the backward whirl. Prior research used custom built CFD codes, however, Lorenz [46] demonstrated that the same solution process could also be implemented with a commercially available CFD software package.

1.4.3 Unbalance Threshold Method

In 2003, Kirk et al. [17] proposed an unbalance threshold method for the ME predication. In this method, the initial mechanical imbalance was set to be located at the center-of-gravity of the overhung mass, and be large enough to create a centrifugal force equal to 10% of the total static rotor weight at MCOS (Maximum Continuous Operating Speed), as shown in Eq. 1-3.

$$U = 0.1W/\omega^2_{MCOS} \hspace{6cm} Eq.\ 1\text{-}3$$

The mechanical imbalance was then used to predict the steady-state orbit and the high spot location for the journal, and moreover, the hot spot was assumed to coincide with the high spot. The temperature variation across the journal circumference could be acquired by solving the 1D simplified energy equation, which neglected the time dependence and axial heat flow. Finally, the thermal imbalance $U_{\Delta T}$ caused by the thermal bending was calculated by multiplying the overhung mass M and distance e, and the phase of the thermal bow was consistent with the thermal deflection at the overhung location. This thermal imbalance modeling was also adopted by de Jong [16] and Murphy [38], as shown on the left of Fig. 1-4. The resultant imbalance was the vector sum of the mechanical and thermal imbalance, and if it exceeded the threshold imbalance U_{thr}, the system was unstable. U_{thr} was firstly defined to be speed dependent, as shown in Eq. 1-4 and the corresponding imbalance force was 15% of the rotor weight [17]. In 2013, Kirk [33] adopted a constant threshold version, shown in Eq. 1-5, considering that designers using the old threshold may observe a crossing speed beyond the MCOS even without thermal imbalance increasing. The imbalance threshold was optimized by benchmarking several case studies with both plain journal bearings and tilting pad bearings, so that the predicted ME instability onset speed could be consistent with the observed onset speed, as shown on the right of Eq. 1-4. The author also concluded that a centered, circular, large amplitude orbit was the worst ME scenario due to a small phase angle between the resulting thermal imbalance and the original mechanical imbalance.

$$U_{thr} = 0.15W/\omega^2 \qquad\qquad\qquad\qquad\qquad\qquad\qquad Eq.\ 1\text{-}4$$

$$U_{thr} = 0.15W/\omega_{MCOS}^2 \qquad\qquad\qquad\qquad\qquad\qquad Eq.\ 1\text{-}5$$
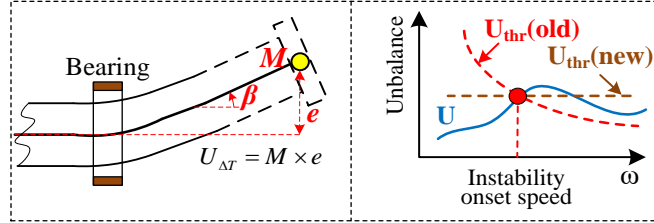
Fig. 1-4 Illustration of unbalance threshold method.

1.4.4 Thermal Ratio Method

The thermal ratio method was introduced by Schmied [20] to calculate the hot spot stability based on the hot spot model of Kellenberger [7]. This method was initially designed to analyze the spiral vibrations induced by light rubs between rotors and stators [9], and could also be used for the ME analysis. The modeling of the hot spot phenomenon was based on Eq. 1-6.

$$\dot{x}_B = p\Omega x - qx_B \qquad\qquad\qquad\qquad\qquad\qquad\qquad Eq.\ 1\text{-}6$$

Where, $p\Omega x$ was the added heat term and assumed to be proportional to the rotating speed Ω and vibration amplitude x at the hot spot location, and qx_B was the eliminated heat proportional to the thermal deflection x_B. The stability threshold was a function of the ratio $p\Omega/q$, where p and q were the proportionality factors for the added heat and

17

eliminated heat, respectively. Both p and q depended on the heating mechanism and must be derived accordingly [20]. If the ratio of added to eliminated heat was close to the threshold or even above the threshold, the rotor could be regarded as sensitive to the ME. Fig. 1-5 illustrates the thermal ratio method, where the solid curve crosses the threshold curve within the operating speed band, indicating that the system may encounter ME instability. By reducing the heat input in the bearing, e.g., reducing the bearing width or lubricant viscosity, the thermal ratio curve will shift downwards and the ME-instability is removed since the crossing speed is pushed outside the operating band, as shown in Fig. 1-5.
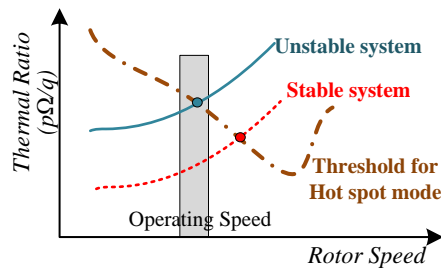
Fig. 1-5 Illustration of the thermal ratio method.

1.4.5 Nonlinear Transient Prediction Method

Previous approaches mainly focus on the steady state analysis of the ME in speed domain. However, considering that (1) the ME can be a transient process, which is not only related to speed but also is acceleration dependent, and (2) the ME can be highly sensitive to operating conditions while most steady methods adopt simplified assumptions in the ME modeling, such as linearizing relationship of the bearing orbit and rotor ΔT [38]

18

or neglecting the C_b change due to the asymmetric rotor thermal expansion [17], the fully nonlinear transient prediction with high fidelity modeling is quite necessary. Palazzolo and his collaborators have focused on the transient Morton analysis since 2009, aiming to view the rotor vibration and temperature profile in time domain. In 2012, Lee and Palazzolo [39] calculated the transient asymmetric temperature distribution of the journal by solving the variable viscosity Reynolds equation, 2D energy equation, heat conduction equation, and equations of motion for the rotor. The rotor thermal bow was modeled by a lumped imbalance located at the overhung, similar to Murphy [38], Kirk [17] and Childs [26]. The tilting pad bearing model was general and nonlinear, and the thermal mode reduction and staggered integration approach (SIA) were utilized in order to reduce the computation time. The SIA was adopted considering that the rotordynamic response was much faster than the rotor temperature change and the former would soon converge before updating the rotor and bearing temperature. Fig. 1-6 shows the diagram of the SIA, where each staggering cycle consists of two stages. During the 1st stage, the Reynolds, energy, heat conduction, and rotordynamic equations of the rotor are solved. The temperature and viscosity are then stored at the end of stage 1 and used for stage 2, where the transient heat conduction equation is solved to update the rotor and bearing temperature. The integration time for stage 2 is set to be much longer than stage 1 to accelerate the software execution. The algorithm was verified by Gomiciaga's CFD prediction [13], and the rotor ΔT was overpredicted due to the assumptions of the insulated boundary condition at the bearing/film interface and (2) neglect of axial thermal gradient in Lee's method.

19
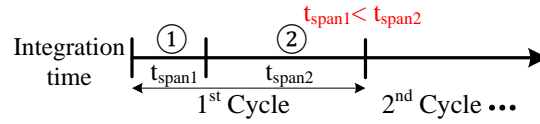
Fig. 1-6 Diagram of the staggered integration scheme.

Suh and Palazzolo [29, 40] improved Lee's approach by adopting the 3D energy equation to account for the oil temperature variation in the axial direction. The 3D heat transfer equations of the bearing and shaft were modeled with the finite element method (FEM) and thermally coupled with the fluid film via a heat flux boundary condition. The heat flux $k\frac{\partial T}{\partial r}$ and temperature T were assumed to be continuous on the rotor-lubricant and lubricant-bearing surfaces to replace the insulated boundary condition in Lee's approach [39]. At each time step, the heat flux boundary conditions between the lubricant and spinning shaft were saved and the orbit time averaged boundary conditions were calculated after a single orbit and imposed on the shaft to update the transient rotor temperature distribution. The rotor thermal deformation was calculate by the 3D FEM instead of using Dimarogonas's formula [6]. Moreover, a distributed thermal imbalance model was proposed to include all nodal thermal imbalance in the bowed rotor on the overhung side, while other methods only considered the imbalance at the overhung disk [38, 39].

All previous methods neglect the thermal bows in the mid-span rotor (between bearings) and may induce possible errors in ME predictions, considering that Guo et al. [23] suggested it was also possible for the mid-span rotor with large mass between bearings to experience the ME instability. To balance the accuracy and computational cost

20

of the 3D FEM, Tong and Palazzolo [42] improved Suh's approach by adopting the hybrid

finite element method to calculate all rotor thermal bows including both the overhung

location and mid-span rotor. As illustrated in Fig. 1-7, the rotor section close to the fluid

film bearing, i.e., the thermal rotor, was modeled with 3D solid elements. Meanwhile,

other rotor parts with negligible temperature increase were modeled with beam elements.

Note that fictitious connecting beams were included at the solid and beam element

interfaces to transmit forces and bending moments caused by the dynamic motion and ΔT

distribution in the journal region.
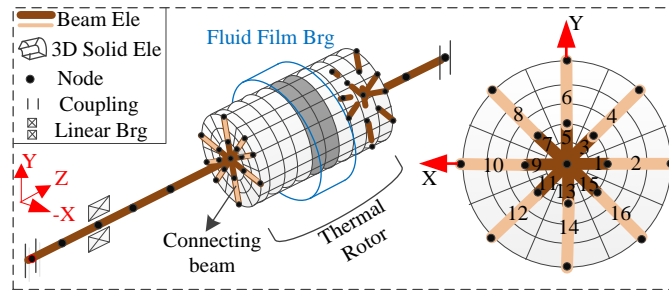
Fig. 1-7 Diagram illustrating the hybrid finite element method.

Tong and Palazzolo [42] also suggested that the bowed rotor method (see Eq. 1-7

should be used to replace the thermal imbalance method, considering that the latter

neglected the moments induced by the transverse angles in thermal bow and the damping

related effects, and in certain cases may overpredict the rotor vibration and ΔT. Also note

that Eq. 1-7 is different from Eq. 1-1 in the aspect that the transient bearing force $\boldsymbol{F}_{brg}$

updated by the Reynolds equation at each time step is utilized instead of the linear dynamic

coefficients $\boldsymbol{C}_B$ and $\boldsymbol{K}_B$, which may overpredict the ME in large orbit cases.

$$M_R \ddot{\chi}_T + C_R \dot{\chi}_T + K_R \chi_T = K_R \chi_B + F_{im} + F_{gyro} + F_{brg},$$

where $\chi_T = \chi + \chi_B$ *Eq. 1-7*

1.4.6   Summary of Different Methods

Based on the aforementioned discussion, the detailed comparison of various ME prediction methods is listed in Table 1-3.

Table 1-3 Comparison of different prediction methods

	Keogh [34, 35]	Tucker [44], Gomiciaga [13], Lorenz[18]	Kirk [17, 33]	Murphy[38], deJongh [16]	Schmied[20]	Grigor'ev et al. [28]	Palazzolo et al. [40, 42, 43]
Steady/Transient?	Steady	Steady	Steady	Steady	Steady	Transient	Transient
Unstable criterion	Re(G)>1, where G is the gain parameter of thermal bow	Not available. Only focus on thermodynamics aspect with CFD.	$U > U_{thr}$, $U_{thr} = \dfrac{0.15W}{\omega_{MCOS}^2}$	$Re(\bar{B}\bar{A}\bar{C})>1$, where $\bar{B}, \bar{A}, \bar{C}$ are the sensitivity coefficient	$p\Omega/q >$ threshold, where p, q are factors for added and eliminated heat	Maximum modulus eigenvalue of the transition operator or rotor trajectory	Multi-opitions (1) film thickness (2) oil temperatue (3) vibration amplitdue
How to calculate rotor thermal bow?	Simplified analytical solution	Not available	Simplified analytical solution	Simplified analytical solution	Beam model; unit cross sectional ΔT along bearing length	Simplified analytical solution	Use 3D FEM to solve the rotor thermal deformation
How to calculate temprature of the rotor?	Solve energy eq. with short bearing theory; calculate temperature with perturbation method	Use CFD to solve the 3D film, bearing, rotor temperature	Solve 1D energy eq. with temperature variation across circumeference	Post-processing results from general rotordynamic software	Cross sectional ΔT of the journal is directly linked to thermal bow	Use FVM (Finite volume method) to solve 2D energy eq. and 3D heat conduction in shaft	Use FEM to solve the 3D energy eq. in oil and 3D heat conduction in solids.
How to model the thermal bow in rotordynamics?	Bowed rotor method with linear bearing coefficients	Not available	Lumped thermal imbalance at overhung	Lumped thermal imbalance at overhung	Bowed rotor method with linear bearing coefficients	Distributed thermal imbalance; bowed rotor method with bearing coefficient.	Distributed thermal imbalance/bowed rotor excitation
Execution speed	Fast	Slow	Fast	Medium (prepare $\bar{B}, \bar{A}, \bar{C}$ first)	Fast	Need 14 mins to simulate 100s (depends on mesh size)	Need 20 mins to simulate 100s (depends on mesh size)

The ME prediction approaches can be summarized into two categories: (1) Simplified approaches with the advantages of low computational cost, while adopt assumptions such as no variation in bearing clearance, axial rotor temperature, no phase lag between high spot and hot spot, etc., and (2) highly fidelity approaches using the 3D FEM to predict the rotordynamics and temperature distribution in the rotor and bearing. The simplified method [11, 38], despite its fast response and relatively easier implementation, sometimes cannot meet the accuracy demand due to the complicated nature of Morton effect and its sensitivity to operational parameters. Thus, the high-fidelity approach, in most cases, needs to be adopted to predict the potential or verify the existing ME instability problem by taking into account the most detailed operating conditions.

1.5   Experimental Morton Effect

Acquiring rotor temperature distributions from operating machines, provides a straight forward benchmark for ME prediction theories, but is extremely challenging in practice. On one hand, embedding the temperature sensors into the rotor will deteriorate the rotor integrity and mechanical strength, and moreover, the protection system will always trip the rotor before the ME instability fully develops. Researchers thus built dedicated ME test rigs to acquire experimental data and compare with ME predictions to calibrate the prediction software.

1.5.1 de Jongh and Morton

In order to replicate the ME-induced instability in the original compressor, de Jongh and Morton [12] built a shorter and simplified rotor, which was supported by the same tilting-pad bearings and exhibited identical rotordynamic characteristics in terms of critical speed and imbalance response. Considering that the overhung mass at the NDE (non-drive end) was greater than the DE (drive-end), only the NDE journal was measured for temperature distribution. Four RTDs (Resistance Temperature Detectors) were inserted 1.3 mm below the journal surface with 90° apart. A special slip-ring-less transmitter was used to transfer the temperature signals from the rotating shaft to the stationary measuring equipment. The journal ΔT was measured between two sensors spaced 180°. de Jongh and Morton found that when running at 10.5 krpm, the rotor was stable with small vibration and journal ΔT of $3^o C$. When the rotor was accelerated to 11.2 krpm, the vibration amplitude and phase fluctuated over a range, and above this speed, the vibration and journal ΔT grew continuously. The rotor ΔT could increase to around $10^o C$ before the speed was reduced to avoid damage, and the 1X polar plot showed that the vibration vector was spiraling in the same direction as the running speed. Some interesting phenomena observed by de Jong and Morton include (1) rotating the attached imbalance by 180° shifted the location of the hot spot by about the same angle. (2) At certain speed, the journal ΔT was proportional to the orbit size. (3) The phase lag between the high spot and hot spot was 20° at 10.5 krm but may change with speed. (4) By quickly raising the rotor speed, it was possible to run through the unstable speed range and recover stability at higher speed, though this was not verified with a real compressor due to speed

limitations. (5) Reducing the NDE coupling mass of 5 kg raised the instability onset speed by 10%.

1.5.2   Kirk and Balbahadur

To verify the unbalance threshold method in ME prediction, Balbahadur and Kirk [47] modified their existing testing rig with a new shaft and tilting pad bearings to investigate the ME. The initial idea of measuring the rotor ΔT was abandoned due to the complexity and cost, and recording the pure rotordynamic symptoms including hysteresis, vibration amplitude and phase changes were adopted to distinguish the ME. Shaft diameter and bearing clearance were optimized so that (1) the predicted ME instability speed was within the running speed range 450-10,000 rpm, (2) a smaller static eccentricity could be obtained, and (3) the predicted ME instability speed could be separated sufficiently far from the lateral critical speed to preclude the resonance effect. During the balancing process, Kirk and Balbahadur [47] found that it was particularly difficult to suppress the large vibration close to the 3rd critical speed at 8 krpm by conventional balancing, even with the three plane balancing technique. The 1st and 2nd critical speeds were the rigid body modes, which were either damped out or not excited, while the 3rd mode shape corresponded to the 1st bending mode with large deflections at the NDE-overhung disk and the DE-coupling. During real testing, the rotor was firstly held at different fixed speeds for several minutes, and no significant vibrations were observed under 7800 rpm. The rotor then was examined through run-up and coast-down testing from 5000 to 9000 rpm, and evident hysteresis was observed: the coast-down vibration was much higher than the run-up from 7500 to 8500 rpm, and the speed with peak vibrations coincided with the 3rd

critical speed, which was also confirmed from theoretical prediction. The authors also found that reducing the supply oil temperature from $100^{o}F$ to $78.3^{o}F$ would reduce the vibration slightly but not eliminate the instability. Eliminating other possible causes including mechanical imbalance variation, Newkirk effect, etc., the ME was identified as the cause of the hysteresis phenomenon. However, due to the close proximity between the critical speed and the instability onset speed, Balbahadur [47] also expressed concerns over the resonance effect on the excessive vibrations, especially when no rotor ΔT occurred to confirm the ME.

1.5.3 Panara et al.

Panara et al. [11] built a dummy rotor to verify the simplified stability approach suggested by Murphy [38] and an iterative FEM thermo-structural dynamic analysis. In the simplified ME approach, the sensitivity coefficient between the vibration vector and the rotor ΔT was quite critical and was acquired through the experiment by Panara et al. To measure the rotor ΔT and also the phase lag of the hot spot relative to the high spot, eight thermocouples equally spaced across the journal circumference were installed a few millimeters below the journal surfaces through a set of axial holes. The electric temperature signals of the spinning shaft would finally transmit to the stator through a wireless slip ring, similar to de Jongh's experiment [12]. Moreover, additional temperature probes were installed on the bottom pad and the next downstream pad to measure the bearing temperature for software calibration. The NDE overhung weight could be varied by means of different idling adaptors hydraulically fit on the shaft. During the test, three different overhung weights (12.4%, 8.4%, 7.3% of the rotor weight) were studied. Panara

et al. reported that the observed ME-instability onset speed decreased from 13.6 krpm to 10.2 krpm to less than 10 krpm when the overhung weight varied from the lightest to the heaviest. By correlating the predicted unbalance response with the measured vibration profile, Panara et al. pointed out that the shift of the overhung critical speed could be directly linked to the shift of the rotor instability speed. During the testing process, Panara et al. also found that the stability could be recovered when the test speed exceeded a certain speed threshold. The linear ME analysis proved to be quite efficient in identifying the instability onset speed, however, it sometimes failed to predict the stability recovery due to the evident discrepancies in evaluating the phase lag.

1.5.4   Tong and Palazzolo

Tong and Palazzolo from Texas A&M University recently conducted an ME experiment to calibrate the transient ME prediction algorithm. The shaft is supported by two rigid ball bearings, and the maximum operating speed of 5 krpm is thus well below any critical speed to prevent resonance. The test 5-pad tilting pad bearing is installed between ball bearings, and the middle stage of the rotor is offset by 2.7 mils (1 mil = 1/1000 inch) in its centerline relative to the entire shaft, thus resulting in a prescribed orbit in the tilting pad bearing when the entire shaft is spinning. The static eccentricity of the tilting pad bearing can be adjusted by changing the positions of the tilting pad bearing housing meanwhile fixing the ball bearing housings. 20 RTD sensors are imbedded 1 mm beneath the rotor surface across the circumference to give the most detailed rotor temperature distribution, and the hot spot location relative to the high spot can be easily identified. A slip ring is mounted on the shaft end with its stator connected to the data

acquisition card. The development of the test rig is still in progress and initial testing data at 4 krpm revealed a rotor ΔT close to 6^oF and phase lag of 41° between the high spot and hot spot.

1.6   Limitation of API Standard in Morton Effect

The API (American Petroleum Institute) standard covers the minimum requirements for turbomachinery equipment in design and operating by quantitatively specifying the separation margin, imbalance response, etc., to avoid the synchronous dynamic instability. To avoid excessive vibration due to the resonance effect, sufficient SM is specified by API 617 [48] to ensure that the operating speed is not in the proximity to the critical speed, and for critically damped cases (amplification factor AF<2.5), no SM is required. However, when the ME is involved, the conventional specification of SM seems not sufficient because the excitation imbalance is varying with speed and can be significantly amplified by the thermal bow near the instability onset speed. Table 1-4 lists the published case studies showing the observed instability onset speed and the nearby critical speed. As shown in Table 1-4, the ME instability can still occur although most cases (except Lorenz [18]) satisfy the SM requirement based on API 617 [48]. For Lorenz's case [18], although the running speed at 4200 rpm was close to the critical speed at 4000 rpm, Lorenz suggested that the analytical results excluding the ME revealed that the vibration response at the bearings should be within the specifications if the imbalance magnitudes were reasonably well controlled. All these cases indicate that the conventional SM requirement has its limitation in avoiding the ME instability. The goal of developing

generic guidelines/standards for machine design to avoid or mitigate the Morton Effect will be very challenging due to the complex, coupled thermal-hydrodynamic-deformation dynamics nature of the problem and the scarcity of test data.

Sufficient SM does not necessarily guarantee elimination of the ME, for example, in the cases of Kocur [15] and Schmied [20], the ME instability onset speed was well displaced from any critical speed. Theoretically, the ME instability may occur at any speed if the positive feedback is formed among the bearing orbit, rotor ΔT and rotor thermal bow. Therefore, performing the ME analysis with the aforementioned methods in Section 1.4 is highly recommended. Presently there are very few rotordynamics software codes that simulate the ME instability, exceptions being MADYN 2000 from Delta JS, the Morton effect module of XLTRC2 from TAMU and VT-MAP from Virginia Tech. Conventional rotordynamics software featuring options for imbalance response and critical speed and mode shape, can provide some limited assistance for designers to avoid the ME. For example de Jongh [12] states that the rotor thermal bow can be amplified if the operating speed was in the vicinity of the second bending mode when large deflection occurs at the overhung nodes. Likewise, Panara [11] pointed out that the shift of the overhung critical speed could be directly linked to the shift of the rotor instability speed. The journal ΔT can be significantly boosted by large vibration at the bearing as the operating speed approaches the aforementioned critical speed even if the SM requirement in API 617 is satisfied or the corresponding mode is well damped. The resulting thermal imbalance will further amplify the vibrations causing a rotor ME instability. Thus, designers need to be careful of the rotor modes, which have large deflection at the overhung nodes. These

modes can be a rigid conical mode [49], an overhung mode, the first bending mode [20], the 2nd bending mode [12], or a high vibration mode above the overhung mode.

The ME instability is not necessarily in the vicinity of any critical speed. However, increasing the SM by pushing the "dangerous" modes away from the operating speed may favorably suppress the ME, though not always. This explains why Schmied [20] stiffened the rotor to raise the first bending critical speed but also reduced the bearing width and lubricant viscosity to eliminate the heat generation.

Table 1-4 Comparison of instability onset and critical speed

Cases	Instability onset speed (rpm)	Critical speed (rpm)	Satisfy API 617?
1994, de Jongh [12]	10500	14000	Yes
1997, Faulkner [19]	9800	>12500	Yes
1997, Corcoran [30]	8500	9100	Yes (critically damped)
1998, deJongh [16]	7200	8000	Yes (critically damped)
1999, Berot [14]	6510	2500, 5200	Yes (critically damped)
2000, Kocur [15]	SM> 20% to any undamped mode; SM> 50% to the impeller overhung mode		
2008, Schmied [20]	18600	28894	Yes
2011, Lorenz [18]	4200	4000, 5756	No

1.7   Contribution of Current Research

Considering that the ME cannot be predicted with conventional rotordynamic analysis or avoided with general API standards, it is quite necessary to propose the high-fidelity prediction methodologies, which can take account of detailed rotor and bearing configuration as well as operating conditions. Case studies and experimental measurement

should be conducted to justify the theoretical modeling. The contribution of the current research is listed as follows.

(1) Establish the ME prediction methodology for rotors with overhung mass at both sides (double-overhung rotor model).

Previously published ME analysis only focuses on the single-overhung rotor case, where the overhung mass is located at the rotor NDE side. The double-overhung rotor model requires the ME analysis to be implemented on both rotor-bearing sides. The rotor thermal bow on one rotor side is likely to affect the rotordynamics and bearing performance on the other side, and the coupled relationship makes it more complicated to predict the entire system instability. The ME methodology for the double-overhung rotor model is proposed and predictions are compared with the classical single-overhung method. The double-overhung method is proven to be more accurate in the prediction of ME induced vibration. Nevertheless, the single-overhung method is less computational intensive. Detailed discussion can be found in Section 3.

(2) Propose the high-fidelity bowed rotor method to replace the traditional thermal imbalance method.

Traditional ME analysis simplifies the ME induced rotor bow into the thermal imbalance, which neglects the thermal bending moment as well as the rotor thermal bow located between bearings. The thermal imbalance method is shown in some cases to predict incorrect ME instability onset speed. The high-fidelity bowed rotor method is proposed herein to account for the neglected bending moments and thermal bow between bearings. The non-thermal bow and disk skew excitation are also considered.

(3) Conduct parametric studies on ME related to rotor/bearing configuration and operating conditions.

The Morton effect is reported to be sensitive to rotor/bearing configuration and operating conditions. Slight change of rotor imbalance, overhung mass, bearing clearance, pivot offset, supply oil temperature and oil viscosity can affect the rotor temperature difference and ME development. Parametric studies are conducted by case studies in Section 5 to evaluate possible influence on ME related to rotor vibration, journal circumferential temperature difference, minimum film thickness ratio in bearings, etc. The objective is to seek the best set of parameters that can suppress the ME instability.

(4) Designed the ME testing rig and measured the rotor circumferential temperature distribution.

Measurement of journal circumferential temperature distribution can be barely found in earlier publication but is highly necessary to justify the proposed analytical model. 20 RTDs (resistance temperature detectors) are installed on the journal outer surface to provide the most detailed circumferential temperature distribution by far. Different operating conditions including the supply oil temperature and bearing eccentricity are tested to evaluate the influence on ME. The detailed results are discussed in section 6.

(5) Predict the experiment with the proposed high-fidelity method and the simplified method.

The measurements of journal circumferential temperature ΔT are used to benchmark the high-fidelity ME modeling in Section 7. The simplified ME prediction method, which was proposed by Murphy [38], is also applied and compared with both the

33

experiment and the high-fidelity approach. Results show that the transient 3D high-fidelity approach is more accurate in predicting the journal ΔT, and the simplified ME method in most cases over predicts the journal ΔT and cannot predict the location of the hot spot position.

2 THERMO-ELASTO-HYDRO-DYNAMIC MODELING OF

FILM, BEARING AND SHAFT*

Accurate thermo-hydro-dynamic (THD) analysis of the fluid film bearings is the prerequisite for Morton effect (ME) prediction, and it includes analysis of the bearing temperature, film pressure and temperature as well as the bearing dynamics. The THD analysis was mainly used for predicting the bearing dynamic coefficients and steady characteristics [50-52], although it could also be applied for the transient analysis [25, 53]. The more recent TEHD (thermo-elasto-hydro-dynamic) analysis also includes the bearing elastic deformation and is more accurate than the THD. Generally, the shaft temperature distribution is not a significant concern in the TEHD analysis and thus is assumed to be isothermal and calculated by either averaging the oil temperature [52] or imposing the no net-heat-flow boundaries conditions on the shaft-oil interface [1, 50, 54]. Note that the ME prediction differs from the general TEHD analysis in the aspect that the detailed journal temperature distribution needs to be solved in the ME prediction to calculate the rotor circumferential ΔT and thermal bow, which is then incorporated into the rotordynamic analysis.

---

* Part of this section is reprinted with permission from "Double Overhung Disk and Parameter Effect on Rotordynamic Synchronous Instability—Morton Effect—Part I: Theory and Modeling Approach" by Tong, X., and Palazzolo, A., 2017. Journal of Tribology, 139(1): 011705. Copyright 2017 by ASME.

2.1 Film Pressure and Temperature Model

2.1.1 Film Viscosity Model

The ME is caused by the uneven oil viscous shearing around the journal and can be significantly affected by the oil temperature due to the sensitive oil viscosity-temperature relationship, which is modeled by an exponential function below in Eq. 2-1, where μ is the lubricant viscosity, α is the viscosity coefficient, T is temperature, the subscript "ref" indicates the reference viscosity or temperature.

$$\mu = \mu_{ref}exp(\alpha(T_{ref} - T))$$ *Eq. 2-1*

Fig. 2-1 illustrates the measured and curve-fitted viscosity-temperature profile for VG 46, note that for most temperature, the curve-fitted viscosity by Eq. 2-1, where $\mu_{ref} = 0.044 \frac{Ns}{m^2}, T_{ref} = 40°C, \alpha = 0.04218$, coincides with the measured viscosity, indicating that the exponential function is quite effective.
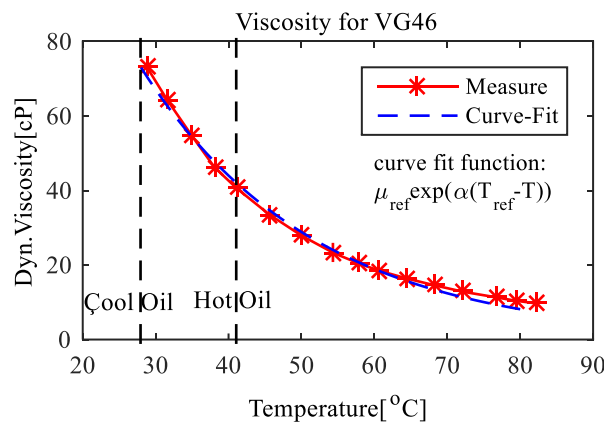
Fig. 2-1 Viscosity profile at different temperature.

36

The oil temperature should be accurately predicted to update the viscosity in time. And in current simulations, the 3D energy equation is employed and solved with FEM to provide the oil temperature distribution in all radial, circumferential and axial directions. The nodal velocity distribution required in the energy equation is solved from the Reynolds equation with FEM and meanwhile the viscosity in the Reynolds equation is closely related to the temperature output of the energy equation. Both coupled relationships require the above two equations to be simultaneously solved, which is realized by dividing the entire bearing orbit into dozens of segments and solving both equations successively within each segment.

2.1.2 Reynolds Equation

The governing equation for film pressure between the journal and bearing is the Reynolds equation, derived based on the continuity and momentum equation. By assuming that the fluid is Newtonian and the inertial and body force are neglected, the generalized Reynolds equation with variable viscosity is shown Eq. 2-2, where h is the film thickness, $\boldsymbol{U_1}$ is the velocity vector of the bottom surface $y = 0$, $\boldsymbol{U_2}$ is the velocity vector of the top surface y$= h$.

$$\nabla \cdot (D_1 \nabla P) + \nabla D_2 \cdot (\boldsymbol{U_2} - \boldsymbol{U_1}) + (\nabla h) \cdot \boldsymbol{U_1} + \partial h/\partial t = 0 \qquad\qquad \textit{Eq. 2-2}$$

In most cases, the bearing is stationary with $\boldsymbol{U_1} = \boldsymbol{0}$ and the shaft is rotating with surface speed $\boldsymbol{U_2} = \boldsymbol{U} = [\omega R, 0]$ in the tangential and axial direction, respectively. Thus, the generalized Reynold equation in Eq. 2-2 can be simplified into Eq. 2-3.

$$\nabla \cdot (D_1 \nabla P) + \nabla D_2 \cdot U + \partial h / \partial t = 0 \qquad \qquad \textit{Eq. 2-3}$$

$\textit{where } D_1 = \int_0^h \int_0^y f_\xi \, d\xi \, dz - D_2 \int_0^h f_\xi \, d\xi \,, D_2 = \dfrac{\int_0^h \int_0^y f_1 \, d\xi \, dz}{\int_0^h f_1 \, d\xi}, f_\xi = \dfrac{\xi}{\mu}, f_1 = \dfrac{1}{\mu}$

Fig. 2-2 shows the unwrapped surfaces of the bearing and the journal, note that x axis is the bearing circumferential direction, y is the cross-film direction, z is the bearing axial direction. In previous research [31, 39] h is only a function of x and t and is uniform along the z axis. The current research of ME includes the shaft and bearing asymmetric thermal expansion and misalignment in the axial direction, and thus h can also vary along z axis. The solution of Eq. 2-3 is the film pressure P, which varies in x and z direction.
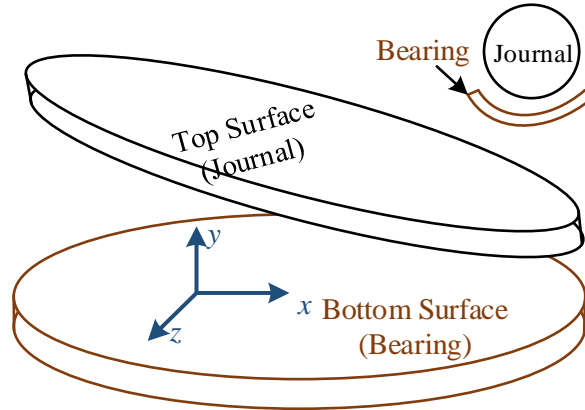
Fig. 2-2 Unwrapped surfaces of bearing and journal.

The governing Eq. 2-3 is solved by the finite element method (FEM) with 2D triangular elements and all the matrices of FEM are detailed in the appendix. The boundary conditions for the Reynolds equation is shown in Fig. 2-3, where the pad leading edge is imposed with supply oil temperature, and the trailing edge as well as the side boundaries

are prescribed with zero gauge pressure. The negative nodal pressure solved by the FEM

may cause cavitation and is thus reset to be zero, and the detailed processed can be found

in appendix.
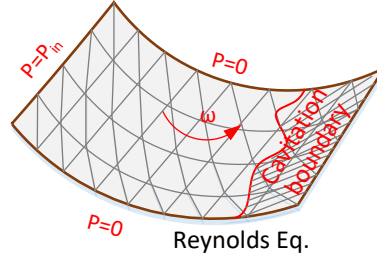
Fig. 2-3 Boundary conditions for the Reynolds equation.

As shown in Eq. 2-4, the velocity profile can be evaluated with the pressure

distribution from Reynolds equation. In the conventional two-dimensional analysis, the

velocity profile is obtained only at the bearing axial center. In current research, the axial

variation of velocity is also included to provide 3D nodal velocity profile for the energy

equation solver.

$$u = \left(\int_0^y f_\xi d\xi - \frac{\int_0^h f_\xi d\xi}{\int_0^h f_1 d\xi} \int_0^y f_1 d\xi \right) \nabla P + \frac{\int_0^y f_1 d\xi}{\int_0^h f_1 d\xi} \cdot U, \ f_\xi = \frac{\xi}{\mu}, f_1 = \frac{1}{\mu} \qquad Eq.\ 2\text{-}4$$

2.1.3 Energy Equation

Accurate prediction of the energy equation is the prerequisite for Morton effect

analysis. First of all, the viscous shearing of the fluid film is the heat source for

temperature rise in the shaft and bearing. Also, the lubricant viscosity is highly

39

temperature dependent, which may further affect the bearing performance and the rotordynamics prediction.

The film temperature distribution is predicted by the energy equation, which requires the velocity distribution from the Reynolds equation. Assuming that the flow is incompressible and Newtonian, the energy equation can be found below in Eq. 2-5, where x, y, z are the film circumferential, radial and axial direction, respectively.

$$\rho c \left(\frac{\partial T}{\partial t} + u \frac{\partial T}{\partial x} + w \frac{\partial T}{\partial z} \right) = k \left(\frac{\partial^2 T}{\partial x^2} + \frac{\partial^2 T}{\partial y^2} + \frac{\partial^2 T}{\partial z^2} \right) + \mu [(\frac{\partial u}{\partial y})^2 + (\frac{\partial w}{\partial y})^2] \qquad Eq.\ 2\text{-}5$$

The traditional 2D energy equation neglected the temperature variation along the bearing axial direction, which was reported to overpredict the film temperature than the 3D energy equation [40]. The convection term on the left of Eq. 2-5 can cause numerical oscillation, which is suppressed by the quadratic up-winding scheme [55]. The time dependent lubricant temperature $\frac{\partial T}{\partial t}$ will not change the steady film temperature distribution, but is also included for transient analysis for Morton effect. Note that in practice the film temperature cannot immediately change with rotordynamics, instead, the film thermodynamics will lag the rotordynamics, causing a phase lag between the hot spot and high spot, especially at high speed. Neglecting the $\frac{\partial T}{\partial t}$ terms will always result in a zero phase lag, which will deteriorate the prediction accuracy. The 3D energy equation in Eq. 2-5 is solved by the FEM with 3D 8-node isoparametric elements, as shown in Fig. 2-4. The film leading edge is prescribed with oil inlet temperature, and the top film/journal

40

contacting surface is prescribed with the journal surface temperature, and the bottom film/bearing contacting surface is prescribed with bearing surface temperature.
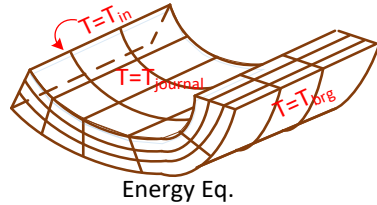
Fig. 2-4 Finite element mesh for the energy equation.

The inlet oil does not directly come from the fresh supply oil which is injected through nozzles from the external oil reservoir. Lots of research [40, 56, 57] show that significant amount of oil will be carried over from the previous pad trailing edge to the next pad leading edge, and thus the inlet oil is actually a mixture from both the hot oil carried over from the previous pad and the fresh oil supplied from extern system, as shown in Fig. 2-5. The inlet temperature of the oil is determined by the mixing of flow in Eq. 2-6, where Q indicates the flow rate, T is the oil temperature, the subscript "out" indicates the carry over flow at the pad trailing edge, "in" is the inlet flow at the next pad leading edge, the superscript 'i' is the pad number.

$$T_{in} = \frac{Q_{out}^{i-1} \cdot T_{out}^{i-1} + (Q_{in}^i - Q_{out}^{i-1}) \cdot T_{supply}}{Q_{in}^i} \qquad \qquad Eq.\ 2\text{-}6$$

Physically, after exiting the previous pad tailing edge, some flow may be carried over to the next pad and the rest will exit the bearing and return to the oil reservoir. This

flow mixing process is quite complicated physically and is thus simplified with the mixing coefficient λ, which is the percentage of the carry over flow Q_{out}^{i-1} over the total inlet flow Q_{in}^i. λ is estimated empirically based on lubrication mechanism and bearing design and was also measured by researchers in the past [56, 57]. If $Q_{out}^{i-1} > \lambda \, Q_{in}^i$, the recirculated flow is limited to $\lambda \, Q_{in}^i$, and if $Q_{out}^{i-1} < \lambda \, Q_{in}^i$, the conventional mixing Eq. 2-6 is used. The modified flow mixing equation is shown in Eq. 2-7.

$$T_{in} = \begin{cases} \dfrac{Q_{out}^{i-1} \cdot T_{out}^{i-1} + [Q_{in}^i - Q_{out}^{i-1}] \cdot T_{supply}}{Q_{in}^i} & if \; Q_{out}^{i-1} < \lambda Q_{in}^i \\[2ex] \dfrac{\lambda Q_{in}^i \cdot T_{out}^{i-1} + [Q_{in}^i - \lambda Q_{in}^i] \cdot T_{supply}}{Q_{in}^i} & if \; Q_{out}^{i-1} \geq \lambda Q_{in}^i \end{cases} \qquad \text{Eq. 2-7}$$
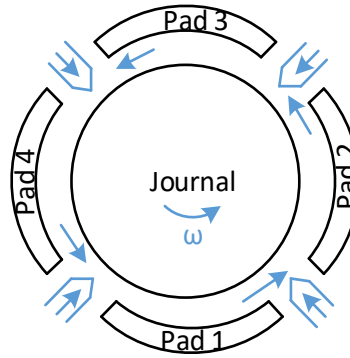
Fig. 2-5 Mixing of carry-over flow and supply flow.

2.1.4 Film Thickness Formula

The film thickness calculation should take into account both the pivot deformation and the thermal expansion of the journal and pads, as shown in Fig. 2-6. Considering that the latter can be highly asymmetric due to the non-uniform temperature distribution, a precise film thickness formula considering the radial and circumferential variation is

shown in Eq. 2-8, where h_{sft} and h_{pad} are the thermal expansion of the shaft and pads respectively.

$$h(\theta, z) = C_p - \hat{e}_x \cos(\theta) - \hat{e}_y \sin(\theta) - (C_p - C_b) \cos(\theta - \theta_p)$$

$$-\delta_{tilt} R \sin(\theta - \theta_p) - h_{\Delta T}(\theta, z) \qquad \text{Eq. 2-8}$$

,where $\hat{e}_x = e_x + z\theta_y - y_{pvt} \cos\theta_p$, $\hat{e}_y = e_y - z\theta_x - y_{pvt} \sin\theta_p$, $h_{\Delta T}(\theta, z) = h_{sft}(\theta, z) + h_{pad}(\theta, z)$.
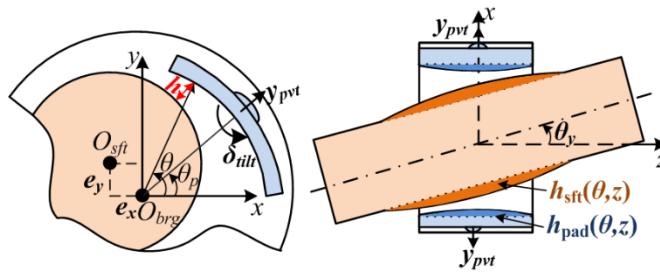
Fig. 2-6 Film thickness diagram.

2.2   Rotor and Bearing Temperature Model

Accurate prediction of the rotor and bearing temperature is necessary from two aspects: (a) the average temperature rise may cause thermal expansion, reducing the operational bearing clearance; (b) the temperature difference ΔT across the journal circumference will induce the ME, generating thermal imbalance. Among various types of hydrodynamic bearings, the tilting pad journal bearing (TPJB) is detailed herein due to its high stability and wide application. Analysis of other bearing types may be treated with a similar procedure.

The 3D heat conduction Eq. 2-9 is applied to both the rotor and TPJBs, and great care should be taken in selection of boundary conditions for the bearing and rotor surfaces, where users can choose (a) the prescribed convective boundary condition is applied with $q = \bar{h}(T - T^\infty)$, where $\bar{h}$ is the convection coefficient and T^∞ is the ambient temperature on surface S_h, (b) the heat flux q is prescribed as q^* on surface S_q, and (c) the temperature is prescribed as T^* on surface S_T. Note that ρ, c, k in Eq. 2-9 are the density, heat capacity and heat conductivity of the pad or rotor, respectively.

$$\frac{\partial^2 T}{\partial x^2} + \frac{\partial^2 T}{\partial y^2} + \frac{\partial^2 T}{\partial z^2} = \frac{\rho c}{k}\frac{\partial T}{\partial t} \qquad\qquad Eq.\ 2\text{-}9$$

The 3D FEM with 8-node iso-parametric elements is utilized, and thus Eq. 2-9 is transformed into Eq. 2-10, where $[T]$ is the nodal temperature vector. Note that $[F_T]$ is time dependent and thus should be updated temporally based on the boundary conditions between the journal\film and film\bearing.

$$[C_T][\dot{T}] + [K_T][T] = [F_T] \qquad\qquad Eq.\ 2\text{-}10$$

The boundary conditions between the bearing\lubricant and lubricant\journal are expressed by Eq. 2-11 and Eq. 2-12, both assuming that the temperature T and the heat flux $k\frac{\partial T}{\partial r}$ are continuous on the boundary surfaces. Note that the angular, radial and axial position is defined by (θ, r, z), and r_b and r_j are the bearing and journal radius. Also Eq. 2-11 accounts for the shaft speed ω and thus θ in the rotor rotational frame corresponds

to $(\theta + \omega t)$ in the lubricant fixed frame. In both equations, the subscript 'J', 'L' and 'B' indicate the journal, lubricant and bearing, respectively.

$$k_L \frac{\partial T_L}{\partial r}\big|_{(\theta+\omega t, r_j, z)} = k_J \frac{\partial T_J}{\partial r}\big|_{(\theta, r_j, z)}$$
$$T_L\big|_{(\theta+\omega t, r_j, z)} = T_J\big|_{(\theta, r_j, z)}$$

Eq. 2-11

$$k_L \frac{\partial T_L}{\partial r}\big|_{(\theta, r_b, z)} = k_B \frac{\partial T_B}{\partial r}\big|_{(\theta, r_b, z)}$$
$$T_L\big|_{(\theta, r_b, z)} = T_B\big|_{(\theta, r_b, z)}$$

Eq. 2-12

The temperature boundary surfaces of the rotor-bearing system are illustrated in Fig. 2-7, where only the surfaces of TR1 (thermal rotor 1, i.e. the rotor portion adjacent to bearing 1) and bearing 1 are numbered for illustration. At the beginning of each staggering cycle, the film temperature inside the bearing is solved with energy equation first, and then the nodal temperature on surface 3 (journal/film interface) and surface 8 (bearing/film interface) are updated based on Eq. 2-11 and Eq. 2-12 i.e., both surfaces are prescribed with S_T and S_q simultaneously. All other surfaces (except surface 5, which is assumed to be insulated due to the negligible temperature increase) for TR1 and bearing 1 are assumed to be exposed to the ambient and thus prescribed with convective boundary conditions S_h, as shown in Fig. 2-7. The boundary conditions of TR2 and bearing 2 are similar but with the left end surface insulated in TR2. The 3D transient rotor and bearing temperature distribution is achieved by numerically integrating Eq. 2-10 until the next staggering cycle. Earlier studies [13, 40, 44] reveal that the rotor temperature rise is only evident adjacent to the bearing location and decays fast outside the bearing length, making it possible to focus only on the "thermal rotor" rather than the entire physical rotor for temperature

calculation. Based on numerous numerical experiments, seven (7) times the bearing length is selected for the thermal rotor length. This selection balances the computation speed and predictive accuracy.
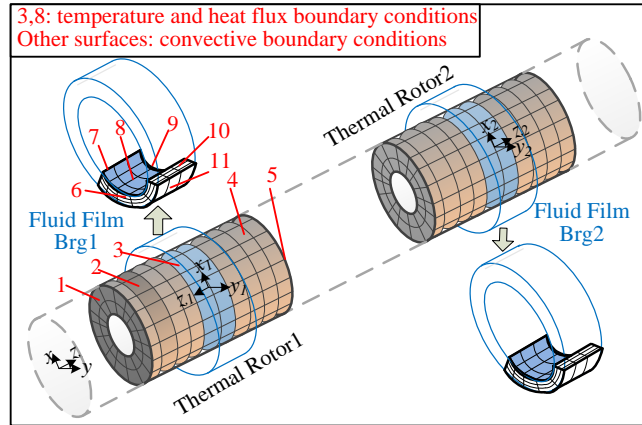
Fig. 2-7 Schematics of temperature boundary surfaces of the shaft and bearing.

The 3D energy equation is utilized to predict the lubricant temperature distribution which accounts for the temperature variation in the circumferential, radial and axial direction. The required 3D nodal velocity and pressure in the energy equation are provided by the Reynolds equation. Earlier studies used the 2D energy equation [26, 39] which is avoided in current simulations due to its neglect of axial temperature variation in lubricant. This has been shown to overpredict the ME in most cases [40] studied.

2.3   Rotor and Bearing Thermal Deformation Model

The 3D FEM is utilized to conduct the thermal deformation analysis, which shares the nodes and elements with the temperature analysis in section 2.2. Once the temperature

solver calculates the temperature rise of all nodes in the rotor and bearing, the thermal load vector $[F_{\Delta T}]$ will be applied to these nodes to calculate the thermal expansion based on Eq. 2-13, which is derived from the equilibrium equation and constitutive equation. Note that $[X_{\Delta T}]$ is the nodal thermal deformation vector and $[X_{\Delta T}]_i = [\Delta x_i, \Delta y_i, \Delta z_i]^T$ for node i.

$$[K_{\Delta T}][X_{\Delta T}] = [F_{\Delta T}] \qquad\qquad Eq.\ 2\text{-}13$$

2.3.1 Boundary Conditions for Rotor

The asymmetric rotor thermal expansion reduces the bearing clearance and also generates equivalent thermal imbalances due to the thermal bow. Current research abandons the assumptions in earlier studies where the journal temperature is linear radially and uniform axially and the thermal deflection is estimated by certain analytical expressions [11, 17, 26, 31, 38, 39, 47].

Boundary conditions should be carefully handled to provide realistic deformation and avoid singular matrixes in the FEM solution. Considering that the temperature rise is negligible outside the thermal rotor (TR), the TR is assumed to be a cantilever with fixed DOFs on the right section of TR1 and left section of TR2, which is illustrated in Fig. 2-8. Note that on the left section, the nodal DOFs are fully fixed for the innermost layer and are fixed axially for other nodes. TR1 has similar boundary conditions as TR2.
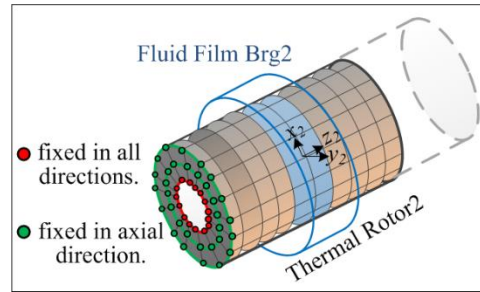
Fig. 2-8 Boundary conditions for rotor thermal deformation.

The rotor thermal bow induced by the asymmetric thermal load is shown in Fig. 2-9. Note that the rotor centerline deviates from the horizontal position due to the non-even radial expansion. For nodes located between both TRs, the thermal bow is zero (dashed rectangle); for nodes within TRs, shaded in Fig. 2-9, the nodal thermal bow is directly calculated by the FEM and expressed with (e_{Tn}, Φ_{Tn}) for magnitude and phase; for nodes close to both rotor ends, the thermal bow is the linear extension of the TR end. Detailed expressions of the thermal bow magnitude $e_{\Delta t,n}$ and phase $\Phi_{\Delta t,n}$ can be found in Eq. 2-14 and Eq. 2-15.
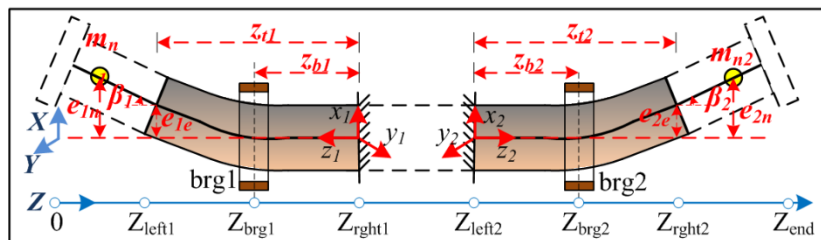
Fig. 2-9 Configuration for determining rotor thermal bow.

$$e_{\Delta t,n}(z) = \begin{cases} e_{1e} + (Z_{left1} - z)sin(\beta_1), & 0 \leq z < Z_{left1} \\ e_{Tn1}, & Z_{left1} \leq z \leq Z_{rght1} \\ 0, & Z_{rght1} < z < Z_{left2} \\ e_{Tn2}, & Z_{left2} \leq z \leq Z_{rght2} \\ e_{2e} + (z - Z_{rght2})sin(\beta_2), & Z_{rght2} < z \leq Z_{end} \end{cases} \qquad Eq.\ 2\text{-}14$$

$$\Phi_{\Delta t,n}(z) = \begin{cases} \Phi_n(Z_{left1}), & 0 \leq z < Z_{left1} \\ \Phi_{Tn1}, & Z_{left1} \leq z \leq Z_{rght1} \\ 0, & Z_{rght1} < z < Z_{left2} \\ \Phi_{Tn2}, & Z_{left2} \leq z \leq Z_{rght2} \\ \Phi_n(Z_{rght2}), & Z_{rght2} < z \leq Z_{end} \end{cases} \qquad Eq.\ 2\text{-}15$$

In accordance with [40], a distributed thermal imbalance force in Eq. 2-16 is used to model the ME with its nodal magnitude proportional to the nodal mass m_n and the nodal thermal bow $e_{\Delta t,n}$. Note that $[F_{xT}]$ and $[F_{yT}]$ are the imbalance projections in two lateral directions, and N is the node quantity. Compared with the earlier studies which model the thermal bow with a lumped imbalance located at the overhung node [10-16], the distributed model takes into account the rotor configuration, and thus is more consistent with the actual machine build.

$$\begin{cases} [F_{xT}]_{N\times1} = [m_n e_{\Delta t,n}\omega^2 cos(\omega t + \Phi_{\Delta t,n})]_{N\times1} \\ [F_{yT}]_{N\times1} = [m_n e_{\Delta t,n}\omega^2 sin(\omega t + \Phi_{\Delta t,n})]_{N\times1} \end{cases} \qquad Eq.\ 2\text{-}16$$

The approach above to model the rotor thermal bow with equivalent thermal imbalance is termed "imbalance method" and is discussed in Section 3. Another different method to model the rotor thermal bow will also be introduced in Section 4 to improve the accuracy.

2.3.2　Boundary Conditions for Bearing

Due to the lubricant heating and the bearing housing restraint, the TPJB pads will expand inwards and thus reduce the bearing clearance. In practice, various bearing pivots and mechanical features are designed to provide various restrictions for pad DOFs, which are imposed as boundary conditions in the FEM to obtain accurate pad thermal deformation. Fig. 2-10 illustrates the boundary conditions for a TPJB pad with a cylindrical pivot. x, y, z are the tangential, radial and axial axis, respectively. For a pivot with 50% offset, the center node on the bottom surface is fully constrained in all directions. Other nodes on the bottom centerline are constrained in the x and y direction, allowing for the axial thermal expansion. The center point on the top surface is constrained in the x and z, allowing for the radial expansion. For a pad with a non-50% offset, the prescribed nodes will align with the pivot in the y-z plane.
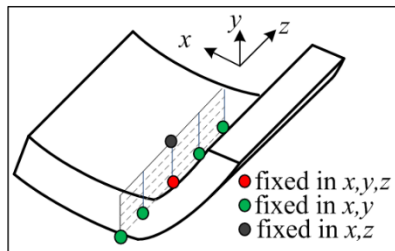
Fig. 2-10 Pad boundary conditions for bearing thermal deformation modeling.

2.4　Bearing Dynamics Model

The bearing pivot and pad deformation should be considered in the bearing dynamic model due to their significant effect on the bearing clearance and dynamic

coefficients. The pivot flexibility is reported to outweigh the pad flexibility for possibly reducing the bearing dynamic coefficients and lowering the critical speeds [58]. Current research employs two different models, i.e. the rigid pad model and the flexible pad model for bearing dynamics calculation. Both models account for the pivot flexibility and pad thermal deformation, while the rigid pad model neglects the pad elastic deformation caused by the hydrodynamic force and is more computationally efficient than the flexible pad model.

In the rigid model, the pad can only tilt and translate about the pivot and no elastic deformation is required. The pivot deformation y_{pvt} and stiffness k_p are calculated based on the Hertzian contact theory [59]. Quite differently, in the flexible model, the pad nodal deformation is calculated by the 3D FEM. The free body diagram of the rigid pad model is shown in Fig. 2-11, where the pivot location P may differ from the mass center G for the asymmetric pivot offset. The zero y_{pvt} indicates zero pivot force F_{pvt}, and the zero tilting angle δ_{tilt} indicates that the line GP aligns with x axis. p_i and f_i are the normal and viscous force calculated by the Reynolds equation for node i. The dynamic equations of the rigid pad model is shown in Eq. 2-17, where p_{iy}, f_{iy} are the y components of p_i, f_i, and M_{pi}, M_{fi} are the nodal moments about G caused by p_i and f_i.

$$\begin{cases} M_G \ddot{y}_G = -k_p y_{pvt} + \Sigma p_{iy} + \Sigma f_{iy} \\ I_G \ddot{\delta}_{tilt} = -k_p y_{pvt} x_G + \Sigma M_{pi} + \Sigma M_{fi} \end{cases} \text{ where } \begin{cases} x_G = -e_G \cos(\delta_{tilt}) \\ y_G = y_{pvt} + e_G \sin(\delta_{tilt}) \end{cases} \qquad Eq.\ 2\text{-}17$$
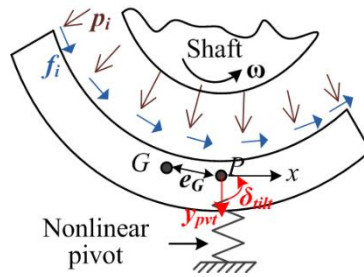
Fig. 2-11 Free body diagram of the rigid pad.
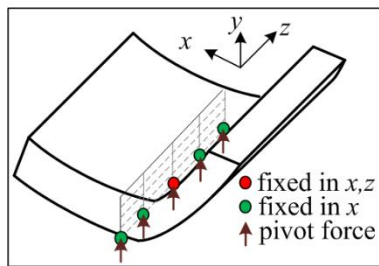
Fig. 2-12 Restricted DOFs of the flexible pad.

The restricted degree of freedom (DOF) of the flexible pad with the cylindrical pivot is illustrated in Fig. 2-12. Note that the pad is allowed to move along the y axis due to the pivot deformation. To predict the transient dynamic response of the flexible pad model and also improve the computational efficiency, the modal reduction method is employed, where the lowest 25% of the modes (corresponding to the lowest 25% eigenvalues) are selected to provide satisfactory estimation and sufficient computational speed. Note that the rigid body modes of the flexible pad correspond to the titling and translation motion in the rigid pad, and thus the flexible model is theoretically more accurate than the rigid model considering that it also takes the flexible modes into account. The governing equations before and after modal reduction for the flexible pad model are

expressed in Eq. 2-18 and Eq. 2-19, where $[\Psi_L]$ and $[\Psi_R]$ are composed by selected left

and right eigenvectors of $[\bar{M}]$, λ is the corresponding eigenvalue.

$$[M]_p\ddot{X}_p + [K]_p X_p = [F]_p \qquad\qquad Eq.\ 2\text{-}18$$

$$[diag(\lambda_1, \dots, \lambda_k)]\dot{Z} = [\Psi_L]^T[\bar{M}][\Psi_R]Z + [\Psi_L]^T[\bar{F}], \qquad\qquad Eq.\ 2\text{-}19$$

where $[\bar{M}] = \begin{bmatrix} 0 & -M_p^{-1}K_p \\ I & 0 \end{bmatrix}, [\bar{F}] = \begin{bmatrix} -M_p^{-1}F_p \\ 0 \end{bmatrix}, \begin{bmatrix} \dot{X}_p \\ X_p \end{bmatrix} = [\Psi_R]Z$

3 MORTON EFFECT PREDICTION ALGORITHM

(I) – THERMAL IMBALANCE METHOD*

The Morton effect instability is mostly reported in turbomachinery with overhung mass, which can be couplings, gears, compressor or turbine disks, etc. The asymmetric heating due to the uneven viscous shearing of the film inside the hydrodynamic bearing may bend the shaft, and if the overhung mass happens to be on the same side, the thermal bow may cause large deflection at the overhung location. Most previous prediction methods modeled the bowed rotor with either a lumped thermal imbalance at the overhung location [12, 31, 38, 39] or distributed imbalance along the shaft [40]. Under certain conditions, the thermal imbalance may boost the rotor vibration and cause larger temperature difference across the journal circumference, and if the positive feedback is formed, the rotor vibration may grow continuously until the rotor is tripped before significant damage is caused. The rotor may have a single-overhung configuration or have overhung masses at both rotor ends, i.e., double-overhung configuration, as shown in Fig. 3-1. The single overhung rotor focuses on the thermal bow only on one side of the rotor, however, the double overhung rotor requires the prediction of thermal bow on both sides. Note that the thermal bow on both sides of the double overhung rotor does not need to be in phase or out of phase and both its magnitude and direction can be speed or even time dependent. In additional, changing the thermal bow on one rotor side can affect the

---

rotordynamics as well as the thermal bow on the other side, making the prediction more complicated.
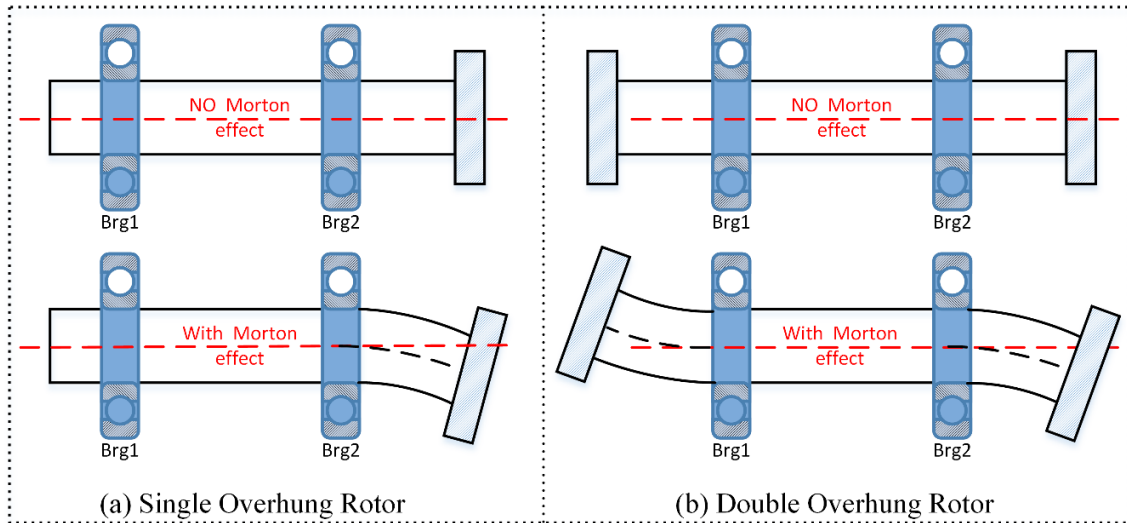
Fig. 3-1 Single and double overhung rotor configuration.

3.1   Prediction Algorithm based on Thermal Imbalance Method

3.1.1   Calculation of Resultant Imbalance

The thermal imbalance method simplifies the rotor thermal bow into distributed thermal imbalance, as discussed in Section 2.3.1. The resultant imbalance is thus the vector summation of mechanical imbalance and thermal imbalance. Besides the mechanical imbalance, the residual bow (RB) and disk skew (DS) can also create synchronous dynamic excitation [60-63]. Considering that both the RB and DS are commonly present in all shaft assemblies due to tolerances or heat treatment, they are included in the current rotor dynamic model together with the mechanical and thermal

55

imbalance. Fig. 3-2 shows a diagram that depicts the various synchronous force excitations. Note that both the DS and RB are assumed to be constant in magnitude, making their projections sinusoidal in the two lateral directions.
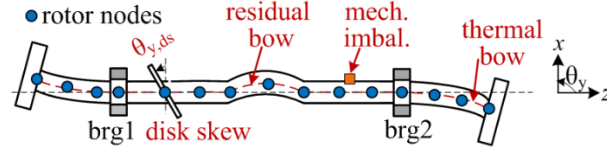
Fig. 3-2 Depiction of synchronous force sources on a flexible rotor model.

For sake of illustration an Euler-Bernoulli beam model with 4 lateral DOFs for each node, θ_x, θ_y, x, y, is utilized for the rotordynamic analysis. With the RB modeled with equivalent imbalances and also assuming that all components are small, the resultant imbalances are the linear superposition of the mechanical, thermal and RB induced imbalance, shown in Eq. 3-1, where $\overline{me}_n$ and Ψ_n are the nodal magnitude and phase of the mechanical imbalance, $e_{n,rb}$ and Θ_n are the nodal amplitude and phase angle of RB.

$$\begin{cases} [F_{x,im}]_n = \omega^2[\overline{me}_n \cos(\omega t + \Psi_n) + m_n e_{\Delta t,n} \cos(\omega t + \Phi_{\Delta t,n}) + m_n e_{n,rb} \cos(\omega t + \Theta_n)] \\ [F_{y,im}]_n = \omega^2[\overline{me}_n \sin(\omega t + \Psi_n) + m_n e_{\Delta t,n} \sin(\omega t + \Phi_{\Delta t,n}) + m_n e_{n,rb} \sin(\omega t + \Theta_n)] \end{cases} \quad \text{Eq. 3-1}$$

The DS also contributes to the synchronous force, expressed in Eq. 3-2, where $\tilde{\theta}_{xn} = -\theta_{ds,n} \sin(\omega t + \varphi_n)$, $\tilde{\theta}_{yn} = \theta_{ds,n} \cos(\omega t + \varphi_n)$, and $\theta_{ds,n}$ and φ_n are the nodal magnitude and phase of disk skewed angles. Note that $\tilde{\theta}_{xn}$ and $\tilde{\theta}_{yn}$ are the lateral projections of the DS sensed in the stationary frame and obey the right hand rule, and for the instant shown in Fig. 3-2, $\varphi_n = 0$.

$$[F_{ds}]_n = [F_{xn}, F_{yn}, M_{xn}, M_{yn}]_{ds}^T = [0,0, \omega^2(I_T - I_p)\tilde{\theta}_{xn}, \omega^2(I_T - I_p)\tilde{\theta}_{yn}]^T \qquad Eq.\ 3\text{-}2$$

Therefore, the governing equation for the rotor dynamics has the following standard form, where $[U]$ includes all rotor DOFs.

$$[M_{rot}][\ddot{U}] + [C_{rot}][\dot{U}] + [K_{rot}][U] = [F] = [F_{im} + F_{gyo} + F_{brg} + F_{ds} + F_{ext}] \quad Eq.\ 3\text{-}3$$

Note that the dynamic coefficients of linear bearings, seals and couplings are incorporated into the $[C_{rot}]$ and $[K_{rot}]$. $[F_{im}]$ is the resultant imbalance vector including the mechanical, thermal imbalance and the RB. $[F_{brg}], [F_{gyro}]$ and $[F_{ext}]$ are the hydrodynamic bearing force, gyroscopic force and other external forces applied on the rotor.

The nonlinear transient rotordynamic response is calculated by solving Eq. 3-3 and the transient bearing orbits are then obtained from the bearing nodal components in the displacement vector $[U]$. Bearing vibrations that exhibit ME symptoms and in particular those causing the vibration amplitude to exceed the threshold in API 617 [48], or the minimum film thickness to drop below the allowable ratio, provide an indication that the system design should be optimized to avoid ME induced instability.

3.1.2 Transient Algorithm for Morton Effect Prediction

Fully nonlinear double overhung method

The ME prediction comprises three coupled sub-problems. (1) The transient rotor & bearing dynamics and the transient lubricant temperature distribution. In the algorithm, one single orbit will be divided into dozens of segments and within each segment, the

Reynolds Eq. 2-3 will be utilized for hydrodynamic pressure calculation; Eq. 2-8, Eq. 2-17, Eq. 2-18, Eq. 2-19 and Eq. 3-3 will be used for transient rotordynamics prediction; the energy Eq.2-5 will be solved for lubricant temperature and viscosity at each segment end. (2) The transient temperature distribution in the rotor & bearings. By assuming that the temperature and heat flux are continuous on the journal-film, bearing-film boundaries, the thermal rotor and bearing temperature will be solved by. Note that this process is purely thermal and no rotordynamic analysis is required. (3) The asymmetric rotor & bearing thermal expansion and the resulted thermal imbalance due to thermal bow. Based on Eq. 2-10, the 3D FEM will be applied to the rotor & bearings to calculate the thermal expansion, which is used to update the film thickness in Eq. 2-8. The thermal bow caused by the asymmetric rotor expansion is modeled with equivalent thermal imbalance based on Eq. 2-14, Eq. 2-15 and Eq. 2-16, and will be incorporated into the synchronous excitation in Eq. 3-1 for the transient rotordynamic analysis in sub-problem (1).

Considering that the numerical simulation cannot be physically multitasking, the aforementioned sub-problems have to be tackled successively within each short interval Δt_n, and then the viscosity, temperature, film thickness, and thermal bow will be updated, preparing for the next Δt_{n+1}. Considering that the rotor and bearing temperature response is significantly slower than the rotordynamics, the latter will soon converge before updating the rotor and bearing temperature, which may refresh the converged dynamic status by changing the film thickness and thermal imbalance. Following the authors' previous research [39, 40], the staggered integration scheme is applied to achieve high computational efficiency without unduly sacrificing accuracy. In this method, ① the

thermal-structural solver (sub-problem 1), where both the lubricant temperature and rotor vibration is updated, is integrated over a short period, followed by ② the temperature solver (sub-problem 2) integrated over a longer period to update the system temperature and the rotor thermal bow (sub-problem 3). As shown in Fig. 3-3, the integration time for solver 1 is shorter than solver 2, and in the current simulation $t_{span2} = 200t_{span1}$, where the ratio 200 is selected based on experience considering the rotor & bearing thermal constants and operational speed.
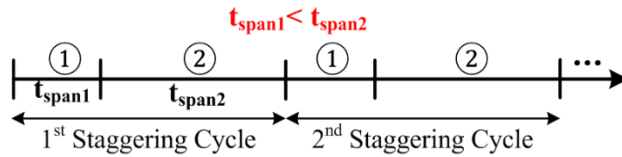
Fig. 3-3 Staggered integration scheme.

Linear method

Quite different from the nonlinear method, which predicts the transient rotor dynamics by solving the bearing hydrodynamic force at each time step, the linear method estimates the bearing force with pre-calculated dynamic coefficients, which are then incorporated into the rotor matrix to assemble the global dynamic matrix. The system steady state frequency response is calculated by premultiplying the synchronous force vector by the inverse of the global dynamic coefficient matrix at each speed. The full stiffness and damping matrix of a TPJB with the cylindrical pivot and rigid pad model are shown in Eq. 3-4, where x, y are the journal center position, $\delta_1, \dots, \delta_n$ are the pad tilting

angles, $p_1, \dots, p_n$ are the pivot displacements. For the flexible pad model, the tilting angles and pivot displacements are replaced with modal components and thus the matrix dimension are usually bigger.

$$[K_b] = \begin{bmatrix} k_{xx} & k_{xy} & k_{x\delta_1} & \cdots & k_{x\delta_n} & k_{xp_1} & \cdots & k_{xp_n} \\ k_{yx} & k_{yy} & k_{y\delta_1} & \cdots & k_{y\delta_n} & k_{yp_1} & \cdots & k_{yp_n} \\ k_{\delta_1 x} & k_{\delta_1 y} & k_{\delta_1 \delta_1} & \cdots & k_{\delta_1 \delta_n} & k_{\delta_1 p_1} & \cdots & k_{\delta_1 p_n} \\ \vdots & \vdots & \vdots & \cdots & \vdots & \vdots & \cdots & \vdots \\ k_{\delta_n x} & k_{\delta_n y} & k_{\delta_n \delta_1} & \cdots & k_{\delta_n \delta_n} & k_{\delta_n p_1} & \cdots & k_{\delta_n p_n} \\ k_{p_1 x} & k_{p_1 y} & k_{p_1 \delta_1} & \cdots & k_{p_1 \delta_n} & k_{p_1 p_1} & \cdots & k_{p_1 p_n} \\ \vdots & \vdots & \vdots & \cdots & \vdots & \vdots & \cdots & \vdots \\ k_{p_n x} & k_{p_n y} & k_{p_n \delta_1} & \cdots & k_{p_n \delta_n} & k_{p_n p_1} & \cdots & k_{p_n p_n} \end{bmatrix},$$

$$[C_b] = \begin{bmatrix} c_{xx} & c_{xy} & c_{x\delta_1} & \cdots & c_{x\delta_n} & c_{xp_1} & \cdots & c_{xp_n} \\ c_{yx} & c_{yy} & c_{y\delta_1} & \cdots & c_{y\delta_n} & c_{yp_1} & \cdots & c_{yp_n} \\ c_{\delta_1 x} & c_{\delta_1 y} & c_{\delta_1 \delta_1} & \cdots & c_{\delta_1 \delta_n} & c_{\delta_1 p_1} & \cdots & c_{\delta_1 p_n} \\ \vdots & \vdots & \vdots & \cdots & \vdots & \vdots & \cdots & \vdots \\ c_{\delta_n x} & c_{\delta_n y} & c_{\delta_n \delta_1} & \cdots & c_{\delta_n \delta_n} & c_{\delta_n p_1} & \cdots & c_{\delta_n p_n} \\ c_{p_1 x} & c_{p_1 y} & c_{p_1 \delta_1} & \cdots & c_{p_1 \delta_n} & c_{p_1 p_1} & \cdots & c_{p_1 p_n} \\ \vdots & \vdots & \vdots & \cdots & \vdots & \vdots & \cdots & \vdots \\ c_{p_n x} & c_{p_n y} & c_{p_n \delta_1} & \cdots & c_{p_n \delta_n} & c_{p_n p_1} & \cdots & c_{p_n p_n} \end{bmatrix} \qquad \textit{Eq. 3-4}$$

The $[K_b]$, $[C_b]$ of each TPJB will be integrated into the rotor stiffness matrix $[K_{rot}]$, $[C_{rot}]$ to form the entire rotor-bearing stiffness matrix $[K_{rb}]$ and damping matrix $[C_{rb}]$. The final state vector $[U_{rb}]$ comprises the rotor nodal DOFs, $x_i, y_i, \theta_{xi}, \theta_{yi}$, plus the pad nodal DOFs, i.e. δ_i, p_i of the rigid pad model or modal components of the flexible pad model. The governing dynamic equation for the linear transient model is listed in Eq. 3-5, where F_{im} (see Eq. 3-1) includes the mechanical, thermal and RB induced imbalance vector, and F_{ds} (see Eq. 3-2) is the DS induced moment vector.

$$[M_{rb}]\ddot{U}_{rb} + [C_{rb}]\dot{U}_{rb} + [K_{rb}]U_{rb} = [F_{syn}] = [F_{im}] + [F_{ds}] \qquad \textit{Eq. 3-5}$$

60

Within each rotor revolution, assuming that $[U_{rb}] = [\widehat{U}_{rb}]e^{i\omega t}$, $[F_{syn}] = [\widehat{F}_{syn}]e^{i\omega t}$, the complex variables $[\widehat{U}_{rb}]$ can be expressed by Eq. 3-6.

$$[\widehat{U}_{rb}] = (-\omega^2[M_{rb}] + i\omega[C_{rb}] + [K_{rb}])^{-1}[\widehat{F}_{syn}] \qquad\qquad Eq.\ 3\text{-}6$$

By updating $[C_{rb}]$, $[K_{rb}]$ and $[F_{syn}]$ with respect to time and speed, $[\widehat{U}_{rb}]$ can be used to express the transient rotor and bearing dynamics $[U_{rb}]$. Note that in the linear analysis, the lubricant temperature and viscosity are also updated in each orbit segment (one orbit is divided into dozens of segments), similar to the nonlinear analysis. Nevertheless, the linear method omits the transient hydrodynamic force calculation, and thus is much faster than the nonlinear method. However, when the bearing orbit grows larger, the accuracy of the linear method deteriorates considering that the rotor dynamics cannot be simplified by the dynamic coefficients at the journal equilibrium position.

Single-overhung-wise method

This method assumes that the hydrodynamic bearing on one side is more likely to experience the ME than the other side, and thus the double overhung rotor model can regress towards the single overhung model, where only the bearing of interest will be analyzed for ME to calculate the transient hydrodynamic pressure, film & bearing & shaft temperature, bearing & shaft thermal expansion, etc. Meanwhile other bearings are simplified as a non-hydrodynamic bearing with speed-dependent dynamic coefficients, and thus no ME analysis will be applied, i.e. no thermal imbalance will be generated by these bearings. For certain rotor structures, it is not obvious which bearing is prone to the ME, and thus a conservative approach is suggested by applying the single-overhung-wise

method (SOWM) for both rotor ends independently. One may analyze bearing one first (meanwhile bearing two is treated as a non-ME bearing), and then analyze bearing two (meanwhile bearing one is treated as a non-ME bearing). This assumes that the ME induced problems at both ends are non-coupled and thus can be analyzed independently.

3.2 Case Verification with the Imbalance Method

A centrifugal compressor supported by two oil-lubricated TPJBs was reported to experience high synchronous vibration and could not achieve the maximum continuous speed of 11947 rpm [12]. Detailed dynamic analysis showed that the vibration at the left non-drive end (NDE) bearing exhibited synchronous vibration hysteresis and increasing vibration level at constant speed, which are characteristic of the ME. The compressor has a double overhung structure and the rotor configuration is illustrated in Fig. 3-4, where the NDE and DE TPJBs are located at node 7 and 29 respectively. The mechanical imbalance is attached on node 4 with a magnitude of $2.8 \times 10^{-4} kg \cdot m$ and initial phase of zero. Both bearings are identical in configuration and detailed parameters can be referred to in Table 3-1. Without specification, all simulation parameters in this paper are consistent with the settings in Table 3-1
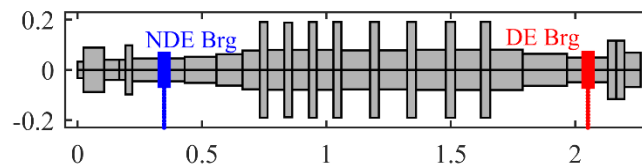
Fig. 3-4 Rotor configuration.

Table 3-1 Parameters of the rotor-bearing system model

Lubricant parameters		Bearing parameters	
Viscosity at 50 ℃ [Ns/m^2]	0.0203	Pad type	Load on pad
Viscosity coefficients [1/℃]	0.031	No. pads	5
Supply temperature [℃]	50	Radius of shaft [m]	0.049
Inlet pressure [Pa]	1.32×10^5	Radial bearing clearance [m]	7.35×10^{-5}
Reference temperature [℃]	50	Preload	0.5
Shaft Parameters		Bearing length[m]	0.049
Heat capacity [J/kg ℃]	453.6	Pad arc length[degree]	56
Heat conductivity [W/mK]	50	Density[kgm^3]	7850
Thermal expansion coeff.[1/℃]	1.1×10^{-5}	Heat conductivity [W/mK]	50
Reference temperature [℃]	30	Thermal expansion coeff. [1/℃]	1.1×10^{-5}
Thermal rotor length [m]	0.349	Reference Temperature [℃]	30

3.2.1   Critical Speed and Mode Shape Analysis

de Jongh reported that the vibration level was quite sensitive to the coupling weight and the final solution to this ME problem included the reduction of overhung mass by installing a lighter coupling on the NDE [12]. Rotordynamic analysis of the original rotor without coupling mass on the NDE predicted the 1st bending mode at 4 krpm and the 2nd bending mode at 14 krpm. Then a coupling of 6 kg is added to the rotor NDE for more accurate prediction, and the initial imbalance of $2.8 \times 10^{-4} kg \cdot m$ is attached on node 4 to analyze the unbalance response, which is plotted in Fig. 3-5 as well as the 2nd bending mode. Note that all predictions in Fig. 3-5 are based on a conventional treatment of both bearings with linear force coefficients. Fig. 3-5(a) shows that the first peak occurring at

the 1st critical speed is still around 4kpm, while the 2nd critical speed is shifted to 12 krpm, proving that the 2nd critical speed is very sensitive to the mass distribution on the NDE. Moreover, the 2nd bending mode shape, characterized by a large vibration amplitude on the NDE, may facilitate the ME development due to the severe viscous shearing induced by the large orbit in the NDE-bearing and the dominating thermal imbalance on the rotor NDE.
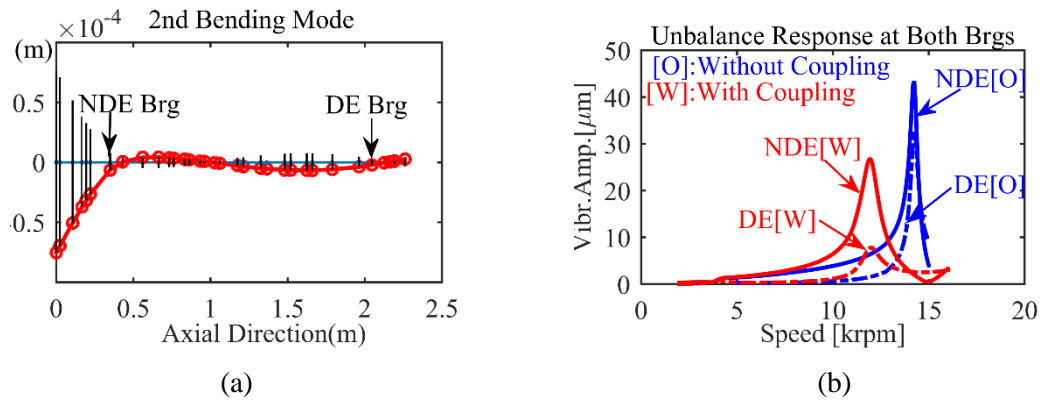
Fig. 3-5 (a) 2nd bending mode shape (b) linear unbalance response at bearings with/without coupling.

3.2.2 Morton Effect Induced Hysteresis

Hysteresis is frequently observed in the thermally induced vibration problem, where the vibration level in the coast-down testing is higher than the run-up testing. Earlier studies have reported the hysteresis behavior in several ME-induced instability cases [20, 49]. Based on the aforementioned rotor model, the nonlinear transient analysis is performed during which the shaft speed increases linearly from 9 krpm to 12 krpm within 1 min and decreases to 9 krpm following the same speed curve. The simulation results are

listed in Fig. 3-6 with the fully nonlinear transient method (see Section 3.1.2) designed for double overhung rotors.
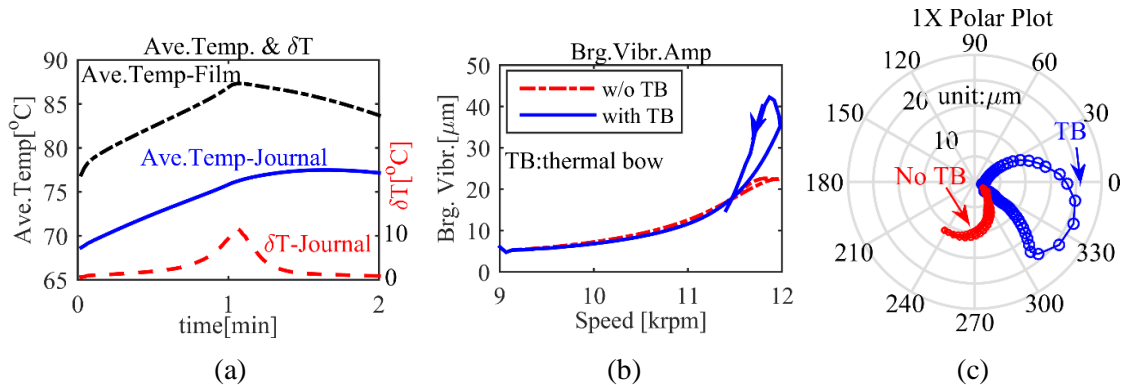
Fig. 3-6 Morton Effect hysteresis at the NDE bearing.(a)Average temperature and PK-PK ΔT, (b) PK-PK vibration amplitude at the bearing w. and w.o. thermal bow, (c) 1X vibration polar plot at the bearing.

Fig. 3-6(a) illustrates the transient average temperature of the film and journal when the ME is considered. Note that the average journal temperature still increases after the operational speed decelerates at t=1 min and then drops slowly to 77^oC, which is still higher than the initial temperature. The journal ΔT, which describes the peak-peak temperature difference across the journal circumference (this journal ΔT is also the maximum value in all cross sections along the journal axial direction) in all following results, increases to its peak value of 12^oC at t= 64 s when the vibration is the maximum. Fig. 3-6(b) shows that including the ME, i.e., including the thermal bow effect, causes a clear hysteresis loop, which is quite evident since the coast-down vibration level is much larger than run-up level. This phenomenon disappears when the ME is neglected. The 1X polar plot in Fig. 3-6(c) shows a spiral vibration with continuously changing phase angle

induced by the ME compared with non-ME case. The hysteresis is due to the slow recovery of the shaft temperature. The thermal imbalance caused by the ME significantly amplifies the vibration level compared with the non-ME case.

3.2.3 Algorithm Validation with Nonlinear Steady State Analysis

In contrast with classic frequency analysis in control theory, the steady state analysis in this paper adopts the fully nonlinear transient analysis (see Section 3.1.2) to acquire the steady state harmonic vibration and temperature at different rotational speeds. The objective is to clearly illustrate the rotor dynamics in the speed domain and determine the ME instability onset speed for this double overhung rotor. The algorithm begins at the lowest speed of interest, performing a nonlinear transient ME analysis at this fixed speed. When both the rotordynamics and thermodynamics converge, the rotor vibration amplitude and phase angle as well as the temperature distribution in the shaft & lubricant & bearing will be recorded. If the system exhibits divergence, simulations will halt at the current speed and all state variables will be saved before the instability drives the minimum film thickness below the threshold ($10\% C_b$ in current simulations), causing an energy equation solution failure. Afterwards, all thermal and dynamic state variables will be transmitted to the next speed as initial conditions. Then simulations will restart for the next speed until all speeds are finished and the vibration and temperature will be plotted with respect to rotational speeds. The steady state results of the aforementioned rotor are illustrated in Fig. 3-7. Without specification, the ambient temperature is $30^o C$ and the convective boundary conditions are imposed onto the corresponding surfaces of the bearing and thermal rotor with convective coefficient of $50 \text{ W}/(\text{m}^2\text{K})$ in all simulations.
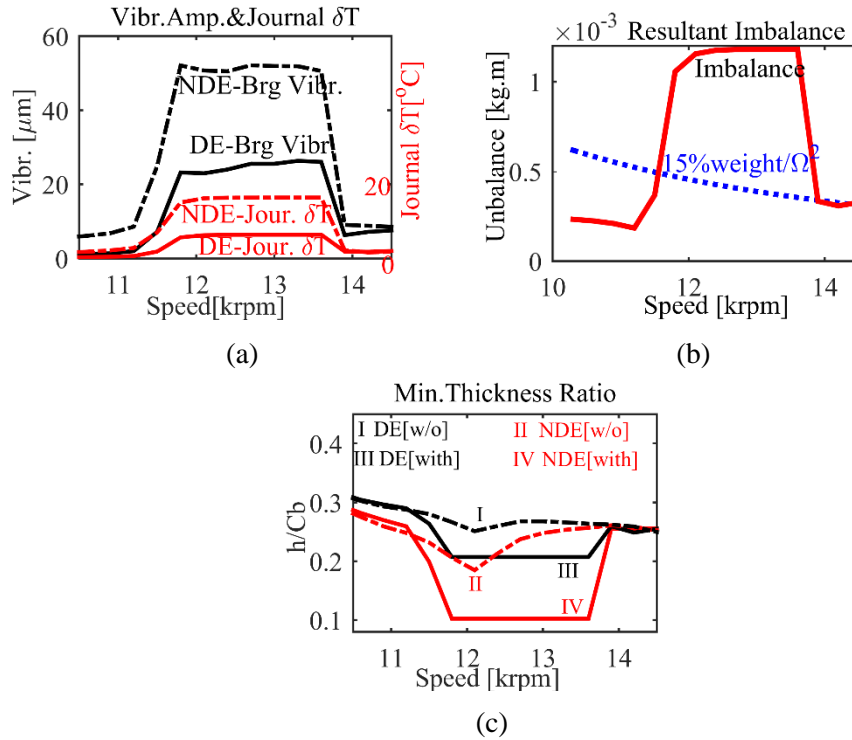
Fig. 3-7 Steady state ME analysis. (a) PK-PK bearing vibration amplitude and PK-PK journal ΔT (b) Resultant imbalance (c) Minimum film thickness ratio with and without the Morton effect.

Fig. 3-7(a) shows that the vibration amplitude increases drastically over 11.8 krpm for both bearings and the NDE bearing is much larger than the DE bearing. The vibration trend coincides with the journal ΔT, confirming that the vibration is closely related to the ME. Fig. 3-7(b) illustrates the resultant imbalance summed by the initial mechanical imbalance and the ME-induced thermal imbalance, and the latter grows quickly with speed and soon becomes dominating above 11.8 krpm. The minimum film thickness ratio is shown in Fig. 3-7(c), where both the ME and non-Morton cases (only for this sub-figure) are illustrated. Note that after taking into account the ME (i.e., including the thermally induced imbalance), the film thickness is greatly reduced, and the reduction of film thickness with ME is caused by the bearing orbit growth as well as the bearing clearance

67

shrinkage due to the rotor expansion. Especially, the minimum film thickness ratio drops below $10\%C_b$ over 11.8 krpm where the simulation is halted and continues to the next speed to avoid possible numerical errors. The predicted instability onset speed at 11.8 krpm is close to the speed observed by de Jongh [12]. In Fig. 3-7, one may observe the existence of the recovery speed, above which the vibration and journal ΔT will drop to an acceptable level, and the recovery from the ME-instability is also reported in the test rig [12].

3.2.4　Comparison of Various Transient Analysis Methods

Various transient methods can be selected for the ME analysis, including the fully nonlinear method, the linear method and the SOWM (see Section 3.1.2). The latter two methods simplify the ME prediction in order to improve the computational efficiency. Based on the aforementioned rotor model, three different methods are applied for the transient analysis and the results of the NDE are listed below in Fig. 3-8. The transient speed curve is also illustrated in Fig. 3-8(a) where the speed grows linearly from 9 krpm to 11.8 krpm within 1 min and then stays at 11.8 krpm for 40s before it decreases to 9 krpm.

Fig. 3-8 shows that the vibration amplitude and the journal ΔT based on the linear transient method are the highest among all three methods, illustrating that the linear method may significantly overpredict the ME problem. As mentioned in Section 3.1.2, the linear method linearizes the bearing force with dynamic coefficients, and the accuracy will deteriorate when the bearing orbit grows larger and the journal is displaced significantly away from its equilibrium position. Meanwhile, the results of the SOWM are quite close

to the fully nonlinear transient method, demonstrating that for this specific case, the dual-bearing vibration problems can be decoupled and regressed towards a single overhung problem. The close approximation of the SOWM is due to the unique 2nd bending mode shape of the original rotor: the mode shape exhibits very low vibration at the DE, making it difficult for the DE bearing to develop sufficient orbits to cause enough journal ΔT to bend the rotor, and therefore it is reasonable to neglect the ME in the DE bearing and simply model it with speed-dependent dynamic coefficients, which has little effect on the rotor dynamics as well as on the ME at the NDE.
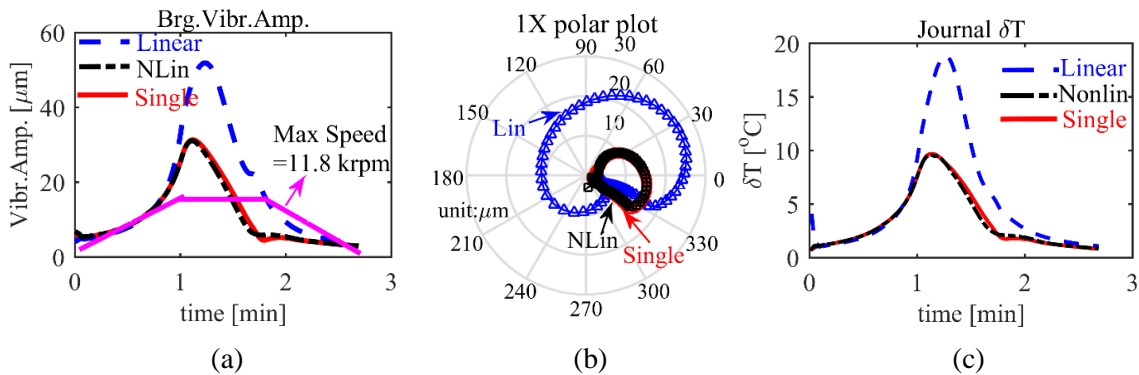
Fig. 3-8 Morton Effect analysis on the NDE with various transient methods.(a) PK-PK vibration amplitude at the bearing node (b) 1X polar plot of the bearing (c) PK-PK ΔT across the journal circumference.

In the following analysis, the DE overhung wheel is designed to be heavier than that of the original rotor to enhance the ME on the DE. Fig. 3-9 illustrates the comparison of the SOWM and the fully nonlinear method. The rotor speed starts from 9 krpm and increases linearly to 11.9 krpm within 60s and then stays constant.
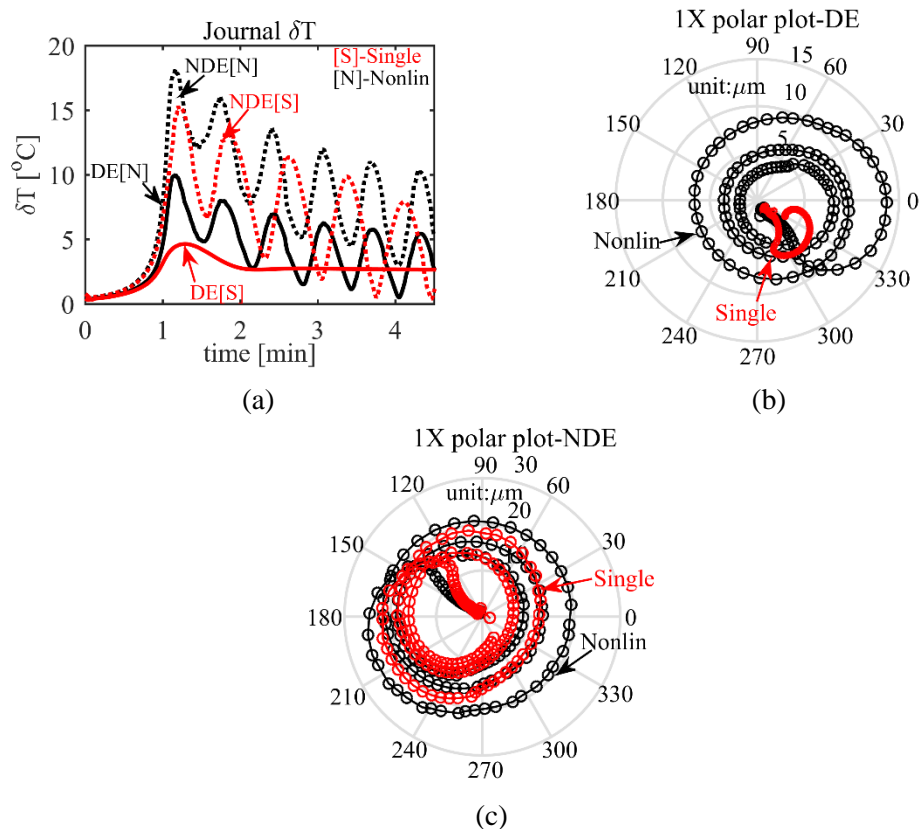
Fig. 3-9 Comparison of fully nonlinear transient method and single-overhung-wise method. (a) PK-PK Journal ΔT on the NDE and DE. (b) 1X polar plot of the DE bearing (c) 1X polar plot of the NDE bearing.

Fig. 3-9(a) shows that for both bearings the SOWM underpredicts the journal ΔT, and this is especially evident for the DE bearing: the peak journal ΔT is over 50% smaller than the fully nonlinear method. The 1X polar plot in above Fig. 3-9(b) and Fig. 3-9(c) confirms the underprediction of the ME by SOWM: for both bearings, the SOWM gives smaller spirals. The SOWM performs the ME analysis of only one bearing each time, thus failing to predict the comprehensive rotor thermal bending. And moreover, the ME in both bearings cannot be simply decoupled as assumed in the SOWM, for instance, in this case

the thermal imbalance in the NDE rotor can also amplify the rotor vibration at the DE-bearing node and raise the journal ΔT, thus intensifying the ME in the DE bearing.

The computational cost of the software can be an important indicator for practical application. The current algorithms are implemented with the mixing programing of MATLAB and C++ to accelerate the numerical integration. The time consumption for the transient analysis in Fig. 3-8 and the steady analysis (for single speed, note that there are 15 speeds simulated in total) in Fig. 3-7 are listed in Table 3-2. And the time cost is based on the authors' PC with 16 GB memory and i7 quad-core CPU. The software uses "ODE23" solver with relative tolerance of 1E-2 and absolute tolerance of 1E-3.

Table 3-2 Time cost of three different methods

	Linear	Single-overhung-wise	Fully nonlinear
Transient case	30 mins	2 hours 30 mins	5 hours 20 mins
Steady case per speed	8 mins	25 mins	26 mins

3.2.5 Influence of Pad and Pivot Flexibility

In this section, three different pad models are compared including (1) flexible pad + flexible pivot, (2) rigid pad + flexible pivot, and (3) rigid pad + rigid pivot. For case 1, each pad is meshed by $15 \times 7 \times 5$ layers in circumferential, axial, radial direction, and both the pad and pivot flexibility is considered; for case 2, each pad has 2 DOFs, i.e. the pad tilting and pivot translation, and the pad is assumed to be rigid in the dynamic model; for case 3, each pad has only 1 DOF, i.e. pad tilting. Theoretically, case 1 is the most precise method among all three since the flexible pad model considers both the rigid body

modes, corresponding to the tilting and translation motion in the rigid pad model, and the flexible modes. The simulation results with the fully nonlinear transient method (see Section 3.1.2) are listed in Fig. 3-10.

(a)

(b)

(c)
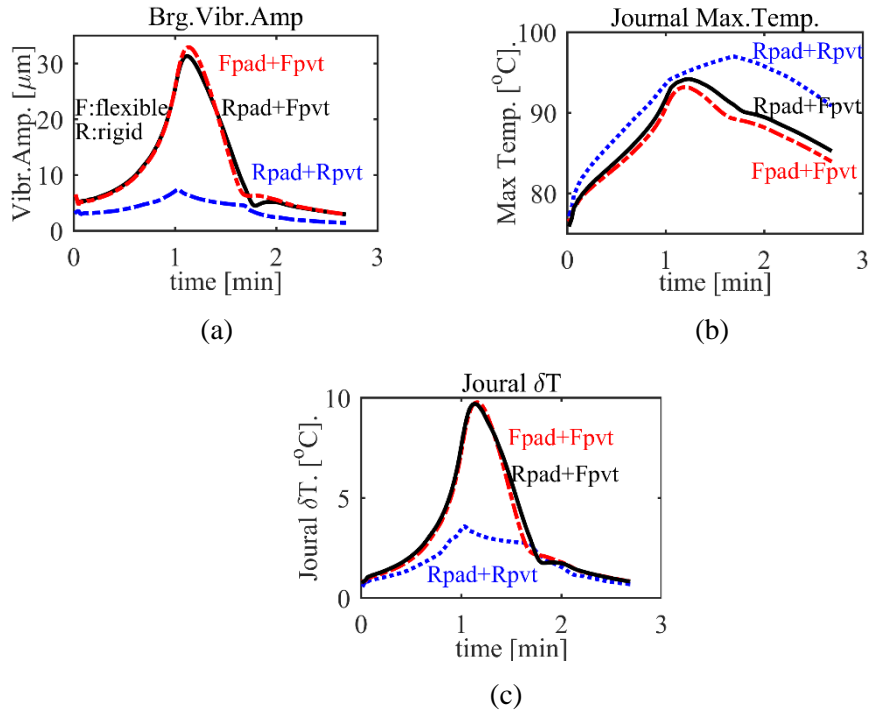
Fig. 3-10 Morton Effect on the NDE based on different pad models. (a) Bearing vibration amplitude (b) Maximum journal temperature (c) Journal circumferential PK-PK ΔT.

Note that the results of case 2 are quite close to case 1, indicating that the pad flexibility barely affect the rotordynamics for this specific bearing, and the rigid pad can be a good approximation. Nevertheless, neglecting the pivot flexibility can significantly underpredict the ME with much lower vibration amplitude and journal ΔT. This is because the bearing clearance is more sensitive to the pivot deformation than the pad flexibility, and the rigid pivot will always underpredict the bearing clearance and stiffen the rotor

system model, pushing the critical speeds away from the operating speed for the current rotor model. Note that the approximation with the rigid pad model cannot be simply applied to all bearings considering that very thin pads can be prone to elastic deformation compared with thick pads, and in the thin pad case, the pad flexibility cannot be ignored.

4 MORTON EFFECT PREDICTION ALGORITHM

(II) – BOWED ROTOR METHOD[*]

The thermal expansion of the shaft simultaneously affects the dynamics of the rotor-bearing system in two ways. One effect is that the increase of journal diameter will reduce the bearing clearance, thereby changing the hydrodynamic force acting on the journal. The other effect is that the asymmetric temperature distribution caused by the ME will bend the shaft causing thermal bow, which could be the dominating factor in the thermally induced, synchronous instability problem.

4.1   Introduction to the Bowed Rotor Method

4.1.1   Element Type Selection

The local thermally induced deformations at the journal are best determined utilizing high fidelity 3D solid (brick) elements. These local deformations in the journal region transmit bending forces and moments to the entire shaft system. The portions of the shaft excluding the journal region are best modeled with 3D Euler-Bernoulli/Timoshenko beam elements for enhanced computational efficiency and good high accuracy. Prior research [13, 29, 40] indicates that the thermal region described above might typically encompass a length approximately several times the journal length. The combined beam – solids approach is referred to below as the hybrid finite element model

---

[*] Reprinted with permission from "Rotordynamic Morton Effect Simulation With Transient, Thermal Shaft Bow" by Tong, X., Palazzolo, A., and Suh, J., 2016. Journal of Tribology, 138(3): 031705. Copyright 2016 by ASME.

(HFEM) and represents a practical balance between computational efficiency and predictive accuracy.
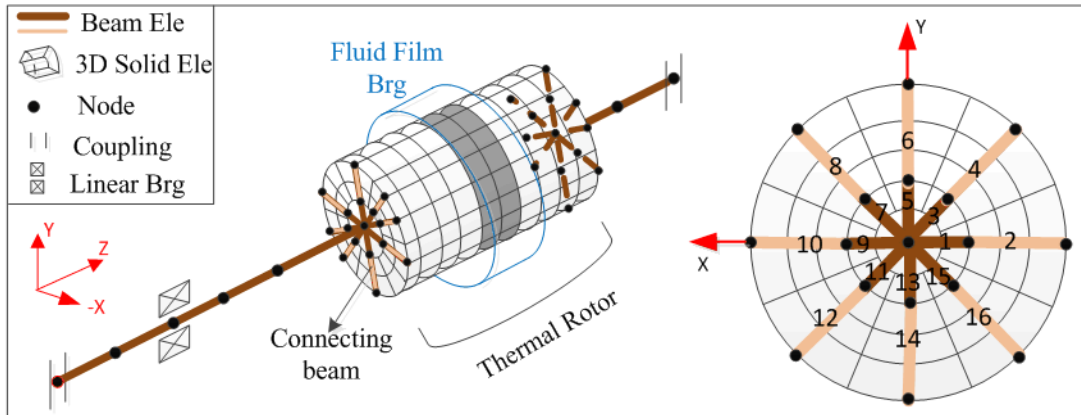
Fig. 4-1 Diagram illustrating the hybrid finite element model.

As illustrated in Fig. 4-1, the rotor section close to the fluid film bearing, i.e., the thermal rotor, is modeled with 3D solid elements. Meanwhile, other rotor parts with smaller bearing induced temperature change are modeled with beam elements. Note that fictitious connecting beams are included at the solid and beam element interfaces to transmit forces and bending moments caused by dynamic motion and by the temperature difference (ΔT) distribution in the journal region. The stiffness property of the fictitious beam interface elements is kept high so as not to introduce significant compliance at the interface, but not too high which would penalize numerical integration accuracy.

4.1.2 Thermal Deflection Calculation

The temperature distribution of the thermal rotor is calculated by solving the heat conduction problem assuming that the temperature and heat flux are continuous at the

boundary of the rotor and lubricant. The convective boundary conditions are imposed on the other rotor surfaces exposed to the ambient air. The calculation of rotor temperature is a complex task and is fully explained in Section 2.2 and Ref. [40]. The thermal force vector $F_{\Delta T}$ resulting from the imposed temperature distribution in the 3D solid element will deform the rotor. Fig. 4-2 shows the x, y and z components of the thermal force vectors at each node of a typical solid element. The beam elements represent the shaft external to the portion of the shaft heated by the bearing ME. The entire rotor is modeled with the HFEM approach, as shown in Fig. 4-3. The static elastic deformation is calculated with the equivalent external load vector $F_{\Delta T}$, where the detailed expression of $F_{\Delta T}$ and the stiffness matrix for both the solid elements and beam elements are discussed in the appendix. Fig. 4-3 shows one linear bearing, the Morton journal region (solid elements) and two couplings.
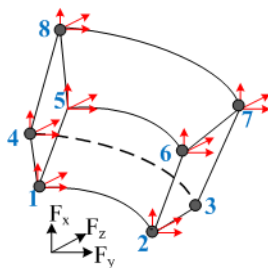
Fig. 4-2 Thermal load for solid elements.
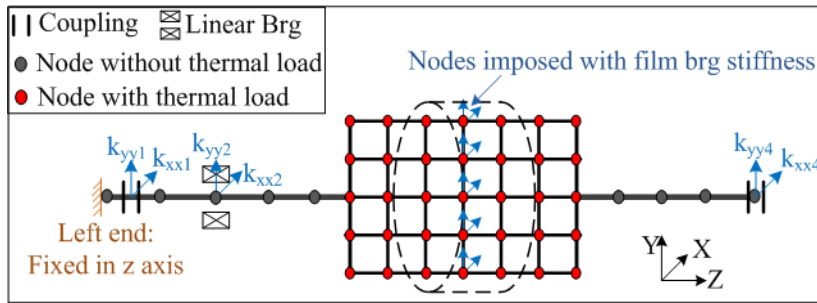
Fig. 4-3 Static thermal deformation model.

In practice, the rotor will be fixed in the axial direction by the thrust bearing. For simplicity, the rotor DE (drive end) is fixed and the NDE (non-drive end) can expand freely in the axial direction, as shown in Fig. 4-3. The couplings and the linear bearings will provide additional constraints, and their stiffness should be added to the rotor stiffness matrix for calculating the thermal expansions. The stiffness of the film bearing is speed dependent and should be pre-calculated, and then the film bearing stiffness is uniformly imposed on the nodes which are located on the middle plane of the film bearing, i.e. *K/N*, where *K* is the film bearing stiffness and *N* is the node number on the middle plane.

4.1.3 Dynamic Model

As shown in Fig. 4-4, mass imbalance, residual bow and disk skew (tilt) are present in all shaft assemblies due to manufacturing tolerances, heat treatment, press fitting practice, etc. Meanwhile, the disk may be tilted by misalignment with the rotor. Residual bow and disk skew both create synchronous (at spin rate frequency) dynamic excitations due to the rotation of the shaft, and can slowly change due to the thermal Morton phenomena. The present paper utilizes a bowed rotor ME model since it reflects the actual

behavior of the shaft as opposed to prior representations utilizing an equivalent thermally induced imbalance approach. The justification of the new method lies in the distinct dynamic response of a bowed rotor as contrasted with an imbalanced rotor. The intuitive explanation of this distinction is closely related to both the simplification of the unbalance method itself and the sensitivity of the ME. Specifically, the unbalance method neglects both the damping terms and the bending moments from transverse angles of the bowed rotor. Moreover, considering that the ME is very sensitive to the rotordynamic excitation, slight over/under evaluation of the excitation by the unbalance method can result in significant difference in the ME predictions, illustrated in section 4.2.2.
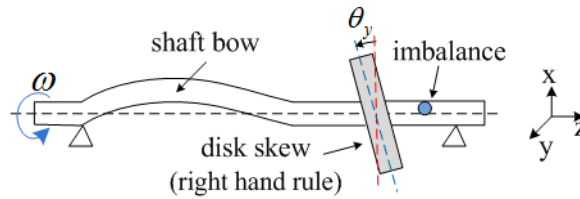
Fig. 4-4 Force sources for the synchronous vibration.

The directions of the disk skew angles as sensed in the stationary frame obeys the right hand rule and is expressed by $\theta_x = -\theta_{skew}\sin(\omega t + \varphi_0)$ and $\theta_y = \theta_{skew}\cos(\omega t + \varphi_0)$. The initial phase of the skewed angle is $\varphi_0 = 0$, and thus at the instant 't=0', $\theta_x = 0$, $\theta_y = \theta_{skew}$.

Combination of Thermal Bow and Permanent Bow

The Euler-Bernoulli beam rotor model possesses θ_x, θ_y, x, y degrees of freedom in the two lateral directions, and excludes axial degrees of freedom θ_z, z. Both the thermal

bow and the permanent bow are relatively small, and so the rotor bow vector is assumed

to be a linear combination of both vectors, as shown in Eq. 4-1.

$$\begin{bmatrix} x_{n\_bow} \\ y_{n\_bow} \end{bmatrix} = A_{n\_tbow} \begin{bmatrix} cos(\omega t + \varphi_{n\_tbow}) \\ sin(\omega t + \varphi_{n\_tbow}) \end{bmatrix} + A_{n\_pbow} \begin{bmatrix} cos(\omega t + \varphi_{n\_pbow}) \\ sin(\omega t + \varphi_{n\_pbow}) \end{bmatrix} \quad Eq.\ 4\text{-}1(a)$$

$$\begin{bmatrix} \theta_{xn\_bow} \\ \theta_{yn\_bow} \end{bmatrix} = \Phi_{n\_tbow} \begin{bmatrix} cos(\omega t + \psi_{n\_tbow}) \\ sin(\omega t + \psi_{n\_tbow}) \end{bmatrix} + \Phi_{n\_pbow} \begin{bmatrix} cos(\omega t + \psi_{n\_pbow}) \\ sin(\omega t + \psi_{n\_pbow}) \end{bmatrix} Eq.4\text{-}1(b)$$

Note that, the amplitude and initial phase of the permanent bow, i.e., $A_{\text{n\_pbow}}$, $\varphi_{\text{n\_pbow}}$, $\Phi_{\text{n\_pbow}}$, $\psi_{\text{n\_pbow}}$ are constant, but the amplitude and phase of the thermal bow will always change with the rotor temperature distribution and are transient in the time domain. However, considering that the thermal response is quite slow, temperature can be regarded as quasi-static and will be updated in a time staggered manner in the total system transient response. Thus, between each update time, the rotor temperature distribution is assumed to be constant, resulting in piecewise constant, temporal representations of $A_{\text{n\_tbow}}$, $\varphi_{\text{n\_tbow}}$, $\Phi_{\text{n\_tbow}}$, $\psi_{\text{n\_tbow}}$.

Rotor Bow and Disk Skew Modeling

The governing equation for the system dynamics has the standard form

$$[M_{rot}][\ddot{U}] + [C_{rot}][\dot{U}] + [K_{rot}][U - U_{bow} - U_{skew}]$$
$$= [F] = [F_{\text{mew2}} + F_{\text{gyro}} + F_{\text{brg}} + F_{\text{ext}}] \qquad Eq.\ 4\text{-}2$$

The damping and stiffness of the linear bearing, seal and coupling models are incorporated in $[C_{\text{rot}}]$ and $[K_{\text{rot}}]$. The Morton Effect fluid film bearing force is F_{brg} and

U_{bow} is the resultant of U_{pbow} and U_{tbow}. Both U_{bow} and U_{skew} have non-zero components at all nodes where the bow and skewed disks occur.

Substituting the relative displacement vector

$$[U_r] = [U - U_{bow} - U_{skew}] \qquad\qquad Eq.\ 4\text{-}3$$

and rearranging Eq. 4-2 yields

$$[M_{rot}][\ddot{U}_r] + [C_{rot}][\dot{U}_r] + [K_{rot}][U_r] = [F_{all}]$$
$$= [F] - [M_{rot}][\ddot{U}_{bow} + \ddot{U}_{skew}] - [C_{rot}][\dot{U}_{bow} + \dot{U}_{skew}] \qquad Eq.\ 4\text{-}4$$

Note that even without external forces, the system will still vibrate and may be susceptible to the Morton thermal instability effect due to the rotor bow and disk skew on the right of Eq. 4-4. The nodal force generated by the skewed disks is expressed in Eq. 4-5 for node i (assuming that the nodal components of $[C_{\text{rot}}]$ are all zero at the skewed disks for simplicity).

$$\left[F_{ix}, F_{iy}, M_{ix}, M_{iy}\right]^T_{skew} = -\left[M_{i_{rot}}\right]\left[\ddot{U}_{i_{skew}}\right] + \left[F_{i_{gyro}}\right]$$
$$= [0, 0, -I_{Ti}\ddot{\theta}_{xi} - \omega I_{pi}\dot{\theta}_{yi}, -I_{Ti}\ddot{\theta}_{yi} + \omega I_{pi}\dot{\theta}_{xi}]^T \qquad Eq.\ 4\text{-}5$$

where, θ_{xi} and θ_{yi} are the nodal skewed angles observed in the stationary frame, and I_{Ti} and I_{pi} are the nodal transverse and polar mass moment of inertial.

The additional nodal force vector in Eq. 4-4 generated by the thermal bow for node i appears as

$$[F_{ix}, F_{iy}, M_{ix}, M_{iy}]_{tbow}^T = -[M_{i_{rot}}][\ddot{U}_{i_{tbow}}] - [C_{i_{rot}}][\dot{U}_{i_{rot}}]$$

<div align="right">*Eq. 4-6*</div>

Assuming that the thermal bow has a constant magnitude before it is updated in the rotor deflection solver, the first term on the right hand side of Eq. 4-6 can be replaced by Eq. 4-7, where m_i is the lumped mass at node i, $\breve{x}_i$, $\breve{y}_i$ are the nodal thermal deflection, $\breve{\theta}_{xi}$, $\breve{\theta}_{yi}$ are the nodal bending angle of the thermal bow. Note that the thermal bow is observed in the stationary frame with directions obeying the right hand rule.

$$-[M_{i_{rot}}][\ddot{U}_{i_{tbow}}] = \omega^2 \cdot [m_i \breve{x}_i, m_i \breve{y}_i, I_{Ti} \breve{\theta}_{xi}, I_{Ti} \breve{\theta}_{yi}]^T$$

<div align="right">*Eq. 4-7*</div>

This is quite different from the equivalent thermal induced mass imbalance model [12, 31, 38]

$$[F_{ix}, F_{iy}, M_{ix}, M_{iy}]_{tbow}^T = \omega^2 \cdot [m_i \breve{x}_i, m_i \breve{y}_i, 0, 0]^T$$

<div align="right">*Eq. 4-8*</div>

which typically employs a single imbalance at the overhung disk or attaches distributed imbalances [40] on the bowed rotor to model the thermal bow excitation. However, both versions of the imbalance method neglect the moments induced by the transverse angles in thermal bow and damping related effects in Eq. 4-6.

At first glance it may appear that the synchronous, harmonic steady state response can be derived with Eq. 4-9.

$$[\hat{U}_r] = (-\omega^2[M_{rot}] + i\omega[C_{rot}] + [K_{rot}])^{-1}((\omega^2[M_{rot}] - i\omega[C_{rot}]) \times [\hat{U}_{bow} +$$

$$\hat{U}_{skew}] + [\hat{F}])$$

<div align="right">*Eq. 4-9*</div>

However, $[\hat{U}_{bow}]$ is affected by the journal region temperature distribution, which varies nonlinearly with the whirl orbit, and affects the temperature distribution in the rotor and bearing by providing an additional excitation, and by changing the film thickness. This renders the solution Eq. 4-9 untenable, and so a nonlinear transient numerical integration solution is recommended to solve the thermal-hydrodynamic problem.

Modal Reduction

The biorthogonality of the left and right eigenvectors is employed here to condense Eq. 4-4 by utilizing modal coordinates. This significantly increases the computational efficiency of numerically integrating Eq. 4-4 to obtain $U_r(t)$. Rewrite Eq. 4-4 in first order (state) form as

$$[\dot{Z}] = [D][Z] + [F_z] \qquad \qquad \text{Eq. 4-10}$$

where $Z = [\dot{U}_r, U_r]^{\mathrm{T}}$, $[D] = \begin{bmatrix} -M_{rot}^{-1}C_{rot} & -M_{rot}^{-1}K_{rot} \\ 1 & 0 \end{bmatrix}$, $[F_z] = [{M_{rot}^{-1}F_{all}} \atop 0]$, and F_{all} is defined in Eq. 4-4.

The right eigenvector Φ_{Ri} and the left eigenvector Φ_{Li} are defined and normalized as indicated in Eq. 4-11.

$$\begin{cases} \lambda_i \Phi_{Ri} = [D]\Phi_{Ri} \\ \lambda_i \Phi_{Li} = [D]^T \Phi_{Li} \end{cases} and \; \Phi_{Lm}^T[D]\Phi_{Rn} = \begin{cases} \lambda_n, if \; m = n \\ 0, if \; m \neq n \end{cases} \qquad \text{Eq. 4-11}$$

Where λ_i is the ith eigenvalue. The biorthogonality relation in Eq. 4-11 can be used to diagonalize $[D]$. Substitute $[Z] = [\Phi_R]Y$ and pre-multiply Eq. 4-10 by $[\Phi_L]^{\mathrm{T}}$ to obtain the condensed Eq. 4-12.

$$[\ddot{Y}]_{k \times 1} = [\lambda_n]_{k \times k} Y + [\Phi_L]^T F_z \qquad\qquad Eq.\ 4\text{-}12$$

where k is the number of modes, $[\lambda_n]$ is a diagonal matrix with λ_1 to λ_k in the diagonal line, $[\Phi_R]$ and $[\Phi_L]$ are defined by $[\Phi_R] = [\Phi_{R1}, \Phi_{R2}, \dots, \Phi_{Rk}]$, and $[\Phi_L] = [\Phi_{L1}, \Phi_{L2}, \dots, \Phi_{Lk}]$

4.1.4 Algorithm for the Nonlinear Transient Morton Effect Analysis

(a) *Temperature solution*. Asymmetric journal temperature is the root cause of the ME. The temperature distribution in the journal region, lubricant and fluid film bearing must be accurately calculated to effectively predict the ME. The temperature model should include a coupled thermal transient solution of the bearing, film and shaft conduction/convection problems. This must be done in a computationally practical manner accounting for the very short time constant of synchronous (at shaft spin frequency) thermal excitation and vibration, and the very long time constant of bearing and shaft heating. Accurate prediction of the fluid film temperature must include the convective term in the energy equation which displaces the hot spot away from the high spot. The convective term typically requires use of upwinding finite elements for numerically stable solutions of the energy equation. Time staggered solution approaches and usage of thermal and structural modes for coordinate condensation can be incorporated to reduce the coupled rotordynamics/bearing transient computation time to acceptable lengths. These topics are discussed in fine detail in the author's previous publications [29, 39, 40].

(b) *Thermal bow solution.* The structural HFEM in Fig. 4-1 was formulated based on numerical experiments that showed that the ME temperature distribution violates the

linear assumptions that are typically made in simulating the ME. Specifically the temperature distribution may vary quite nonlinearly through the journal thickness, and the ME asymmetric temperature distribution extends well beyond the length of the journal. In addition, the cross section of the journal deforms into a slight oval, effecting the film thickness distribution, pressure, heating and temperatures. For these reasons a 3D, structural solid element model is incorporated in the journal region. This is adjoined to beam element representations of the remaining portions of the shaft to maintain computational efficiency and modeling accuracy. The HFEM then provides an accurate and computationally practical approach for predicting the transient shaft bow $U_{tbow}(t)$ that is needed for solving Eq. 4-4.

(c) ***Transient rotordynamic system solution***. This step is the transient numerical integration of Eq. 4-4 with synchronous excitation sources including residual (permanent) disk skew, mass imbalance and permanent shaft bow, and time varying, thermally induced shaft bow.

The instantaneous bearing forces F_{brg} are obtained by solving Reynolds equation with finite elements during the transient solution. Thermal bows U_{tbow} are determined as described above during the transient solution and are added to the permanent (initial) bow to obtain the total bow U_{bow}. The dimensions of the rotordynamics system model Eq. 4-4 are greatly reduced by employing subspace condensation with thermal and structural modes as basis vectors for spanning the subspace.

(d) ***Evaluate ME system stability.*** The ME is often referred to as a synchronous 'instability' phenomena involving the slowly increasing component of shaft vibration at

the frequency of rotor spin (1X). Note that considering the ME is fully nonlinear, the 'instability' herein is different from that in the linear problem, where eigenvalues are utilized. Two practical aspects of the ME-induced instability are (a) the machinery would be tripped or lowered in speed if vibrations exceeded some preset level often determined by ISO or API standards, and (b) unlike linear stability models the vibration would eventually become bounded by a time invariant or oscillatory limit cycle. Thus, the ME instability phenomena has the practical definition as synchronous vibrations that grow slowly with time eventually exceeding vibration trip levels within 1 – 5 minutes, while the speed and machinery load conditions remain constant. While not being exclusive of all other phenomena such as rubs, this definition encapsulates reported machinery experience quite well. For purposes of simulation we slightly broaden the symptoms indicating ME as indicated below.

Minimum film thickness. If the vibration induced minimum film thickness $h_{min}(t) < h_0$, direct rubbing may occur between the bearing and the journal, and the system is said to have a ME instability. This is conditional based on the same system having minimum film thickness well within acceptable levels if the ME effect is not included in the simulation.

Vibration amplitude. If the vibration amplitude at the bearing node exceeds the threshold, e.g. defined by API standard [48], the system is ME unstable. This is conditional based on the same system having vibration amplitudes well within acceptable levels if the ME effect is not included in the simulation.

Maximum lubricant temperature. If the peak temperature in the lubricant film exceeds an unallowable level $T_{max} > T_0$, the system is ME unstable. This is conditional based on the same system having a peak lubricant temperature well within acceptable levels if the ME effect is not included in the simulation.

(e) ***System transient ME simulation.*** The temperature change in the shaft and bearing occurs quite slowly relative to the shaft vibration deflection changes (vibration), yet both are dependent on each other in the ME. A practical consequence of this is that although the end time of the numerical integration-based simulation is relatively long, the numerical integration time step must be very short. This is a bad combination for simulations. This problem was addressed in the author's prior work [29, 39, 40] by employing a staggered scheme wherein ① both the thermal and dynamic problem are integrated simultaneously over a short period to update the film temperature and rotor vibration, followed by ② a longer period where the temperature problem is integrated to update the bearing and journal region temperature distributions and the thermal bow. The integration time for the thermal only update is longer than its counterpart for the combined thermal- structural system. This staggered integration scheme is shown in Fig. 4-5. For the examples in this paper, $t_{span2} = 200 t_{span1}$, and the ratio 200 is selected by consideration of time constants and from experience. Depending on the rotor-bearing configuration, slightly raising this ratio is helpful to improve the simulation speed, however, excessive value should be avoided due to the deterioration of accuracy.
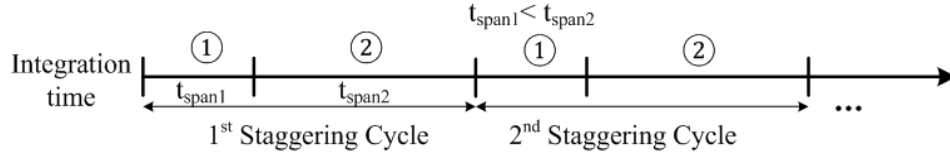
Fig. 4-5 Staggered integration scheme.
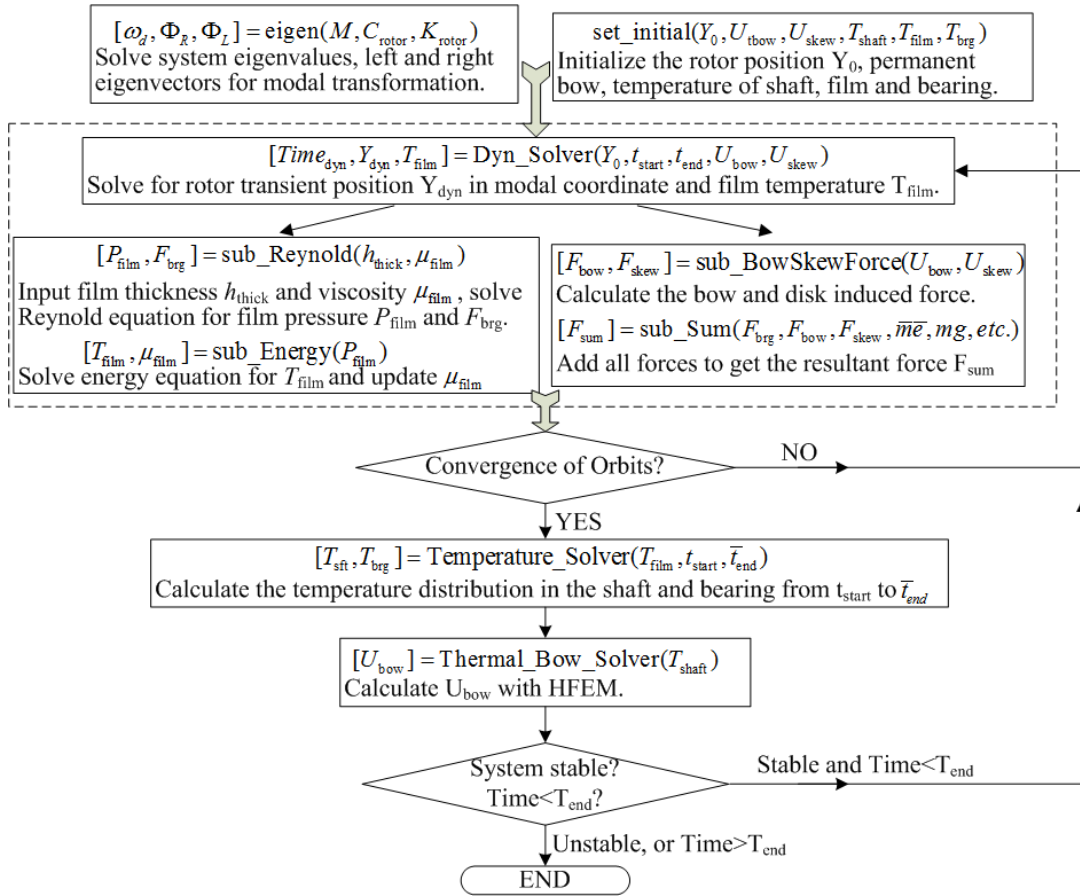
Fig. 4-6 Flow diagram for Morton Effect transient simulation.

This process is repeated throughout the entire ME simulation until the system stabilizes or exhibits a ME instability and is terminated. The ME solution process is illustrated in Fig. 4-6.

4.2   Verification with Case Studies

Simulations are based on the single overhung rotor-bearing model tested by de Jongh and van der Hoeven [16] with input parameters from [29, 64]. This system began to exhibit ME instability just above 8,000 rpm and within two minutes the vibration trip level was reached.

The simulation model employed in the present study is the same as [16] but includes permanent bow and disk skew effects for parametric studies, and other than that, both the permanent bow and disk skew are set to be zero for consistency with the tested case [16]. The mass imbalance, without specification, is located at node 18 with a magnitude of $2.7 \times 10^{-4} kg \cdot m$ and phase angle of 0 degree. As shown in Fig. 4-7, the linear bearing model and nonlinear (Morton Effect) tilting pad bearing model are located at nodes 4 and 12 respectively.
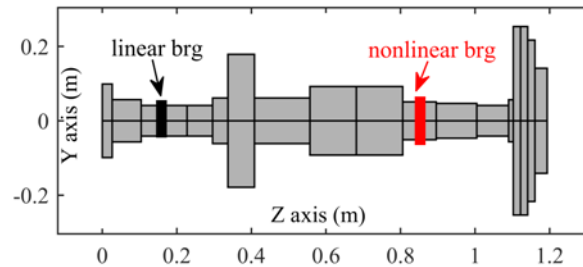
Fig. 4-7 Rotor-Bearing configuration.

The single overhung mass is located at the non-drive end (NDE), which is the right side of the rotor. All rotor surfaces have convective boundary conditions with the ambient temperature of 30 ℃ and convection coefficient of 50 W/(m^{2}K). The lubricant thermo-

viscosity relationship is modeled with $\mu = \mu_{ref} e^{-\alpha(T-T_{ref})}$, where α is the viscosity coefficient, μ_{ref} and T_{ref} are the reference viscosity and temperature. Important parameters can be found in Table 4-1.

Table 4-1 Simulation parameter

Lubricant parameters		Bearing parameters	
Viscosity at 50 ℃ [Ns/m²]	0.0203	Pad type	Load on Pad
Viscosity coefficients [1/℃]	0.031	No. pads	5
Supply temperature [℃]	50	Radius of shaft [m]	0.0508
Inlet pressure [Pa]	1.32×10^5	Bearing clearance [m]	7.49×10^{-5}
Reference temperature [℃]	50	Preload	0.5
Shaft Parameters		Bearing length[m]	0.0508
Heat capacity [J/kg ℃]	453.6	Thermal expansion coeff. [1/℃]	1.3×10^{-5}
Heat conductivity [W/mK]	50	Reference Temperature [℃]	25
Thermal expansion coeff.[1/℃]	1.22×10^{-5}	**Linear Bearing**	
Reference temperature [℃]	25	K_{xx}, K_{yy} [N/m]	1.7×10^8
Thermal rotor length [m]	0.3508	C_{xx}, C_{yy} [Ns/m]	1.0×10^5

4.2.1 Simulation Results vs. Rotor Speed

The nonlinear transient analysis starts from the lowest speed and once it's done, the solver will switch to the next higher speed, and so on. If the system is stable, all state variables, such as the dynamic and temperature data will be inherited as the initial condition of the next speed. Otherwise, the state variables of the closest stable speed will be used as initial conditions. This method assumes that the instability of the previous speed

won't affect the next speed, thus will give more conservative results. The results from 5000 to 12000 RPM are plotted in Fig. 4-8. This plot shows the peak values of vibration amplitude and journal temperature difference, and the minimum film thickness ratio captured over the entire transient simulation time at any given speed. The computational time required for each speed depends on how fast the system converges/diverges, and also varies with tolerances in the differential equation solver. For the present case, the simulation time per speed ranges from 1/4~1 hour using the 'ode23' MATLAB solver and relative tolerance of 1E-3 and absolute tolerance of 1E-4.
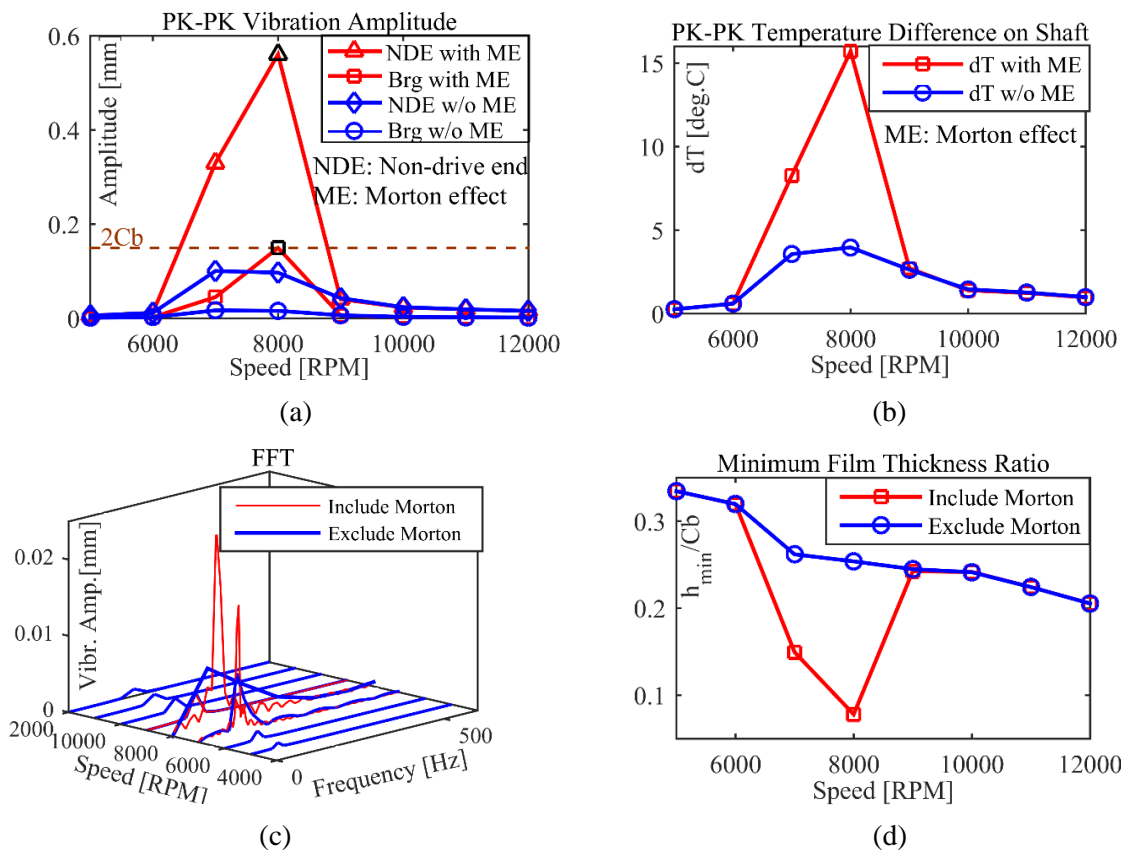
Fig. 4-8 Key response variables vs. speed. (a) Peak-Peak vibration at the rotor non-drive end(NDE) overhung disk and at the tilting pad bearing (b) Peak-Peak temperature difference in the journal (c) FFT of the tilting pad bearing vibration (d) Minimum film thickness ratio.

Fig. 4-8 illustrates the vibration and temperature difference at different speeds. Results with red lines consider the thermal bow in the dynamic model, while the blue lines neglect the thermal bow. Results with the ME show much larger vibration amplitude at the overhung disc and the tilting pad bearing, and a larger peak-peak temperature difference (ΔT) in the shaft. The system experiences ME synchronous instability near 8000 RPM with $h_{min} < h_0$, which is 10% of the bearing clearance in this simulation. This instability phenomenon was observed experimentally by de Jongh [16]. The speed range with violent vibration corresponds to that with large peak-peak ΔT in the journal, which results from the ME. The high ΔT across the journal circumference causes a thermal bow which displaces the large overhung disk mass away from the equilibrium line, generating significant inertial forces and resulting vibrations. Fig. 4-9 shows the thermal bow components in X-Z and Y-Z planes at various speeds along the rotor length, and the subplots inside the circle illustrate the bow profiles at the NDE bearing with 10-fold magnification. For the speeds with converging ME, these bows are the final steady states. Otherwise, no steady states are available and the maximum transient thermal bow is plotted. The length of the thermal rotor (shown in Fig. 4-1), is seven times the bearing length in the simulation. Note that the thermal bow amplitude at both bearings is almost zero because additional bearing stiffness is added to the rotor to apply a transverse constraint for determining the bow. The bow amplitude at the rotor NDE overhung disk increases and then decreases with speed, while simultaneously the phase angle keeps changing.
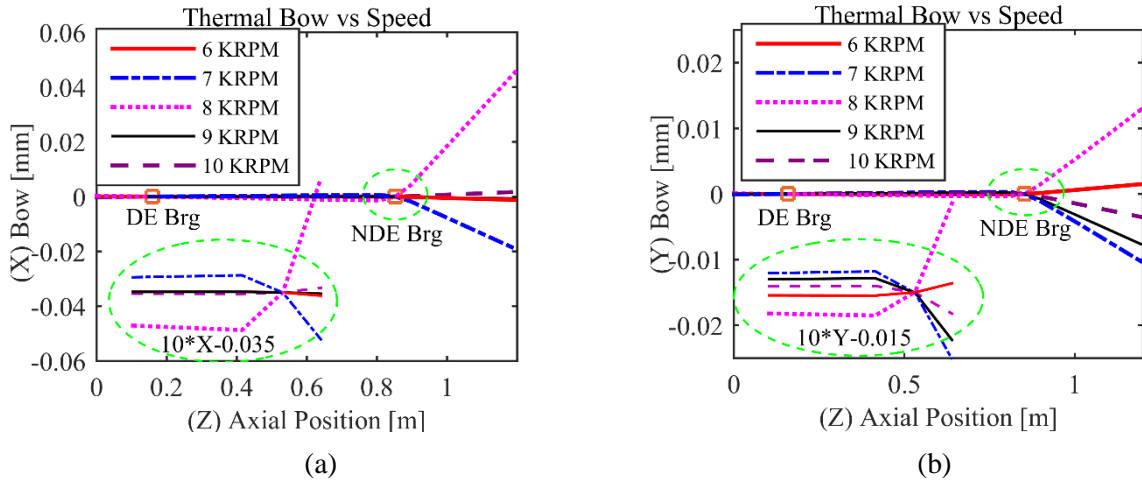
Fig. 4-9 Thermal bow at various speeds. (a) X-Z plane (b) Y-Z plane.

4.2.2 Compare the Thermal Bow Method and Thermal Imbalance Method

The physics of the ME consists of an asymmetric heat source acting on the journal region of the shaft and a resulting rotating bow caused by the shaft thermal bending moments at the heat source. The thermal bow is defined and described in a rotating frame of reference fixed to the shaft. The bow is a deflection distribution involving translatory and rotational (tilt) coordinates along the length of the shaft, with maximum bow deflection located at the end of the shaft adjacent to the ME bearing. The maximum deflection at the end of the shaft may be coincident with an overhung wheel, so the wheel could execute a large vibration simply due to the bow. A common assumption is that the effect of the bow may be included by neglecting the bow and simply attaching a lumped imbalance at the disk location, with a magnitude equal to the mass of the wheel multiplied by the bow displacement at the wheel [31, 38]. Another improved version of the imbalance approach replaces the lumped model with distributed imbalances attached to all bowed-

92

rotor nodes [40]. This imbalance approach may provide a good approximation however a highly refined model, including actual bowed rotor dynamics, may be required to accurately predict the ME. This is clearly illustrated in Fig. 4-10 where vibration response is shown at 8500 rpm, with an "equivalent" distributed imbalance model and with an actual bowed rotor model. The imbalance method shows that direct rubbing of the rotor and bearing occurs at around t= 5.5 min with excessively large vibration amplitude at the rotor NDE as well as the bearing location, and the temperature difference ΔT across the journal is well above 20 deg. C. Both methods show similar results until t= 3 min, when the imbalance method shows a strong synchronous instability with a rapid increase of vibration amplitude and ΔT, while the bow method shows a slight oscillation with no occurrence of rubbing. The bow method provides an improved prediction of ME considering that the experiment in [16] shows similar oscillation amplitudes without synchronous instability (rubbing between pads and shaft), at 8500 rpm. Note that all simulation results from Fig. 4-8~Fig. 4-10 are based on the initial mass imbalance of $2.7 \times 10^{-4} kg \cdot m$ and zero permanent bow and disk skew inputs.
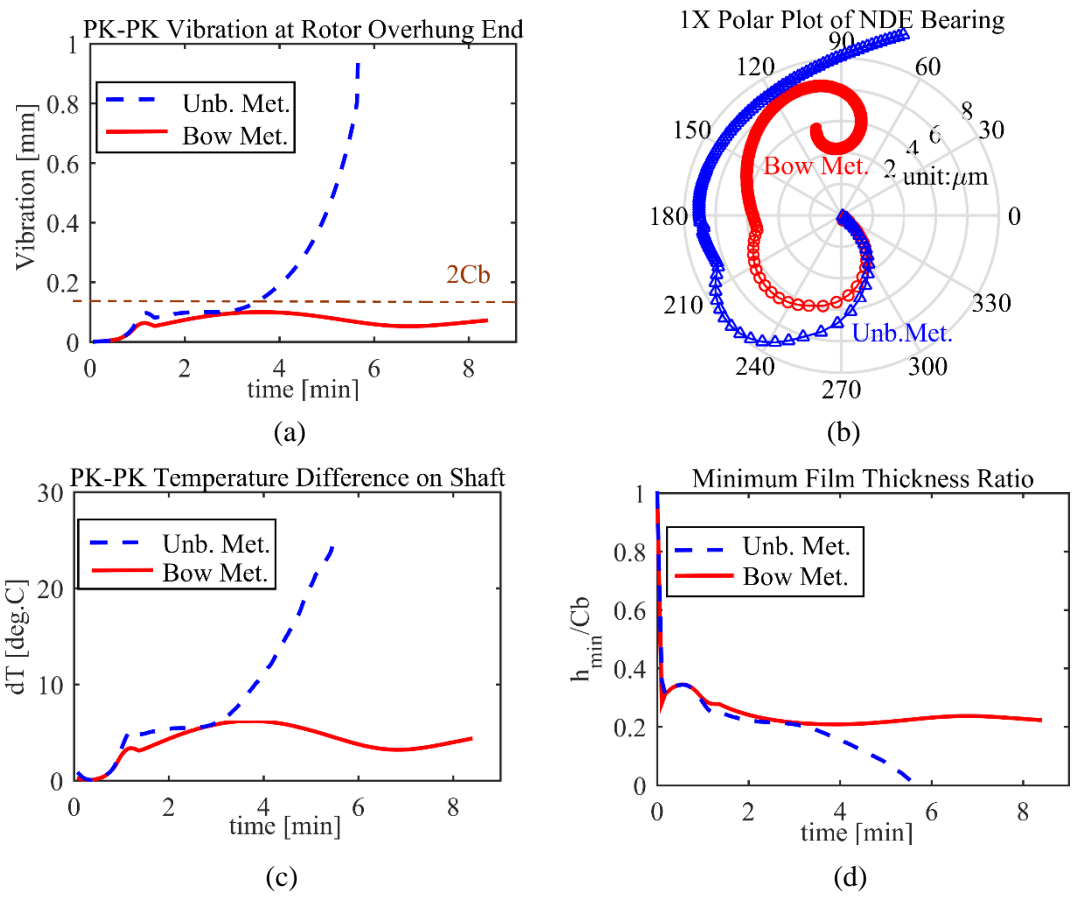
Fig. 4-10 Comparison of the thermal imbalance method and thermal bow method. (a) PK-PK vibration at rotor overhung end (b) 1X polar plot of the non-drive end bearing (c) PK-PK tempearture difference in the shaft (d) Minimum film thickness ratio.

4.2.3 Morton Effect Induced by the Permanent Bow and Disk Skew

The original mass imbalance is removed to check if the ME can be caused by only permanent bow or disk skew. Fig. 4-11 shows the location and magnitude of the permanent bow and disk skew angles in the simulation. Bow 1 is spatially linear and the peak magnitude at the end is 35.7 um, which is about 2/3 of the thermal bow at 8000 RPM in Fig. 4-9. Bow 2 is 50% of bow 1 and bow 3 has the same peak magnitude as bow 1 but is located between two bearings. In skew 1, disks at nodes 18 and 19 in the rotor-bearing

94

system (shown in Fig. 4-11) are tilted by 0.1°; skew 2 is 50% of skew 1; skew 3 has the same angle as skew 1 but the tilting disks are located at node 9 and 10. Note that the permanent bow and disk skew are fictitiously imposed for parametric studies in this section, and thus are not actually relevant to the real tested case [16].
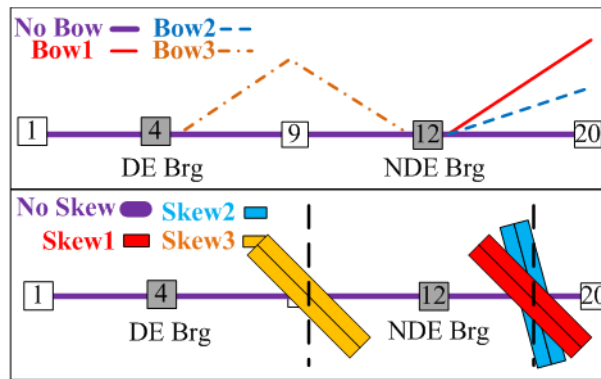
Fig. 4-11 Configuration of the permanent bow and disk skew.

Nonlinear transient analysis is done for each case at 6000 RPM, where both experiments and simulation illustrate good stability and negligible journal ΔT without any permanent bow or disk skew, as shown in Fig. 4-8. When the permanent bow or disk skew effect is considered, both the system dynamics and temperature distribution change considerably, as shown in Fig. 4-12 for the permanent bow cases and Fig. 4-13 for the disk skew cases. Note that both the vibration amplitude at the rotor NDE and PK-PK ΔT increase monotonically when the permanent bow or disk skewed angles become larger at the rotor NDE. When the bow or skewed disks are located between the bearings, the system still experiences an increase of vibration amplitude and ΔT, but with a much smaller magnitude. These results indicate that the ME can be induced by the permanent

bow or disk skew without additional mass imbalance, but is more sensitive when the excitation is located at the rotor NDE than the midspan. Note that in both Fig. 4-12 and Fig. 4-13, no spiral vibrations are observed and the bearing vibration finally converges to the steady state. This is because the simulated speed of 6 krpm is much lower than the ME instability onset speed, and therefore the rotordynamics still converges despite the large shaft ΔT induced by the ME.
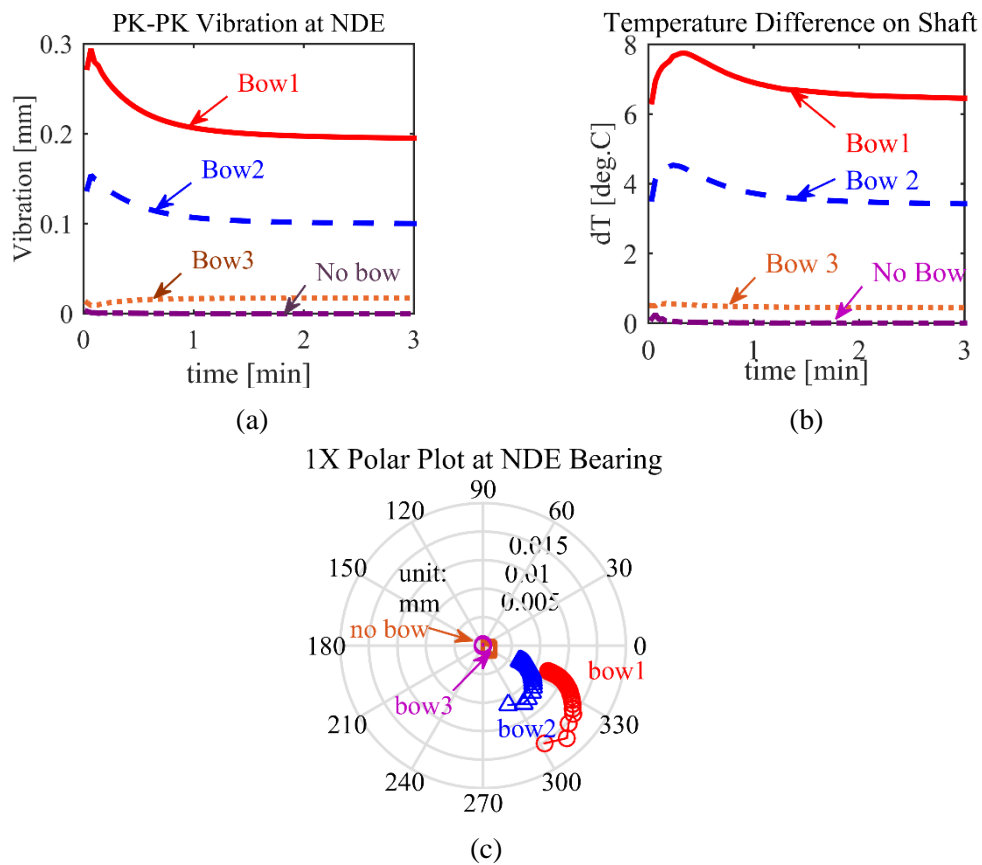
Fig. 4-12 Nonlinear transient analysis at 6 KRPM with permanent bow. (a) PK-PK vibration at rotor non-drive end (b) PK-PK temperature difference in shaft (c) 1X filtered polar plot at non-drive end bearing.
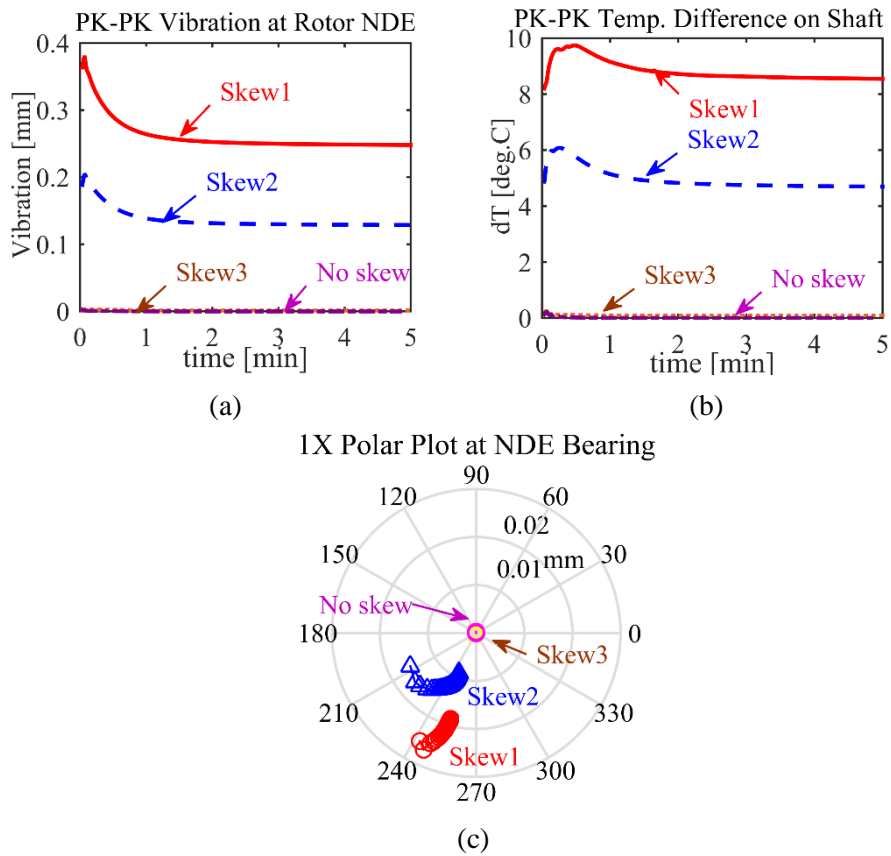
Fig. 4-13 Nonlinear transient analysis at 6 KRPM with disk skew. (a) PK-PK vibration at rotor non-drive end (b) PK-PK temperature difference in shaft (c) 1X filtered polar plot at non-drive end bearing.

4.2.4 Morton Effect Mitigation with the Coupling Stiffness Effect

The ME frequently occurs in a machine with "identical" counterparts that operate free from ME. This motivated the authors to investigate more salient features of the rotordynamic models as a step in the overall investigation of ME sensitivity to model features. One such feature studied is coupling lateral stiffness. Couplings connect two shafts to transmit power. Flexible couplings are designed to accommodate misalignment with radial stiffness typically varying from 10^5 to 10^8 N/m, while rigid couplings are used

when precise shaft alignment is required. The author's lab has conducted experiments to measure the transverse stiffness of various commercial couplings. The stiffness results for one test are plotted with respect to the torque and the transverse load in Fig. 4-14. The sensitivity of the coupling lateral stiffness to torque may be a distinguishing feature that explains why only a single unit may experience ME amongst a group of "identical" machines if they operate at different loads. Common practice is to model the coupling as an ideal lumped overhung mass [12] neglecting all lateral stiffness effects of the coupling. However, the transverse misalignment of both sides of the coupling will generate some lateral restoring (stiffness) forces which are generally neglected. Therefore, the coupling at the rotor end may be modeled more precisely as a lumped mass with a linear spring to ground. This added resistance may affect the deflections due to Morton journal heating and thus affects the ME thermal shaft bow distribution. In this portion of the study, we deviate from the actual machinery arrangement [16, 64] to consider the hypothetical case where the overhung disk end is coupled to a second machine via a flexible coupling. The purpose of the study is to investigate to what effect the radial stiffness of the coupling may influence the ME. Note that the same rotor configuration in Fig. 4-7 is utilized herein, but the coupling mass is assumed to have been integrated into the rotor for the present case. Thus, only the radial stiffness is considered explicitly in representing the coupling.

The effect of the NDE coupling radial stiffness on thermal bow is investigated first, prior to determining the effect that this stiffness has on the ME. The stiffness is attached to the right end of the model shown in Fig. 4-7 and varies in values as: 10^5, 10^6, 10^7, and 10^8 N/m. A prescribed temperature distribution is imposed in the thermal rotor within the

bearing length and the thermal shaft bow distribution is calculated in different cases. To simplify the problem, the temperature is assumed to be linear along the Y axis and uniform along the X axis with maximum temperature of 80℃ and minimum temperature of 76℃, as illustrated in Fig. 4-15. The calculated thermal bow profiles are illustrated in Fig. 4-16. Lower coupling stiffness, i.e. below 10^6 N/m has little effect on the bow. Larger stiffness tends to reduce the bow magnitude monotonically, which could have a mitigating effect on the ME. Fig. 4-17 shows the transient analysis of the rotor-bearing system at 7500 RPM with various stiffness of the coupling. Note that both journal ΔT and vibration at the NDE bearing are reduced with increased coupling stiffness, indicating mitigation of ME.

Thus, when the rotor experiences the Morton effect instability close to the coupling end, it may be best to select a coupling of higher transverse stiffness to restrict the rotor thermal deflection. This is especially recommended when reducing the coupling mass is difficult. Previous studies [12, 64] reported that reducing the coupling mass may benefit the ME mitigation, thus, providing an alternative approach if coupling stiffness modification is unfeasible.
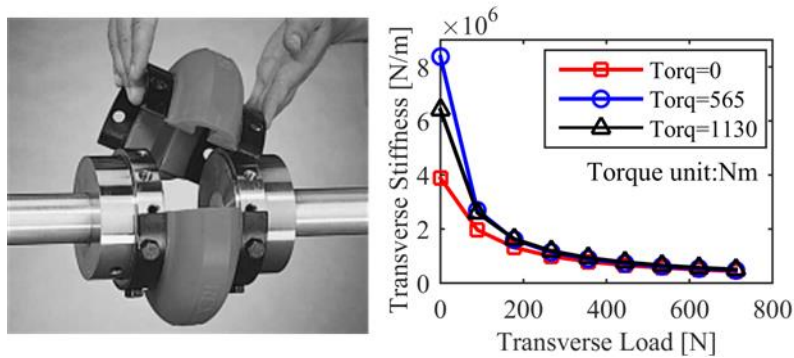
Fig. 4-14 Photo and transverse stiffness of a coupling.
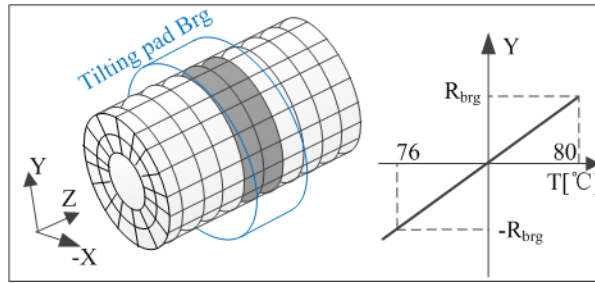
Fig. 4-15 Temperature distribution in the shaft.
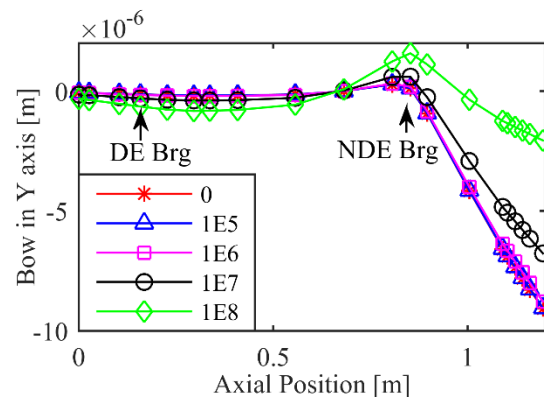
Fig. 4-16 Thermal bow with various coupling stiffness values (N/m).

(a)

(b)
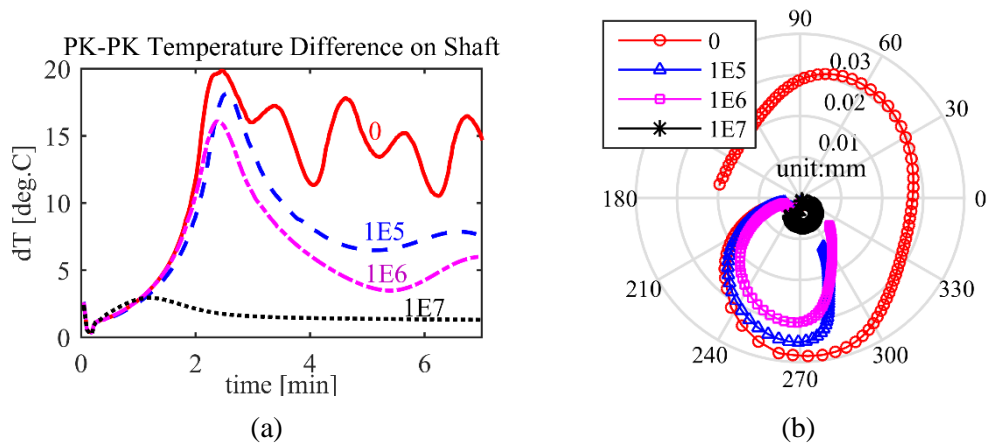
Fig. 4-17 Transient analysis at 7500 RPM with various coupling stiffness. (a) Journal temperature difference and (b) 1X polar plot at the NDE bearing.

5 PARAMETRIC STUDIES TO MITIGATE MORTON EFFECT[*]

The parametric studies in this section aim to provide practical solutions for suppressing the existing ME and also benefit designers for avoiding the potential ME. The parametric studies of the ME from earlier studies are reviewed below.

In 1996, de Jongh and Morton [12] experienced the ME in a centrifugal compressor, which exhibited high vibration level and continuous phase change on the non-drive end and could not achieve the maximum continuous operating speed (MCOS) of 11947 rpm. The final solution included the overhung mass reduction obtained by installing a lighter coupling hub on the non-drive end. In 1998, similar problems were reported by de Jongh and van der Hoeven [16]. The vibration level was found to be sensitive to the bearing clearance (C_b), and increasing the C_b from 1.9% to 2.2% (ratio defined by C_b/R_{brg}) could successfully suppress the vibration. In 1997, Corcoran [30] presented another ME case, where reducing the C_b by 33% could suppress the rotor vibration effectively but meanwhile caused overheating inside the bearing. Finally, a heavier coupling and modified bearings were installed to shift the critical speed for solving the problem.

In 2007, an air separation compressor with double overhung was reported to exhibit slow but dramatic synchronous oscillations by Marscher and Illis [22]. Dropping the oil supply temperature below $125^o F$ may trigger the high cyclic vibration, and

---

[*] Reprinted with permission from "Double Overhung Disk and Parameter Effect on Rotordynamic Synchronous Instability—Morton Effect—Part II: Occurrence and Prevention" by Tong, X., and Palazzolo, A., 2017. Journal of Tribology, 139(1), 011706. Copyright 2017 by ASME.

increasing the oil temperature above 128° F could effectively eliminate the high vibration. In 2008, Schmied [20] reported a ME case of a turbo-expander supported by two tilting pad bearings in the cryogenic industry. The investigated machine had two overhung impellers, and the measured vibration had a dominant synchronous component and spiral appearance at the MCOS of 18600 rpm. Reducing the bearing length and oil viscosity or increasing the C_b was the suggested solution to cure the ME.

In 2011, Lorenz and Murphy [18] observed the ME-induced spirals in a 4200 rpm rotating electric machine, and the divergent synchronous vibration prevented stable operation above 4000 rpm. Finally, the 4 lobe sleeve bearings were installed to replace the original partial arc bearings to suppress the excessive vibration. In 2012, Childs and Saha [26] conducted the ME parametric studies by simulating Keogh and Morton's symmetric rotor [35]. By reducing the initial imbalance from 100 g-cm to 50 g-cm, the vibration divergent speed increased from 7 krpm to 11 krpm. Increasing the bearing length-width ratio from 0.35 to 0.5 or reducing the lubricant viscosity from VG46 to VG32 could fully suppress the ME. In 2014, Suh and Palazzolo [40] performed the nonlinear transient analysis based on the single overhung compressor provided by de Jongh [16, 64]. They identified that reducing the supplying oil temperature, pivot stiffness and increasing the bearing clearance may mitigate the ME effectively. In 2015, Panara, et al [11], built the ME testing rig with three different overhung configurations, and the ME instability onset speed was found to decrease when the overhung mass increased. Panara concluded that the shift of the overhung critical speed could be directly linked to the shift of rotor stability threshold.

Previous research demonstrates that the ME can be quite sensitive to operating parameters, while the comprehensive analysis is still necessary to explore the root cause and effect. Moreover, testing experiences related to the ME are not entirely consistent in the adjustment of bearing clearance, supply oil temperature, overhung weight, etc., thus demanding more accurate guidelines for the ME suppression. Based on the published rotor model from de Jongh and Morton [12], parametric studies are conducted in this paper by perturbing the default conditions, i.e., the real operating parameters, to demonstrate the changes of rotor vibration and temperature. The ME instability onset speed, which can be closely related to the rotor critical speeds and oil cooling effect, is fully explained and summarized with respect to operational parameters.

5.1 Rotor-System Illustration

The simulated compressor has a double-overhung structure and is supported by two tilting pad journal bearings (TPJBs), illustrated in Fig. 5-1. Both bearings on the non-drive end (NDE) and drive end (DE) have identical configurations and are located in node 7 and 29, respectively.

The mechanical imbalance $2.8 \times 10^{-4} kg \cdot m$ is attached on node 4. Detailed parameters can be found in Table 5-1 and are also listed in [64]. The oil viscosity-temperature is expressed by $\mu = \mu_0 e^{-\alpha(T-T_0)}$, where μ_0 is the viscosity at $T_0 = 50^o C$. Convective boundary conditions are imposed on the thermal rotors and TPJBs with the ambient temperature of $30^o C$ and convection coefficient of 50 W/m^{2}K. Without

specification, the settings above apply to all simulations. In Section 5.3, parameters will

be varied based on the "baseline" in Table 5-1 to investigate the ME.
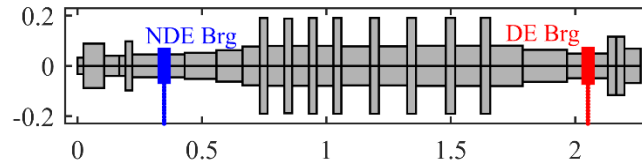
Fig. 5-1 Rotor configuration.

Table 5-1 Parameters of the rotor-bearing system

Lubricant parameters		Bearing parameters	
Viscosity at 50 ℃ [Ns/m^2]	0.0203	Load type	Load on Pad
Viscosity coefficients [1/℃]	0.031	No. pads	5
Supply temperature [℃]	50	Radius of shaft [m]	0.049
Inlet pressure [Pa]	1.32×10^5	Bearing clearance [m]	7.35×10^{-5}
Reference temperature [℃]	50	Preload	0.5
Shaft Parameters		Bearing length[m]	0.049
Heat capacity [J/kg ℃]	453.6	Pad arc length[degree]	56
Heat conductivity [W/mK]	50	Density[kg/m^3]	7850
Thermal expansion coeff.[1/℃]	1.1×10^{-5}	Heat conductivity [W/mK]	50
Reference temperature [℃]	30	Thermal expansion coeff. [1/℃]	1.1×10^{-5}
Thermal rotor length [m]	0.349	Reference temperature [℃]	30

5.2   Critical Speed Analysis

5.2.1   Morton Effect and Critical Speed

The nonlinear analysis in Section 3.2 reveals that the instability onset speed (IOS) is located at 11800 rpm. The "instability" indicates that above the IOS both the rotor vibration and temperature difference (ΔT) across the journal circumference increase drastically and the minimum film thickness of the NDE bearing drops below 10% of C_b. Although in practice the rotor vibration may reach trip level at a speed lower than the IOS, this quantitative definition is convenient to implement in simulations.

The critical speeds, mode shapes and unbalance response of the rotor-bearing system are listed in Fig. 5-2, and these predictions are based on a conventional treatment of both bearings with linear force coefficients. The 2nd bending mode is characterized with large vibration on the NDE, and the corresponding critical speed is located at 11927 rpm, close to the ME IOS. This is consistent with the testing record, which showed that the rotor vibration was quite large on the NDE and was closely related to its 2nd bending mode [12]. The ME induced instability can be explained as follows based on the mode shape: when the running speed approaches the critical speed, the initial mechanical imbalance causes synchronous vibration and journal ΔT (the temperature difference across the journal circumference); the overhung rotor structure is prone to amplify the thermal imbalance caused by the rotor thermal bow, especially at rotor ends, and the thermal imbalance may excite the overhung mode more violently. Without sufficient damping the thermal bow will soon drive the system into a synchronous instability.

(a)

(b)
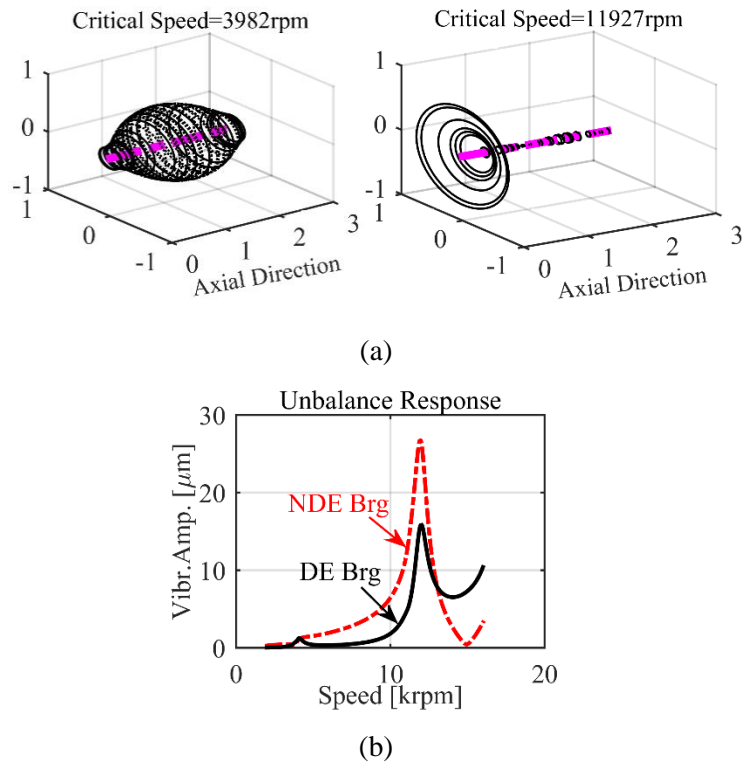
Fig. 5-2 (a) Critical speeds and mode shapes (b) Unbalance response.

Note that the 1st critical speed does not experience ME instability. Part of the reason is that for this specific rotor, the bearing orbit induced by the initial imbalance at the 1st critical speed is much smaller than the 2nd critical speed, which has a large overhung deflection. And the generated ΔT across the journal will be much lower for the 1st critical speed, causing smaller thermal bow and thermal imbalance. Moreover, even with identical journal ΔT, the rotor will still observe a much larger thermal deflection at the overhung node (in the 2nd mode) than the rotor midspan (in the 1st mode) due to the restraint from both bearings. For example, Fig. 5-3 shows the resulted thermal bow due to the prescribed temperature distribution in the NDE thermal rotor. Note that in Fig. 5-3(a), the NDE thermal rotor is prescribed with linear temperature distribution in *y* direction ($\Delta T = 4^{o}C$)

and uniform temperature in *x* and *z* direction, and the DE thermal rotor is kept at ambient temperature. Fig. 5-3(b) shows that the thermal deflection between bearings is much smaller than that on the rotor NDE. Therefore, the ME induced thermal imbalance is mainly located at the rotor end and can hardly excite the 1st bending mode.

(a)   (b)
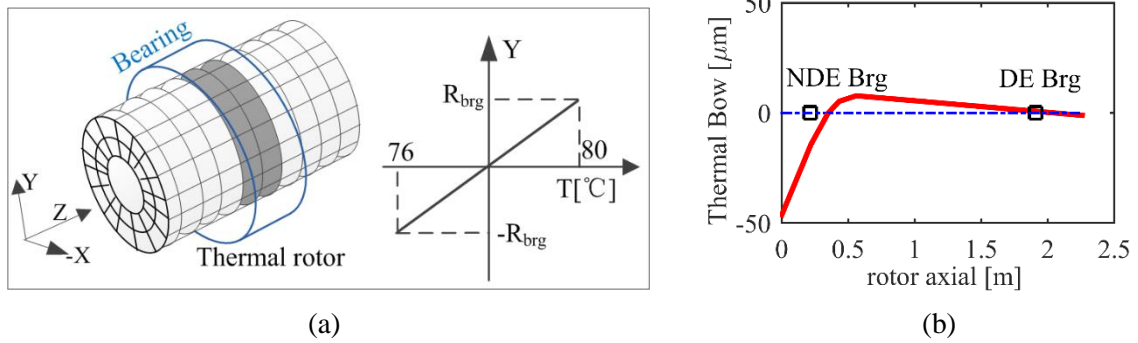
Fig. 5-3 (a) Prescribed temperature in the NDE thermal rotor, (b) thermal bow profile.

5.2.2   Instability Speed Band

During testing, de Jongh reported that by quickly raising the rotor speed, it was possible to run through the unstable speed range and reach stability at 13600 rpm [12]. Thus, the instability speed band starts from the IOS and ends at the stability recovery speed. The steady state and transient analysis illustrate the rotor vibration and temperature both in the speed and in the time domain, as shown in Fig. 5-4.
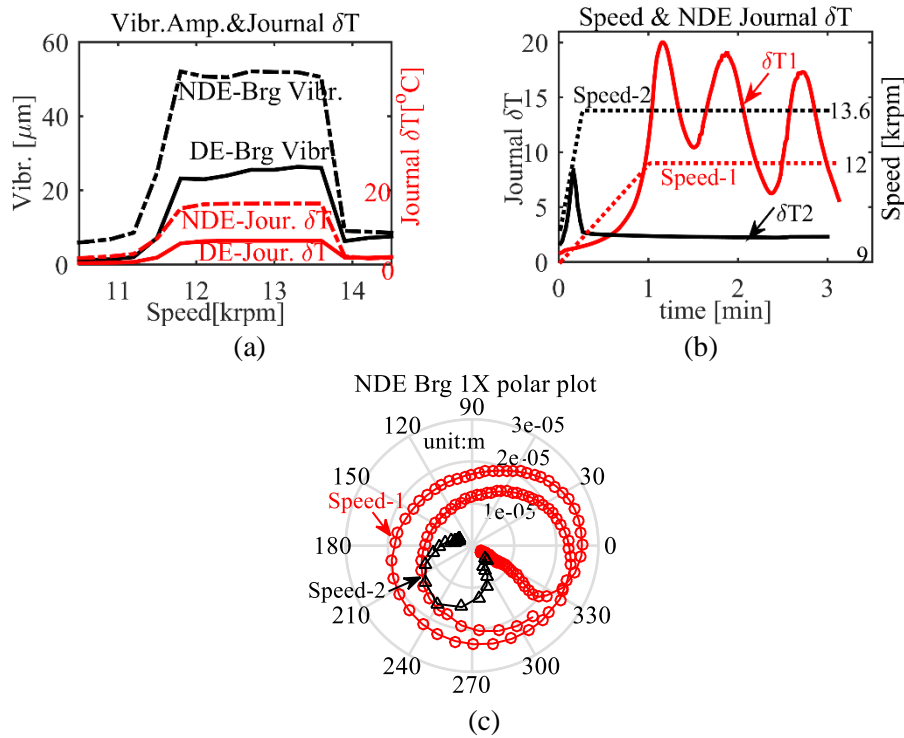
Fig. 5-4 (a) Steady state analysis for instability speed band (b) Transient analysis on NDE journal PK-PK ΔT (c) Transient 1X polar plot of NDE bearing.

Fig. 5-4(a) illustrates the PK-PK vibration level and the journal ΔT (which is the peak-peak temperature difference across the journal circumference and also the maximum value in all cross sections along the journal axial direction) at different speeds. Note that the vibration at both bearings and the ΔT across both journals increase steeply around 11.5 krpm and then plunge at 13.6 krpm. The predicted instability speed band is close to de Jongh's observation. In Fig. 5-4(b), two different speed curves are tested for transient analysis: (1) the speed starts at 9 krpm and increases linearly to 12 krpm within 1 min and then stays constant; (2) the speed starts at 10 krpm and increases linearly to 13.6 krpm within 15s and then stays constant. The first case is designed to verify the IOS, and the second is to demonstrate that by quickly raising the speed, it is possible to pass the

instability speed band and regain stability over 13.6 krpm. Results show that for "speed-1", the journal ΔT oscillates at high level and the 1X polar plot in Fig. 5-4(c) shows that the bearing orbit develops into large limit cycles; for "speed-2" the journal ΔT rises steeply but soon drops to the acceptable level after the speed passes the instability speed band. Note that the 2nd critical speed, which plays an important role in facilitating the ME, is within the instability speed band. Detailed discussions will be presented later that changing the 2nd critical speed by adjusting the operating parameters, e.g., bearing clearance, oil viscosity, etc., can also shift the ME instability speed band.

5.2.3 Parameter Studies of Critical Speed

The ME is closely related to the critical speed and mode shapes, and though API 617 [48] has detailed the minimum requirement including the separation margin and unbalance response amplitude, accessories such as couplings and bearing housings may add additional mass and stiffness to the system, shifting the critical speeds unexpectedly. Moreover, the operational conditions, such as ambient temperature, lubricant viscosity, etc., may differ from the standard parameters, and can also affect the rotordynamics. Thus, performing the sensitivity study of critical speeds by varying the operating parameters is necessary for the ME analysis. Note that the original operational condition is: oil supplying temperature of $50^{o}C$, bearing clearance of 100%, viscosity of VG32, pivot offset of 0.5, mixing coefficient of 80% (ratio defined by the hot oil carried over from the previous pad trailing edge to the next pad leading edge).

Based on the aforementioned rotor, Fig. 5-5 shows the damped unbalance responses at various conditions. In each subplot, only one operating parameter is changed

109

while others are the same as original. In Fig. 5-5(e), the original overhung case is marked with "large", and the reduced overhung case is "small", where the overhung mass is reduced by 8.1 kg at the NDE and 12.5 kg at the DE, as suggested by [48] to cure the ME. Note that the 2nd critical speed becomes higher by increasing the supply oil temperature, viscosity, pivot offset or reducing the bearing clearance, overhung mass. From intuition, increasing the supply oil temperature may raise the temperature of the journal & bearings and cause more thermal expansion. The reduced bearing clearance will make the bearing stiffer. Likewise, increasing the lubricant viscosity, pivot offset can increase both the bearing load-carrying capacity and the bearing stiffness, and finally the rotor critical speed will be raised by the stiffer bearings.
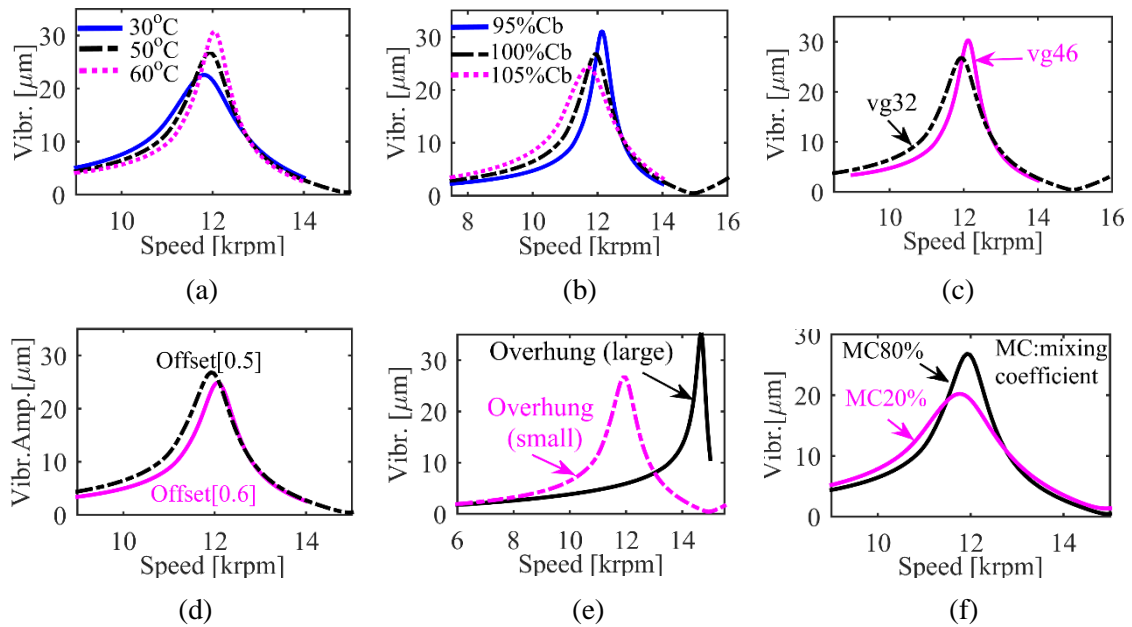
Fig. 5-5 Unbalance response with various conditions.(a) oil supplying temperature (b) bearing clearance (c) oil viscosity (d) pivot offset (e) overhung mass (f) mixing coefficient.

5.3 Parameter Studies of the Morton effect

The nonlinear transient analysis together with the steady state analysis provide two high fidelity modeling tools to evaluate the ME via a transient thermodynamic process in the time domain and the IOS in the frequency domain. Note that the steady state analysis is based on the fully nonlinear transient integration designed for the double overhung rotors and differs from the classic steady state frequency analysis in the control theory.

5.3.1 Inlet Lubricant Temperature

The steady state analysis with supply oil temperature at 30^oC and 50^oC is performed and the results are plotted in Fig. 5-6. The speed range within the red rectangles in Fig. 5-6(a) experiences the ME-induced instability, i.e., the minimum film thickness drops below $10\% C_b$. By reducing the inlet oil temperature from 50^oC to 30^oC, the IOS decreases from 11.8 krpm to 11.5 krpm, consistent with the critical speed change in Fig. 5-5(a). The shifting of IOS indicates that the rotor may experience intolerable vibration and will be tripped at lower speeds. For this rotor, the ME at lower speeds are intensified by reducing the inlet oil temperature because (1) the cooler inlet oil can reduce the average journal temperature. For instance, compared with the original inlet oil at 50^oC, dropping the oil temperature to 30^oC will reduce the average journal temperature by 15^oC, as shown in Fig. 5-6(b). The smaller thermal expansion of the journal will result in a larger bearing clearance and a lower rotor critical speed, which deteriorates the speed separation margin. (2) At lower temperature the oil viscosity will increase, thus intensifying the viscous shearing and raising the journal ΔT.

111

Note that the ME is induced by the journal ΔT, not the average journal temperature, so reducing the latter with lower inlet oil doesn't necessarily mitigate the ME. One may argue that both the differential and average journal temperature can be reduced simultaneously by providing sufficient cooling oil at even lower temperature. Note that in practice, the inlet oil at the pad leading edge is not completely supplied by the external lubrication system, and the hot oil carried over from the previous pad trailing edge can be the majority. Thus, the actual cooling effect is restricted if the bearing lubrication design is not optimized. This oil carryover ratio is set to be 80% without specification in all simulations and will be fully discussed in Section 5.3.7. Note that the ME on the DE is less serious than the NDE, and thus only the latter will be discussed in all following results.

Fig. 5-6 Steady analysis with different oil supplying temperature. (a) PK-PK vibration amplitude at bearing nodes (b) average temperature of journals (c) PK-PK temperature difference across journals on both rotor sides.

The transient analysis is conducted with the fully nonlinear double overhung method (without specification, this applies to all other transient analysis in this paper) and the results are demonstrated in Fig. 5-7. The speed curve in Fig. 5-7(a) indicates that the rotational speed increases linearly from 9 krpm to 11.8 krpm within the 1st min and then stays constant for 40 s before it drops back to 9 krpm. Without specification, this speed curve applies to all transient simulations afterwards. The ME is mitigated with hotter inlet oil since the vibration, journal ΔT and thermal imbalance at $60^{o}C$ are only half of those at $30^{o}C$. Fig. 5-7(c) is obtained by vector summing the thermal imbalance components of all nodes and plotting with respect to time.

(a)

(b)

(c)

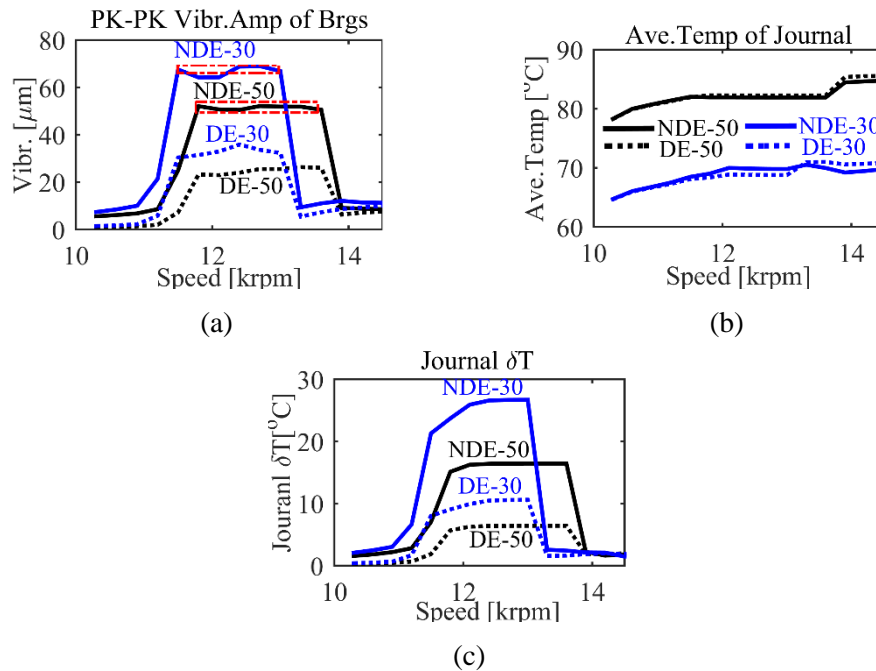*Fig. 5-7 Transient analysis with different oil supply temperature. (a) PK-PK vibration amplitude at the bearing (b) average temperature and PK-PK temperature difference in journal (c) resultant thermal imbalance.*

113

For the aforementioned rotor, the IOS is below the dominating critical speed, which has large overhung deflection in its mode shape (actually the rotor was tripped at lower speed than IOS during testing [48]). In this case, engineers may suppress the ME by increasing the supply oil temperature, while considering the following constraints (a) the bearing clearance can be significantly reduced due to the insufficient oil cooling and the thermal expansion of the journal & bearing, and (b) the oil viscosity is very sensitive to its temperature and will almost drop by 50% with $20^o C$ increase in temperature. However, for the rotor operating at overcritical speed, reducing the oil temperature, in most cases, may increase the separation margin and thus suppress the ME, and this will be explained in Section 5.4.

5.3.2 Bearing Clearance

The operating bearing clearance can be affected by the bearing manufacture, assembly tolerance and the babbitt deformation due to wearing, heating, etc. Engineers may simultaneously observe the low vibration level in one rotor and the violent spiral vibration induced by the ME in another identical rotor. Based on the aforementioned rotor model, the bearing clearance is adjusted by $\pm 5\%$ to investigate its effect on the ME, and the transient analysis results are shown in Fig. 5-8, marked with $95\% C_b$, C_b and $105\% C_b$ respectively. Fig. 5-8(a) demonstrates that the vibration at the NDE bearing is quite sensitive to the bearing clearance: reducing the clearance by 5% can suppress the vibration amplitude at the NDE bearing from 31 μm to 17 μm, while increasing the clearance by 5% may raise the vibration level to 53 μm. Fig. 5-8(b) and Fig. 5-8(c) show that the smaller bearing clearance increases the average journal temperature by intensifying the oil viscous

shearing and meanwhile decreases the journal ΔT and thermal imbalance, which mitigates the ME. The ME suppression with smaller bearing clearance around 11.8 krpm indicates that the IOS shifts to a higher level, which is consistent with the critical speed change in Fig. 5-5(b). A larger separation margin between the operating speed and the critical speed is helpful to suppress the ME since the rotor vibration becomes lower and the journal ΔT is reduced. The journal average temperature in Fig. 5-8(b) illustrates the negative effect (downside) of reducing the bearing clearance, i.e., the overheating problems due to insufficient oil cooling and increased viscous shearing. The simulations are consistent with Corcoran [30], where the ME suppression was reported through clearance reduction and meanwhile the overheating problem was observed.
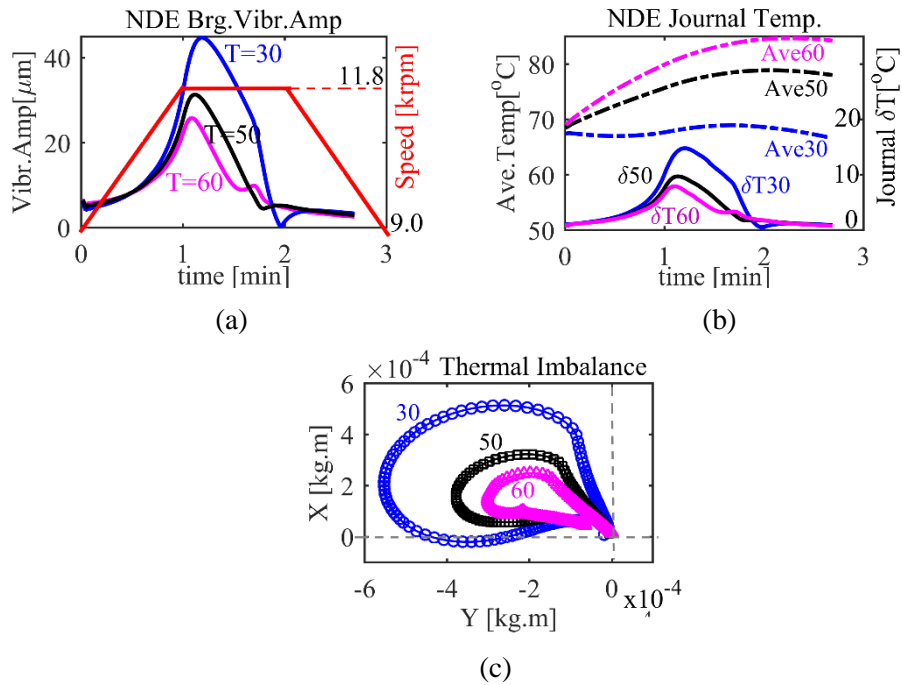

Fig. 5-8 Transient analysis with different bearing clearances. (a) PK-PK vibration amplitude at the bearing node (b) average temperature and PK-PK temperature difference of journal (c) rotor thermal unbalance.

Note that the bearing clearance effect is investigated by applying a small change to the original clearance value, and therefore the dynamic characteristics of the system, including the rotor critical speeds and mode shapes, are still close to their original levels.

When the bearing clearance is significantly changed, the system dynamic behavior can be completely different, and the above suggestion of the ME mitigation through bearing clearance reduction may not apply. However, the general guideline still holds: adjust the bearing clearance to provide more damping and larger separation margin for the dominating critical speed. One may refer to de Jongh's case [16], where the clearance is increased by 15.8% to reduce the amplification factor below 2.5 at the dominating critical speed.

5.3.3 Oil Viscosity

Higher oil viscosity can improve the bearing load capacity and meanwhile intensify the viscous shearing inside the bearing. The transient analysis in Fig. 5-9 illustrates the results from various viscosities. Fig. 5-9(a) shows that by increasing the oil viscosity from VG32 to VG46, the average journal temperature is raised by 4^oC in maximum, and the peak value of the journal ΔT is reduced by 30%. The higher average temperature with VG46 will expand the journal more, thus reducing the operating bearing clearance and increasing the rotor 2nd critical speed by 240 rpm, as shown in Fig. 5-5(c). Moreover, the lower journal ΔT will generate less thermal imbalance, thus reducing the rotor vibration and bearing orbit, and the minimum film thickness will be larger relative to the VG32 case, as shown in Fig. 5-9(c).
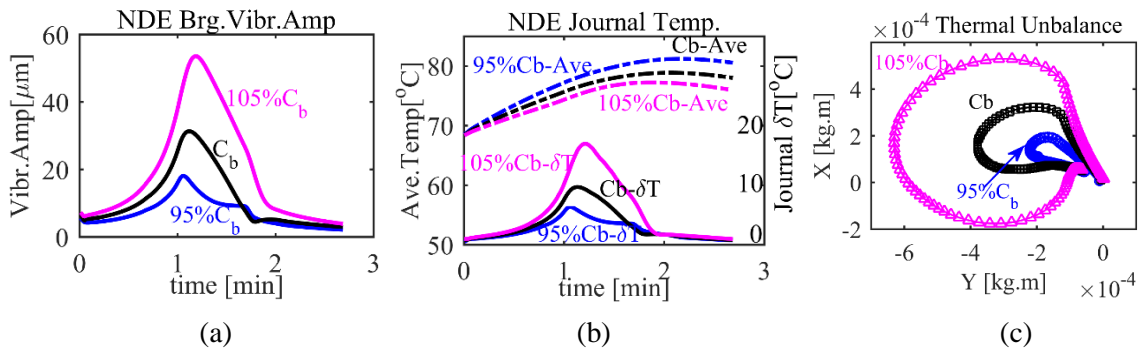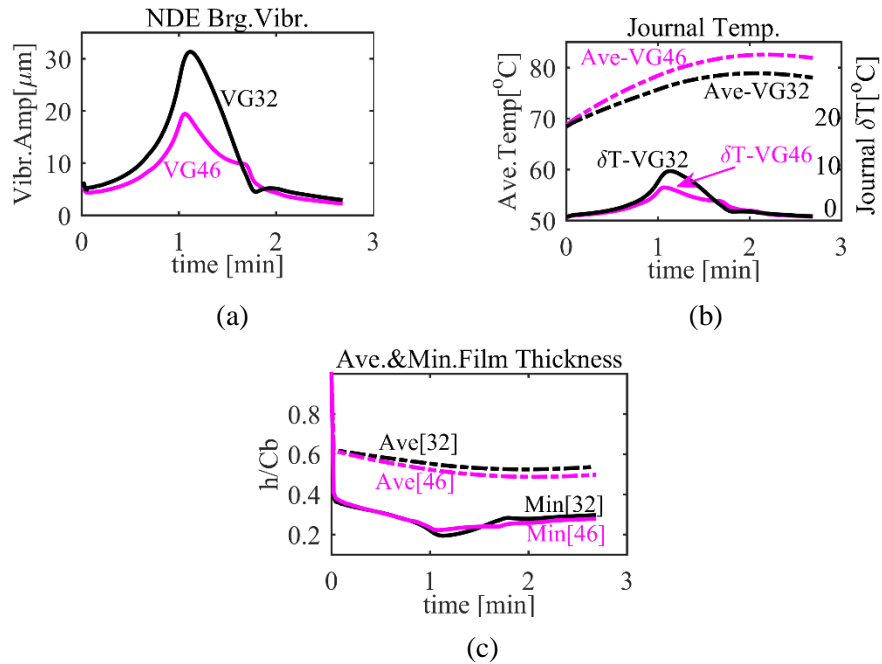
Fig. 5-9 Transient analysis with different viscosities. (a) PK-PK vibration amplitude at the bearing node (b) average temperature and PK-PK temperature difference of journal (c) average and minimum film thickness of bearing.

The transient analysis shows that the ME is mitigated with higher oil viscosity for this rotor considering that both the vibration level and the journal ΔT are suppressed. Therefore, the IOS is concluded to shift to higher speed by increasing the oil viscosity, and this trend is consistent with the critical speed change. Results above demonstrate that the larger oil viscosity doesn't necessarily cause higher journal ΔT, which also depends on the bearing obit size, eccentricity, etc. The bearing with a centered, circular, large amplitude orbit is reported to be prone to the ME [17]. For the aforementioned rotor, the higher oil viscosity helps raise the critical speed further from the MCOS and reduce the bearing orbit size, thus decreasing the journal ΔT. However, similar to the bearing clearance reduction case, higher oil viscosity usually increases the average bearing &

journal temperature (in Fig. 5-9(b)), thus increasing the possibility of overheating. Schmied [20] took an opposite strategy, where the critical speed was greatly increased by expanding the rotor diameter and the oil viscosity was reduced to eliminate the heat generation. This method is consistent with our guideline to increase the speed separation margin, but the viscosity is no longer used to adjust the critical speed.

5.3.4 Overhung Mass

In [12], the overhung mass on the NDE and DE were finally reduced by 8.1 kg and 12.5 kg respectively to cure the ME. The steady state analysis with different overhung mass is illustrated in Fig. 5-10. "Large" indicates the original rotor model without overhung reduction, and "Small" indicates the reduced overhung model. Compared with the original IOS at 11.8 krpm, the new IOS with overhung reduction is raised over 14 krpm, which is consistent with the critical speed change in Fig. 5-5(e). For the modified rotor, the vibration, journal ΔT and resultant imbalance (vector summation of the mechanical and thermal imbalance) stay at low levels around the MCOS of 12 krpm. Fig. 5-10(c) shows that the shaft isotherms are concentric close to the MCOS for the reduced overhung model, indicating that the journal ΔT across the circumference is quite small.

The ME mitigation for the reduced overhung model is due to (1) the greater separation margin of the 2nd critical speed, which helps to reduce the bearing orbit size, and (2) the reduction of the thermal imbalance at both rotor ends, considering that the thermal imbalance is proportional to the mass and thermal deflection.

118
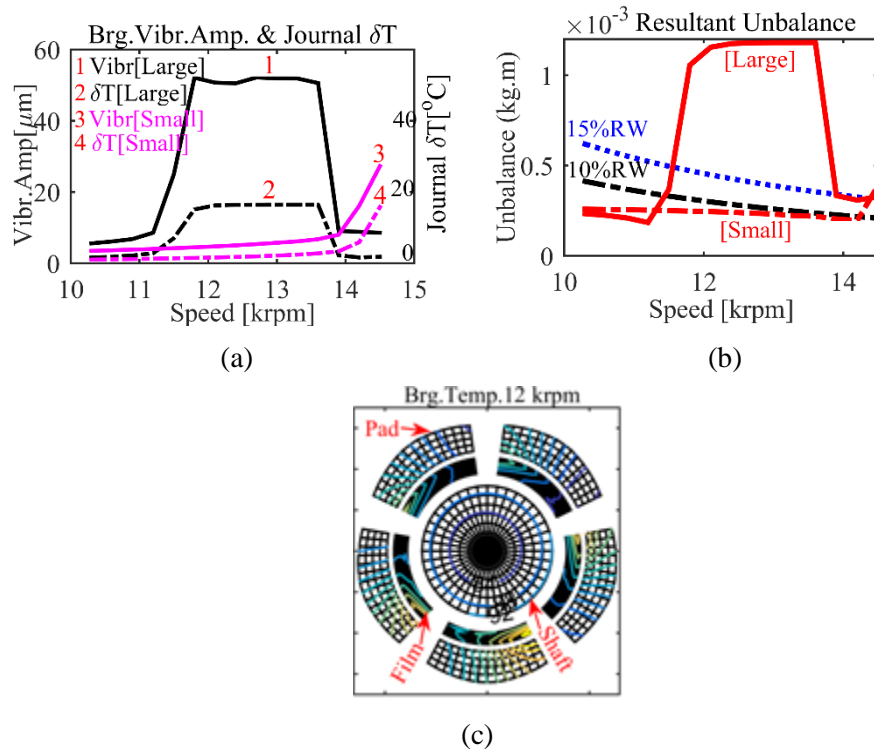
Fig. 5-10 Steady analysis with different overhung masses. (a) Bearing vibration amplitude and PK-PK journal temperature difference. (b) Resultant imbalance. (c) Bearing isotherms for the reduced overhung model.

5.3.5 Residual Bow and Disk Skew

The shaft residual bow (RB) and disk skew (DS) commonly exist in rotormachineary due to the rotor manufacture and assembly tolerances. Earlier studies [60, 63] revealed that the RB and DS may affect the rotor dynamics significantly, complicating the unbalance response especially in the vicinity of critical speeds. Though both have not been related to the ME or reported in [12], they may provide additional synchronous excitation similar to the mechanical imbalance, generating the journal ΔT and causing the ME. Based on the aforementioned compressor, various bows and disk skewed angles are imposed for parameter studies, shown in Fig. 5-11(a). Note that the linear RBs are imposed

119

on the NDE with different magnitude: "++bow" indicates a bow magnitude of 0.001 inch on the left end, and "+bow" is 50% smaller; "++skew" and "+skew" indicate that the left disk is tilted by 0.3^o and 0.15^o respectively. Note that the initial mechanical imbalance is removed in this section, and thus the ME will be induced solely by the RB or DS.
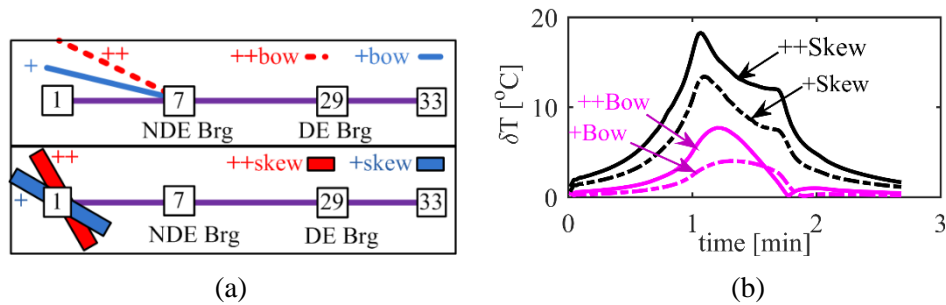
Fig. 5-11 Residual bow and disk skew effects. (a) Excitation configurations (b) Journal PK-PK temperature difference.

Fig. 5-11(b) illustrates that both the RB and DS can cause the ME in the absence of initial imbalance, and larger RB or DS will generate larger journal ΔT, causing a more severe ME. Moreover, the relationship of excitation-ΔT cannot be simply linearized considering that the journal ΔT of "++skew" is not twice that of '+skew' and also the ΔT profile of '++bow' differs from that of '+bow'.

5.3.6 Initial Mechanical Imbalance

The initial imbalance is reduced to 10% of its original to check the transient response, shown in Fig. 5-12. With smaller imbalance, the peak vibration amplitude at the NDE bearing decreases from 31.3 μm to 5.3 μm, and the peak journal ΔT decreases from $9.7^o C$ to $1.6^o C$, indicating a less severe ME. In the absence of initial imbalance (marked

by "0% me" in Fig. 5-12), the ME is completely eliminated with zero vibration amplitude and journal ΔT. In practice, despite the impossibility to achieve perfect-zero mechanical imbalance for engineers, simulations demonstrate that reducing the initial imbalance can benefit the system stability by suppressing the ME to an acceptable level. Note that the relationships of both "imbalance-vibration" and "imbalance-ΔT" are not exactly linear, proving that it is necessary to establish a precise thermo-elasto-hydro-dynamic model rather than try to simplify the ME with linearized assumption.
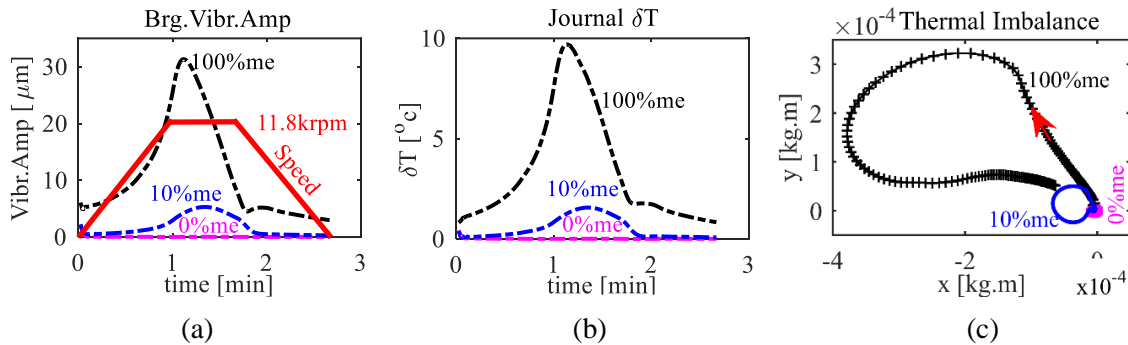
Fig. 5-12 Transient analysis with various initial imbalances. (a) PK-PK vibration amplitude at the bearing node (b) PK-PK temperature difference across the journal circumference (c) thermal imbalance.

5.3.7 Mixing Coefficient

The mixing coefficient (MC), also termed the carryover flow ratio, describes the percentage of the hot oil carried over by the shaft from the trailing edge of one pad into the leading edge of the next pad. The lower the MC, the more effective the bearing cooling. Reduction of this value can be achieved by optimizing the lubrication design to introduce more inlet oil directly into the pad leading edge. In all simulations elsewhere in this paper,

the default MC is set to be 80%, and the MC is reduced to 20% herein for parameter studies, shown in Fig. 5-13.

In Fig. 5-13(a), for the MC of 20%, the average journal temperature drops from the initial condition of 70^oC to 59^oC due to the sufficient oil cooling with inlet oil at 50^oC. For the MC of 80%, the average journal temperature continuously increases to 80^oC, expanding the journal more and reducing the bearing clearance & film thickness, shown in Fig. 5-13(b). The maximum journal ΔT is also reduced from 10^oC to 7^oC by better cooling with the MC of 20%, indicating that the ME is suppressed. Note that the effect of reducing MC differs from lowering the supply oil temperature in Section 5.3.1, considering that the latter is observed to intensify ME for this specific rotor with a lower IOS. Although in both cases the average journal temperature decreases and the 2nd critical speed drops, reducing the MC from 80% to 20% can significantly improve the oil cooling efficiency and thus reduce both the journal average temperature and the journal ΔT. However, simply decreasing the supply oil temperature without reducing the MC cannot cool the journal sufficiently and the ME is enhanced due to the lower critical speed (in Section 5.3.1, the journal ΔT actually increases due to the larger bearing orbit caused by the smaller separation margin).
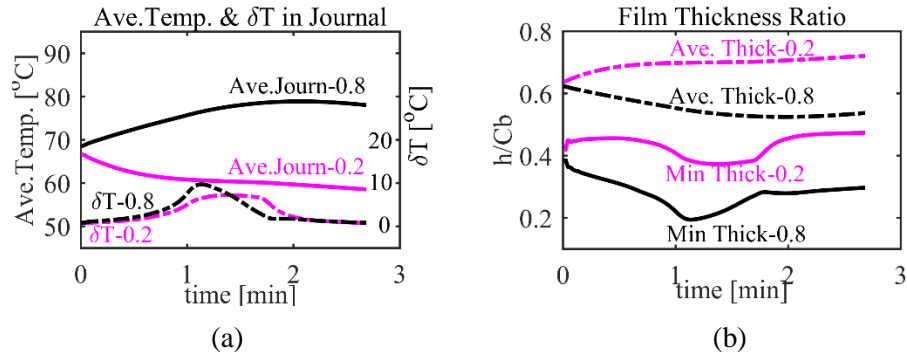
Fig. 5-13 Transient analysis with mixing coefficient of 20% and 80%. (a) Journal average temperature and PK-PK temperature difference across circumference (b) Average and minimum film thickness ratio.

5.3.8 Pivot Offset

Asymmetric pivot offset, usually larger than 50%, is reported to be effective in reducing the oil temperature compared with the central pivot offset [65, 66]. In the following case, the pivot offset is increased to 60% to compare with the original 50% and the results are illustrated in Fig. 5-14. The 60% offset is quite effective in suppressing the rotor vibration from 31 μm to 22 μm and the journal ΔT from $9.7^o C$ to $6.4^o C$, indicating a less severe ME. Moreover, the oil viscous shearing is also less severe considering that the average temperature for the lubricant and journal is reduced by $11^o C$ and $8^o C$, respectively. Both the average and minimum film thickness are larger than those with 50% offset, proving that the system is more stable. The ME mitigation with the 60% pivot offset indicates that the IOS shifts to the higher level, which is also consistent with the critical speed change in Fig. 5-5(d).

123
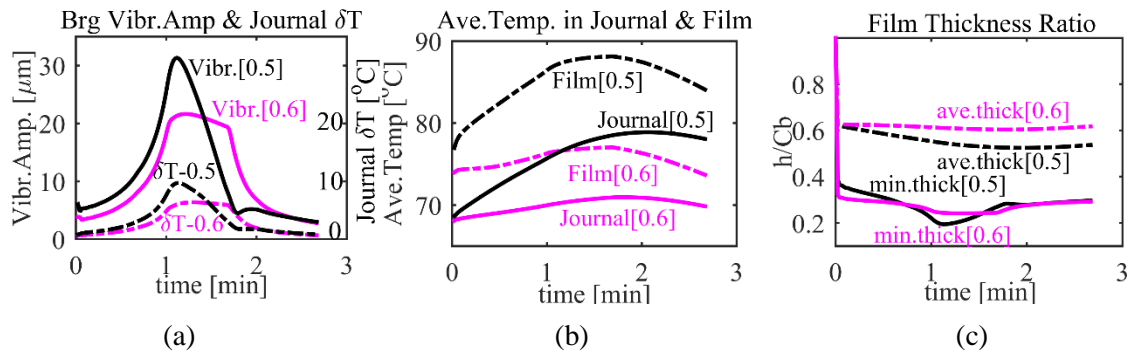
Fig. 5-14 Transient analysis with pivot offset at 50% and 60%. (a) Vibration amplitude of bearing and PK-PK temperature difference of journal (b) Average temperature of the lubricant and journal (c) Average and minimum film thickness ratio.

5.4 Remedies for the Morton effect

ME suppression can be achieved by either reducing the viscous shearing in the lubricant or impeding the heat flux into the journal. The former aims to reduce the heat generation by optimizing operational parameters (e.g. bearing clearance, lubricant viscosity, etc.), and the latter blocks the heat transfer route by inserting additional isolation components between the lubricant and journal.

5.4.1 Optimization of Operational Parameters

Operational parameters should be optimized to increase the separation margin between the dominating critical speed and the MCOS to avoid large bearing orbits and journal ΔT. Moreover, considering that the ME is caused by the uneven oil heating, sufficient oil cooling is helpful to reduce the journal average temperature and ΔT, thus mitigating the ME. However, engineers may encounter situations where adjusting certain parameters may benefit the oil cooling efficiency but meanwhile may deteriorate the separation margin, or the other way around. For instance, reducing the supply oil

124

temperature for the discussed rotor can improve the cooling efficiency, but simultaneously shifts the critical speed closer to the MCOS, thus eventually increasing the journal ΔT and intensifying the ME. In practice, the ME mitigation may be achieved by adjusting multi-parameters simultaneously. For instance, in Corcoran's case [30], solely adjusting the lubricant temperature was reported to have little effect, and reducing the radial bearing clearance could suppress the vibration but caused overheating problems. Final solutions included both the overhung coupling change and the bearing modification for [30].

The instability speed band (ISB) for the current rotor is similar to a gate function (solid line in Fig. 5-15) with lower boundary at the IOS and upper boundary at the stability recovery speed. Speeds within the ISB will normally observe excessive rotor vibration violating API 617. Rotors running at such constant speed for long time will exhibit 1X spiral at the bearing node, and the bearing orbit may develop into limit cycles, or even direct rubbing problems may occur between the pads and journal. Depending on the practical design, the rotational speed can be located on either side of the ISB (see Fig. 5-15). By adjusting the operating parameters, for instance, the ISB shifts to the right (marked with dashed lines in Fig. 5-15) and the rotational speed in "Region2" will experience more serious ME, while the speed in "Region1" will observe the mitigated ME. If the ISB shifts to the left, the ME for both regions will behave in the opposite way. To better illustrate the application, one may refer to another ME case reported by de Jong [16], where the dominating critical speed is located around 7.5 krpm with its mode shape exhibiting large deflection at the overhung end. The IOS for [16] is experimentally found to be around 7.2 krpm and the rotor tested at 8.5 krpm displays 1X spirals. From the theory

125

above, we know that the testing speed is located in "Region2". To suppress the ME, we need to increase the bearing clearance or reduce the oil supply temperature (opposite to what we have done to [12]) to shift the critical speed and the ISB to the left, thus being away from the testing speed at 8.5 krpm. These methods are verified by de Jong [16] through testing and Suh [29] through simulations.

Note that in most cases the excessive vibration will cause the rotor to trip before it can reach "Region2" (although by raising the speed fast, it is possible to run through the ISB for certain cases), and thus engineers will focus more on the instability onset speed and "Region1".
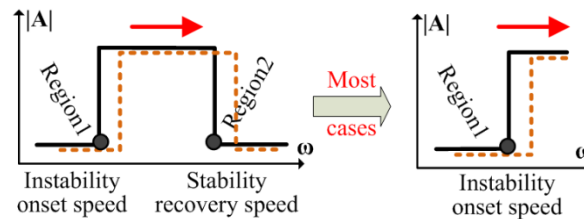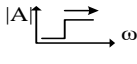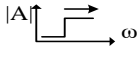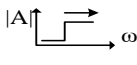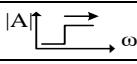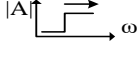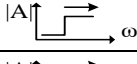
Fig. 5-15 Instability speed band and operating speed regions.

Table 5-2 summarizes the parametric studies of the ME based on the current rotor model, and the results are based on the univariate analysis although multi-parameters may be adjusted in practice. Note that to suppress the ME, most parameters in Table 5-2 are adjusted aiming to provide a larger separation margin between the dominating critical speed Ω and the running speed. However, lowering the mixing coefficient may mitigate the ME by providing more efficient cooling effect, which may compensate the deterioration of the separation margin.

126

Table 5-2 Summary of parameter influence on the Morton Effect

Parameter	Instability onset speed	Explanation
↑ Supply oil temperature	$\|A\|$ vs ω (step shift right)	Reduce cooling efficiency, expand the journal thermally, shrinking C_b, increase critical speed Ω.
↓ Bearing clearance	$\|A\|$ vs ω (step shift right)	Stiffen the rotor and increase Ω, may cause overheating inside bearings due to intensified viscous shearing
↑ Oil viscosity	$\|A\|$ vs ω (step shift right)	Intensify oil viscous shearing, raise journal average temperature, expand the journal and increase Ω
↓ Overhung mass	$\|A\|$ vs ω (step shift right)	Increase Ω, reduce thermal imbalance
↓ Residue bow/disk skew/initial imbalance	$\|A\|$ vs ω (step shift right)	Reduce synchronous excitation and bearing orbit size, reduce journal ΔT
↓ Mixing coefficient	$\|A\|$ vs ω (step shift right)	Increase oil cooling efficiency, reduce journal ΔT
↑ Pivot offset	$\|A\|$ vs ω (step shift right)	Increase cooling efficiency, reduce journal average temperature and ΔT, increase Ω.

5.4.2 Isolation of Thermal Flux

The ME is in essence caused by the journal circumferential ΔT due to the asymmetrical heat flux. An effective approach to mitigate the ME is to isolate the heat flux into the journal, and this can be achieved by adding isolating components, such as heat barrier sleeves or ceramics, between the journal and lubricant.

The heat barrier sleeve, which is mounted on the journal and rotates with the rotor, is proposed by de Jongh to suppress the ME [16]. Air gap is intentionally designed inside the sleeve to prevent the heat flux into the journal. Similarly, a ceramic sleeve is designed by us to be shrink-fitted on the journal to isolate the heat flux since the ceramic thermal conductivity can be quite low. The schematics of both methods are illustrated in Fig. 5-16. In simulations, both the sleeve gap length L_1 and the ceramic length L_2 are set to be the bearing length, h_1, h_2, h_3 are all 3 mm, the thermal conductivity of the ceramics, air and

steel (in the air sleeve) is 3, 0.024 and 50 (unit: W/mK) respectively. The steady state analysis for the aforementioned rotor with the heat barrier sleeve and the ceramic isolation is performed, shown in Fig. 5-17.

(a) (b)
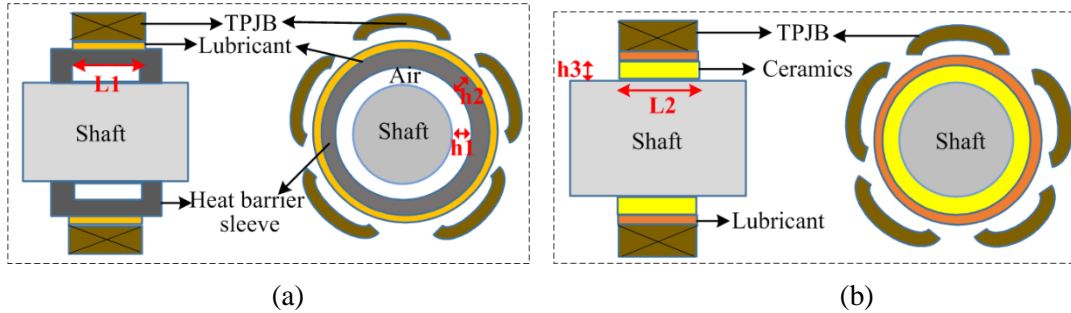
Fig. 5-16 Schematics of (a) Heat barrier sleeve with air gap (b) Ceramic isolation.

(a) (b) (c)

(d) (e) (f)
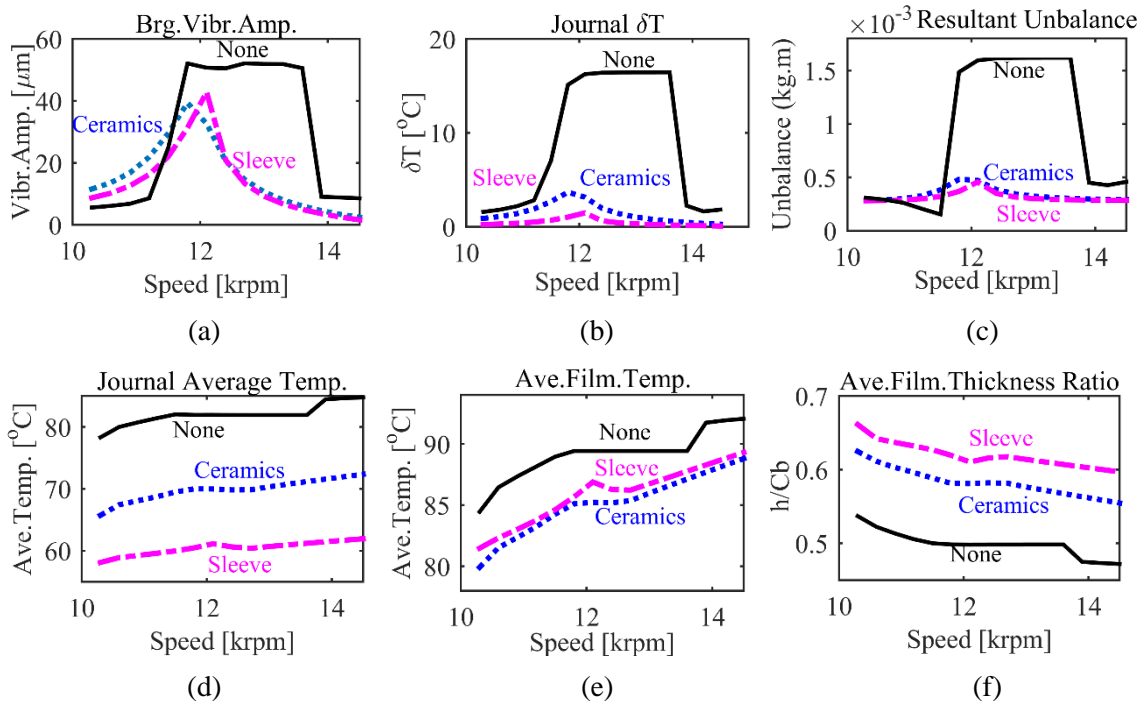
Fig. 5-17 Steady state analysis on the NDE journal with the heat barrier sleeve and ceramic isolation.

Compared with the original system without heat flux isolation, both the ceramics and heat barrier sleeve can effectively suppress the ME in Fig. 5-17: the ISB is narrower with lower vibration amplitude; the maximum journal ΔT are reduced to $3.6^{o}C$ by ceramics and $1.5^{o}C$ by the air sleeve; the resultant unbalance curve (vector summing both the mechanical and thermal imbalance) are flattened. Due to the isolation of heat flux into the journal, the average journal temperature with ceramic isolation is more than $10^{o}C$ lower than the no isolation case, and the sleeve with air gap achieves a better cooling effect than the ceramics by reducing the journal temperature further down to $60^{o}C$. A cooler journal will yield less thermal expansion and larger bearing clearance, and therefore, the film temperature will be reduced due to less viscous shearing. Note that the heat barrier sleeve outperforms the ceramics in cooling the journal and increasing the film thickness due to the lower air thermal conductivity compared with ceramics in this paper. However, the ceramic sleeve can be simpler in design and thus easier for implementation.

6 EXPERIMENT OF JOURNAL CIRCUMFERENTIAL TEMPERATURE MEASUREMENT[*]

6.1 Importance of Journal Circumferential Temperature Measurement

The difficulty of measuring temperatures in a high-speed journal has limited the number of experimental ME papers appearing in the literature. Telemetry and slip ring based approaches are required along with a shaft motion measurement and DAQ (Data acquisition) system. Dowson [3] used 12 thermocouples, which were located in four axial journal planes, to measure the temperature variation in both circumferential and axial direction in 1966. The maximum speed was 2000 rpm and the maximum load was 3500 lb in these measurements. The steady journal temperature variation in both directions was quite small and thus the shaft was treated as an isothermal component. The journal was in equilibrium when the measurement was performed, and thus the journal surface experienced similar heat flux and negligible ΔT in the absence of journal whirling motion.

In 1994, de Jongh [12] tested an overhung rotor supported by tilting pad bearings to replicate the thermal instability problem observed in a compressor close to 11500 rpm. Four RTDs (resistance temperature detectors) were equally spaced around the journal circumference. The peak-peak journal ΔT was found to be 2℃ at 10500 rpm and the hot spot lagged the high spot by an estimated 20°. The system became synchronous-unstable

when the rotor was accelerated up to 11500 rpm, with vibration continuously increasing and ΔT growing to as high as $10°C$. In 2015, Panara, et al. [11], installed eight thermocouples equally spaced around the journal circumference and a few millimeters below the journal surface. The peak-peak journal ΔT and phase lag between the high and hot pot were correlated to the vibration data to extract function parameters for linking vibration and temperature. Both the temperature and phase lag were found to vary with rotor speed, viscosity and heat capacity of the lubricant, etc. They compared predictions to theory and found that accurate prediction of phase lag between the hot spot and high spot was much more difficult than journal ΔT.

Incorrect prediction of the hot spot position and/or the journal ΔT can deteriorate the prediction accuracy of the ME instability onset speed, considering that both parameters directly determine the shaft thermal bow magnitude and direction [67]. It was believed that a finer grid of measured temperatures was needed to more accurately benchmark journal temperature prediction tools. Thus, to improve the spatial resolution of the measured journal temperature distribution, the work in this paper utilized 20 RTDs installed around the journal circumference to give the most detailed measurement of the journal ΔT and phase lag between the high and hot spot, to date. The objective of the experiment was solely to measure temperature distribution of a journal in a spinning and synchronous whirling condition, as opposed to observing an actual ME instability. The test schedule varied operating conditions including rotor speed, supply oil temperature and bearing static eccentricity. A simulation model was developed to compare predictions with

measurements and utilized a 3D FEM (finite element method) based approach with both bearing and shaft asymmetric temperature variation and thermal expansion.

6.2 Test Rig Description

The primary objective of the test rig is to perform a comprehensive measurement of the journal circumferential temperature distribution inside a tilting pad journal bearing (TPJB) at various operating conditions including: speed up to 5500 rpm, supply oil temperature at 28°C and 41°C, and bearing static eccentricity at 0 and 32% C_b. A photo and drawing of the test rig is shown in Fig. 6-1, and the instrumented test shaft and tilt pad journal bearing TPJB are shown in Fig. 6-2. The five-pad TPJB with L/D = 1 and $C_b=$ 0.0055 inch (0.14 mm) is installed between two ball bearings. The single shaft has multiple steps and a journal instrumented with 20 RTDs equally spaced around its circumference and attached 1 mm beneath the surface. The RTD leads are routed along the hollow shaft and nearly fill the cylindrical space. The journal is intentionally machined to be eccentric with a radial offset of r=0.0027 inch (0.0686 mm) with respect to the global centerline of the shaft determined by the ball bearings and shown in the axial cross-section view in Fig. 6-1.

The high radial stiffness (1.6E8 N/m per bearing) of the support ball bearings nearly produces a "pinned" condition causing the eccentric journal to execute a synchronous, circular orbit of radius r within the TPJB. This emulates the synchronous whirl that occurs in an operating machine under the influence of mass imbalance, and is the known source of asymmetric heating and consequent thermal bow in the Morton effect.

The tolerance limitations on machining the eccentric journal results in an orbit radius r that exceeds the typical values observed in most machinery, so might represent the case of a severe ME event. All RTDs are electrically isolated from the shaft with a thin thickness, highly thermally conductive epoxy and have wire leads that are routed via the hollow shaft to the slip ring at the non-drive end (NDE). The output wires of the slip ring transmit the signals to the data acquisition board over the operating speed (RPM) range. Orthogonally oriented non-contacting eddy current sensors (ECS) are installed at both bearings yielding "X1, Y1, X2 and Y2" relative shaft displacement signals, and a fifth ECS is installed to provide a tachometer (key-phasor) output signal. The high combined stiffness of the ball bearings and their rigid support structures elevate the 1st critical speed above 40,000 rpm, which assures that support motion is minimal at the max operating speed 5,500 rpm of the test rig. The lateral position of the TPJB centerline with respect to the shaft (ball bearings) centerline can be adjusted utilizing jack-bolt set-screws that translate the TPJB to achieve the desired static eccentricity and attitude angle. The two tested operating eccentricities are $e_1 = 0, e_2 = 32\%C_b$, and the corresponding attitude angle is held close to zero, to simulate typical TPJB operation.
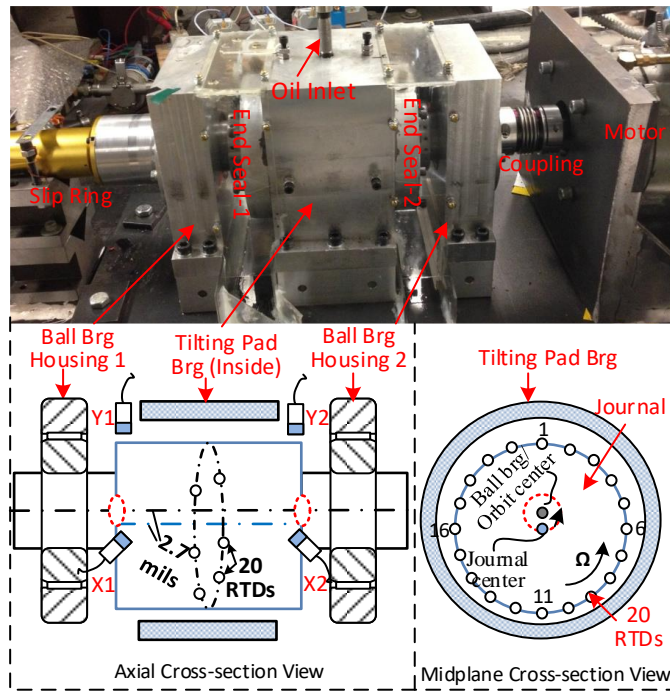
Fig. 6-1 Photo and diagram showing the key components of the TPJB-ME test rig.
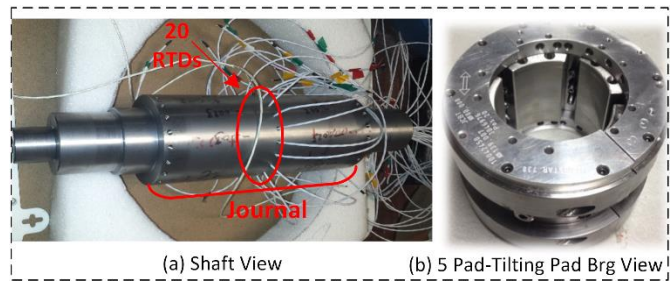
Fig. 6-2 (a) Shaft with eccentric journal and 20 internally routed RTDs and (b) tested TPJB.
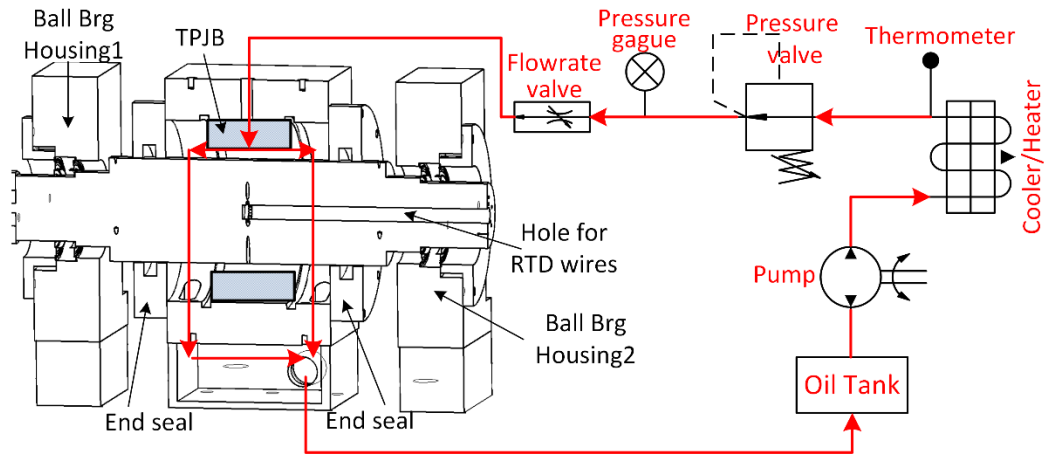
Fig. 6-3 Key components of the TPJB-ME test rig hydraulic system.

Table 6-1 Parameter values of the test rig

Lubricant parameters		Bearing parameters	
Viscosity at 40 ℃ [Ns/m^2]	0.044	Load type	Load on Pad
Viscosity coefficients [1/℃]	0.04218	No. pads	5
Supply temperature [℃]	$28 \pm 3(cool),$ $41 \pm 3(hot)$	Radius of shaft [m]	0.040
Flow rate [L/min]	17(≤3 krpm), 21(>3 krpm)	Radial bearing clearance [m]	1.40×10^{-4}
Reference temperature [℃]	40	Pad Preload	0.42
Shaft Parameters		Bearing length[m]	0.08
Shaft total length [m]	0.40	Pad arc length[degree]	56
Shaft total mass [kg]	9.25	Pivot	Rocker
Journal radius [m]	0.040	Pivot offset	50%
Journal length [m]	0.21	Tested eccentricity	$0, 32\%C_b$
Journal centerline offset [m]	6.86×10^{-5}	Tested attitude angle	$0°, 5.8°$
Thermal expansion coeff.[1/℃]	1.2×10^{-5}	Speed [rpm]	Up to 5500
Reference temperature [℃]	25	Thermal expansion coeff. [1/℃]	1.2×10^{-5}
Ball bearing stiffness [N/m]	1.6E8	Reference Temperature [℃]	25

135

Fig. 6-3 illustrates key components in the TPJB-ME test rig's hydraulic system. The TPJB's VG 46 viscosity grade lubricant is routed from the supply tank through the pump and heater and into the oil inlet port on the top of the TPJB housing. The TPJB has a directed lubrication nozzle system that sprays oil into the gaps at the leading edges of all pads. Two end seals restrict oil leakage from the bearing house to atmosphere, assuring that nearly all of the oil returns to the oil supply tank. The "oil supply" temperature of the lubricant entering the TPJB is controlled by an inline heater/cooler system, and the shaft speed is controlled with a VFD 25 hp electric motor.

The bearing clearance, eccentricity, rotor speed, oil flow rate and supply temperature are selected at the design stage to prevent overheating, oil starvation and rubbing between the bearing and journal. Table 6-1 provides a summary of the parameter values for the test rig.

6.3   Measured Shaft Temperature Distribution

The RTD accuracy is 0.15℃ and the thermal response time is less than 1 second. All RTDs were calibrated at room temperature before each experiment to eliminate static output (drift) error. The oil supply temperature was set at 28 ℃ or 41℃ for cool and hot oil testing, respectively. Real time recording of supply temperature indicated fluctuations within ± 3℃ during the test sequence. All test conditions were repeated at least three times and satisfactory repeatability was found with the journal ΔT variation typically within 0.2℃. All RTDs were recorded at a sampling frequency of 0.6 Hz over a recording duration of 8 minutes at each speed to ensure convergence of measurements to their steady

state values. The samples within the last 10 seconds were averaged to represent the steady rotor temperature. Two bearing static eccentricities were tested with $e_1 = 0$, and $e_2 = 0.32C_b$ and with the other variable values provided in Table 6-1. Fig. 6-4 shows the cross-section of the journal in the bearing for the two static eccentricity cases.

Note: Exaggerated size. e1,e2 are distance between O$_{TPJB}$ and O$_{orbit}$. h is film thickness

(a) $e1$=0   (b) $e2$=0.32Cb
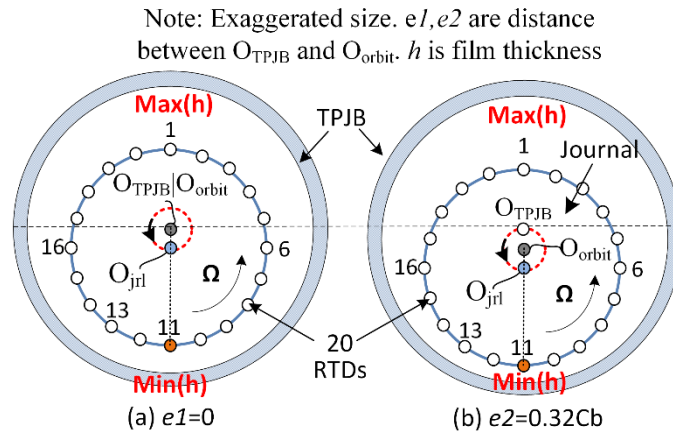
Fig. 6-4 Cross-sectional view for both static eccentricities, $e_1 = 0$ and $e_2 = 0.32C_b$.

6.3.1 Cool Supply Oil Test

The journal orbit center O$_{orbit}$ exactly coincides with the TPJB center O$_{TPJB}$ when $e_1 = 0$, as shown in Fig. 6-4(a). RTD #11 experiences the minimum film thickness continuously during each synchronous whirl orbit and thus observes more viscous shearing than the other 19 sensors. In practice, the TPJB always operates with a static eccentricity to support the bearing loads, such as rotor weight and gear force. The operating eccentricity of the TPJB also changes with load, speed, bearing configuration, etc., and can be as high as 80% C_b or even larger, especially for low speed and heavy

loading conditions. The test eccentricity of $e_2 = 32\% C_b$ was chosen to simulate a low to medium static bearing loading in practice and to avoid rubbing between the journal and the TPJB while considering the dynamic eccentricity caused by the eccentrically machined journal.

The journal orbit center O_{orbit} is displaced away from O_{TPJB} when the bearing is operating with a static eccentricity. In this case RTD #11 experiences a fluctuating film thickness during its synchronous orbit, which might lead one to expect a reduction in the journal circumferential ΔT compared with the centered case [31]. However, the film thickness at RTD #11 is smaller than the zero-eccentricity case when the journal center is at the lowest point in its orbit, leading one to expect a boost in the journal ΔT. Test results with the two bearing eccentricities $e_1 = 0$ and $e_2 = 0.32 C_b$, and the lower supply oil temperature $28 \pm 3°C$ are presented in Fig. 6-5. $\max(T)$ is the maximum journal temperature relative to the supply oil temperature, and $\max(\Delta T)$ is the peak-peak temperature difference among all 20 RTDs in this figure. Note that all measurements in this paper are presented relative to the supply oil temperature, i.e., $T=0$ corresponds to the given supply oil temperature.

The journal orbit size and shape may vary significantly with rotor speed, mechanical imbalance, bearing loads, etc., in an actual operating machine, making it difficult to conduct a single variable sensitivity study related to the ME. In contrast, the test rig facilitates ME sensitivity studies by maintaining an invariant journal orbit determined solely by the machined eccentricity of the journal centerline relative to the shaft, which is supported by relatively rigid ball bearings. This enables the study of static

eccentricity effects on ME while maintaining an invariant synchronous whirl orbit. Fig. 6-5(a) shows that both max(T) and max(ΔT) increase almost linearly with speed, and for every 1 krpm increment, the max(T) and max(ΔT) grow by approximately 3.8℃ and 0.83℃ respectively. Changing the bearing static eccentricity from 0 to $0.32C_b$ does not significantly affect max(T) but increases max(ΔT) by 0.5℃ throughout the test speed range. The larger max(ΔT) indicates that the smaller minimum film thickness experienced by the high spot for the statically eccentric case (journal at the bottom of the orbit in Fig. 6-4(b)) intensifies the viscous shearing and journal asymmetric heating compared with the zero-eccentricity case, which results in a higher temperature difference around the journal. This trend in the measured max(ΔT) differs from that opined in Kirk [31] that a centered orbit was more prone to the ME than an off-centered orbit. On the other hand the measured trend is somewhat substantiated by Schmied [20], where he mentioned that the ME was also observed in highly loaded bearings with the elliptical, off-centered journal orbits. The measured results indicate that one should not expect that increasing the static eccentricity will always improve suppression of the ME by reducing the journal ΔT. Fig. 6-5(b)-Fig. 6-5(d) illustrate the steady journal temperature distribution at different speeds from all 20 RTDs. The temperature profiles are quite sinusoidal with the sensors close to the high spot, i.e., RTD #11, experiencing higher temperature. Interestingly, the hot spot does not exactly coincide with the high spot, which experiences the minimum film thickness. Instead, the hot spot is close to RTD #13 and lags the high spot by a certain angle which is speed dependent and increases from 20° at 1143 rpm to 40° at 5454 rpm.
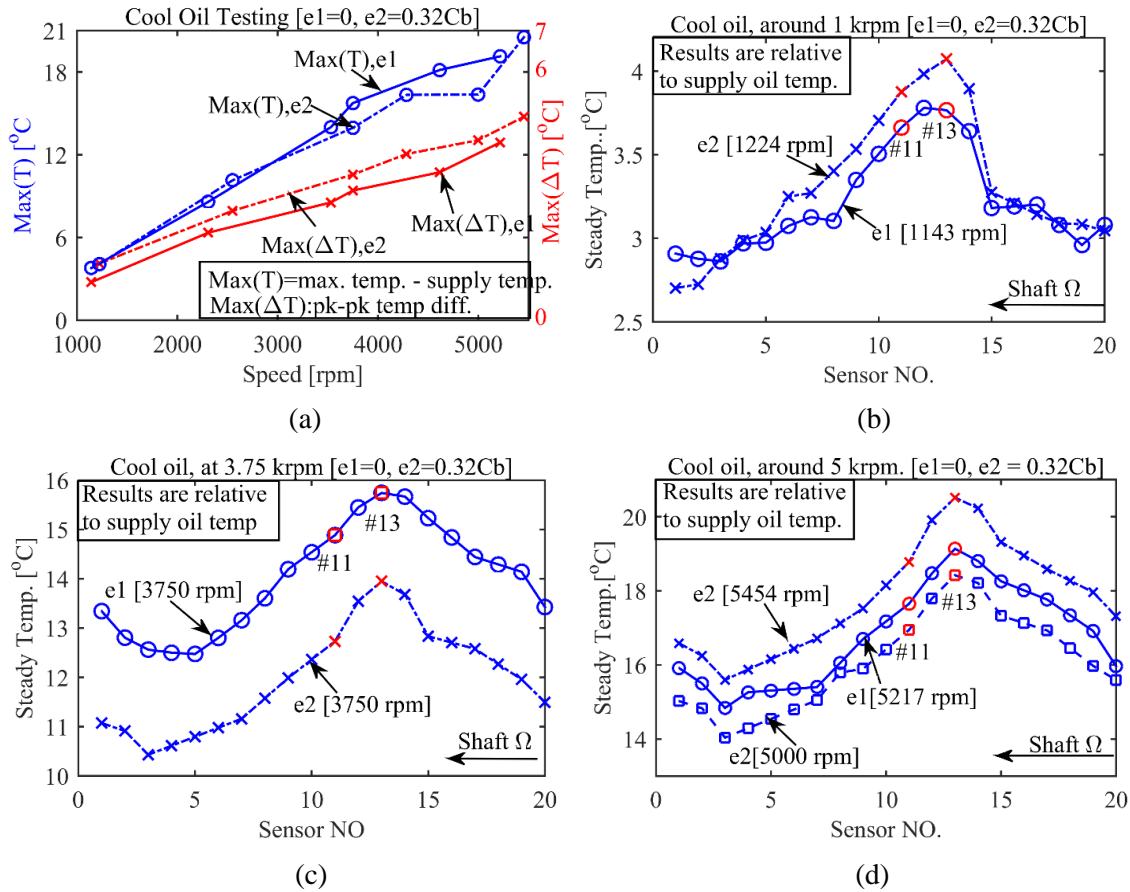
Fig. 6-5 Measured rotor temperature with lower (cool) supply oil temperature and two static eccentricities. (a) Maximum rotor temperature and peak-peak temperature difference, (b) rotor temperature profiles at approximately 1 krpm, (c) 3.75 krpm, and (d) 5 krpm.

A simple linear interpolation method is employed to approximate the hot spot location, assuming that in most cases the hot spot is close to RTD #13, as depicted in Fig. 6-6(a). The 3 cases that may occur are: (1) the temperature of RTD #12 is lower than RTD #14, i.e., $T_{12} < T_{14}$, then the hot spot will be at the crossing point between #13 and #14 and is located by extending two adjacent sensor readings to locate the crossing point CP. The CP is always greater than T_{13} in the measured data. (2) if $T_{12} = T_{14}$, #13 is the hot

spot; (3) if $T_{12} > T_{14}$, the hot spot will be at the CP between # 12 and # 13. The CP is always greater than T_{13} in the measured data.

The measured phase lag of the hot spot behind the high spot is shown vs. speed in Fig. 6-6(b). Note that at low speed, the phase lag falls below 30° for both eccentricity cases and grows with speed and converges to 40° at 5454 rpm. Predicted phase lag for speeds greater than the measurement limit 5454 rpm indicates a reduced rate of growth of phase lag with speed. The measured phase lag differs from de Jongh's experiment [12], where the journal temperature distribution was estimated using only four sensors and the phase lag ranged from 15° at 4 krpm to 20° at 10.5 krpm. The difference may be due to the fewer number of sensors in de Jongh's experiment or due to the phase lag being sensitive to running speed and bearing configuration, which would dispel the notion of a nearly universal phase lag for the Morton Effect. The current measurements are more consistent with Gomiciaga and Keogh's prediction [13], which was about 35° using a CFD (computational fluid dynamics) model.

(a)   (b)
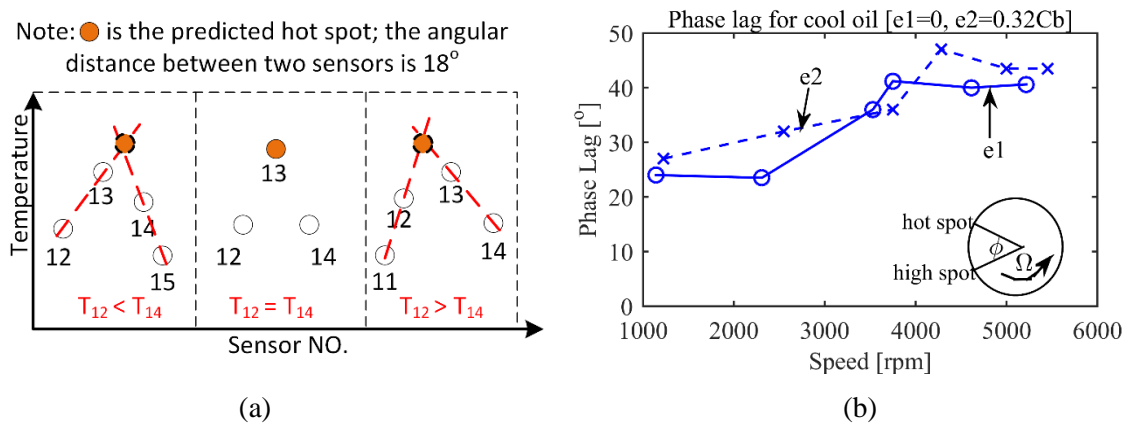
Fig. 6-6 (a) Linear interpolation to estimate hot spot location and (b) measured phase lag between the high spot and hot spot with cool supply oil and two eccentricities.

141

6.3.2 Hot Supply Oil Test

The supply oil temperature was increased from 28℃ to 41℃ and the related measurements are presented in Fig. 6-7. In Fig. 6-7(a) both the journal $\max(T)$ and $\max(\Delta T)$ increase monotonically with speed, which is similar to the cool oil case but is lower in magnitude. The eccentricity's influence on $\max(T)$ is more evident than the cool oil case, and changing the bearing eccentricity from 0 to $0.32C_b$ increases the journal $\max(T)$ by 2℃ on average. The journal $\max(\Delta T)$ with $e_2 = 0.32C_b$ is higher than $e_1 = 0$ by 0.5℃, which is quite similar to the cool oil testing, indicating that increasing the bearing operating eccentricity may not mitigate the ME. Fig. 6-7(b) shows that the phase lag between the high and hot spot grows from below 30° at low speed to 40° at high speed and almost levels off afterwards, which is also similar to the cold oil case. Fig. 6-7(c) to Fig. 6-7(e) illustrate the circumferential journal temperature distribution vs. speed, indicating that the hot spot near RTD #13 clearly lags the high spot RTD #11 which experiences the minimum film thickness. The cold spot is close to RTD #3, which is out of phase with the hot spot, indicating that the temperature profile is nearly sinusoidal.
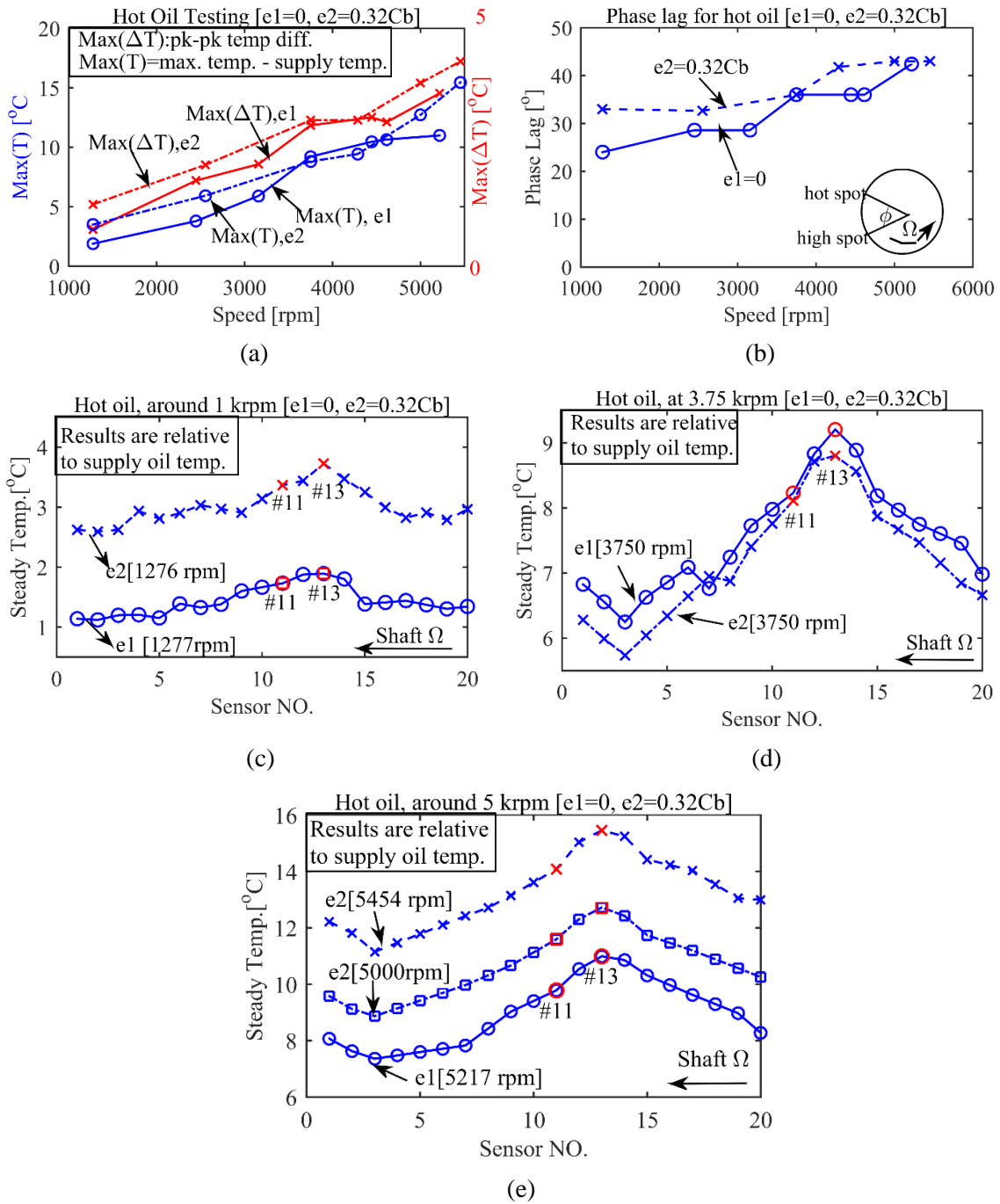
Fig. 6-7 Measured rotor temperature with hot supply oil and two eccentricities. (a) Maximum journal temperature and peak-peak temperature difference, (b) phase lag between high spot and hot spot (c) steady rotor temperature profile around 1 krpm, (d) 3.75 krpm, and (e) 5 krpm.

The max(T) and max(ΔT) for the hot oil testing are both lower than the cold oil case, and the ratio of the hot oil divided by the cool oil measurements is shown in Fig. 6-8. Note that the max(T) is presented relative to the supply oil temperature, and thus smaller max(T) for the hot oil does not indicate that the absolute temperature is lower. As shown in Fig. 6-8(a) the journal max(T) with hot oil decreases for both eccentricity cases compared with the cool oil testing. The reduction percentage is 20%~40% for $e_2 = 0.32C_b$ and 40%~60% for $e_1 = 0$, which is related to the reduction of lubricant viscosity, which drops by 43% compared to the cool oil at 28°C, as shown in Fig. 6-8(b). The reduction of the journal max(ΔT) is less significant and stays around 20% for all speeds as shown in Fig. 6-8(a). The viscosity-temperature profile is measured and curve fitted by an exponential function in Fig. 6-8(b), and the parameters are included in Table 6-1 and employed in the simulations in Section 7.
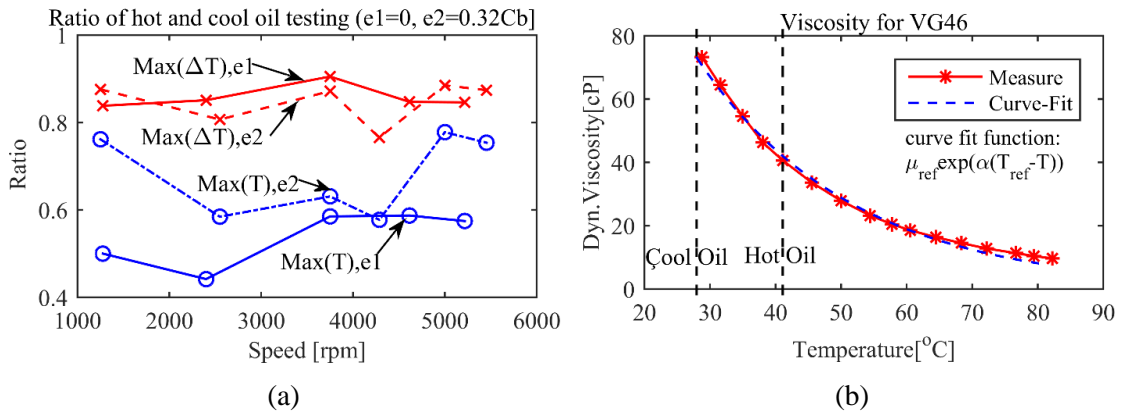
Fig. 6-8 (a) Ratio between hot and cool oil testing (b) Oil viscosity vs. temperature.

144

7 PREDICTION OF EXPERIMENT WITH HIGH FIDELITY

AND SIMPLIFIED APPROACH[*]

Accurate prediction of the journal temperature distribution, especially the ΔT (journal temperature difference) and the hot spot location (the hot spot is the journal circumferential position with the highest temperature), is critical in determining the potential for ME induced instability, and for its mitigation in existing machines. The journal ΔT helps to evaluate the magnitude of the rotor thermal bow, while the phase lag between the hot spot and high spot determines the thermal bow direction (high spot is the rotor angular position which experiences the minimum time-averaged film thickness). Morton effect (ME) predictions generally fall into two categories (1) the high-fidelity approach [39, 40, 42, 43], which numerically integrates the multi-physics problem of rotordynamics, thermodynamics, fluid mechanics and deformation in the time domain to predict the transient rotor vibration and temperature, and (2) the simplified approach [18, 38], which adopts an iterative linearized "influence coefficient" assumption between vibration, journal ΔT and thermal imbalance. The latter approach ignores the actual continuous transient behavior and instead idealizes the ME as being either synchronous stable or unstable, judged by eigenvalues of a sequential steady state model. This approach approximates the ME as a finite sequence of steady state problems instead of a transient phenomenon. Temperature distributions obtained in this approach are evaluated at a

sequence of fixed journal positions and thus ignore the effects of journal velocity on temperature. The simplified approach also neglects transient film temperature effects by only solving the steady state form of the energy equation. This assumes that temperatures in the lubricant follow their sources (heat generated from viscous shear) instantaneously, neglecting the time required for heating the lubricant after for example a maximum shear (minimum film thickness) event. Thus, the hot spot and high spot are always coincident in the steady state energy equation solution approach. The high-fidelity approach seeks to improve the prediction accuracy and treats the actual (continuous) transient response during the ME. The influence of thermal boundary conditions, bearing clearance, bearing pad and pivot flexibility, etc., are also considered due to the ME's sensitivity to these factors. As expected the execution time of the simplified approach is much faster than the high-fidelity approach.

7.1   Introduction of the High Fidelity Approach

7.1.1   Dynamic Model

The ME is commonly observed in overhung rotating machinery, where rotor thermal bending at a journal may add significant thermally induced, effective mass imbalance at the overhung node. The aim of the test rig is limited to investigating the asymmetric journal temperature distribution as opposed to reproducing a full blown ME occurrence. Thus, the rig uses a short rigid, synchronously whirling rotor without an overhung mass. The ball bearings react the rotor induced loading while restricting its lateral motion, and thus the journal orbit remains nearly invariant under all operating

146

conditions. The mechanical imbalance $\overline{me}$ due to the intentionally machined eccentric journal and the hydrodynamic forces at the TPJB location both effect the rotor response in the rig. The rotor is connected to the drive motor with a very flexible coupling that has negligible influence on the rotor motion or bearing forces. The rotor equations of motion are given in Eq. 7-1, where m is the rotor mass, k is the ball bearing stiffness, w is the rotor weight and F_x and F_y are the hydrodynamic forces from the TPJB. Note that x and y locate the shaft geometrical center, i.e., the center of the journal orbit, which differs from the journal center by the machined eccentricity r=0.0027 inch.

$$\begin{bmatrix} m & 0 \\ 0 & m \end{bmatrix} \begin{bmatrix} \ddot{x} \\ \ddot{y} \end{bmatrix} + \begin{bmatrix} 2k & 0 \\ 0 & 2k \end{bmatrix} \begin{bmatrix} x \\ y \end{bmatrix} = \overline{me}\omega^2 \begin{bmatrix} cos(\omega t) \\ sin(\omega t) \end{bmatrix} + \begin{bmatrix} 0 \\ -w \end{bmatrix} + \begin{bmatrix} F_x \\ F_y \end{bmatrix} \qquad \textit{Eq. 7-1}$$

The test bearing is a five-pad load-on-pad TPJB with a cylindrical pivot, 50% offset, and pad thickness of 11 mm. As shown in Fig. 7-1, the simulation model permits tilt δ_{tilt} and translation y_{pad} of each pad about its pivot, and the individual pivot deformation and stiffness are predicted based on Hertzian contact theory [59]. Pad flexibility [43] was initially included in the model using 3D FEM, however the results were quite similar to the rigid pad model indicating that the rigid pad model was sufficiently accurate for all ensuing simulations. The governing equations for the ith rigid pad shown in Fig. 7-1 are given in Eq. 7-2, where m_{pad} and I_{Pad} are the pad mass and moment of inertia, p_i and f_i represent the nodal hydrodynamic and viscous forces, p_{iy}, f_{iy} are the y components of p_i, f_i, and M_{pi}, M_{fi} are the moments about the pivot P caused by nodal forces p_i and f_i.

$$\begin{cases} m_{pad}\ddot{y}_{pad} = -k_{pvt}y_{pad} + \Sigma p_{iy} + \Sigma f_{iy} \\ I_{Pad}\ddot{\delta}_{tilt} = \Sigma M_{pi} + \Sigma M_{fi} \end{cases}$$

$Eq.\ 7\text{-}2$
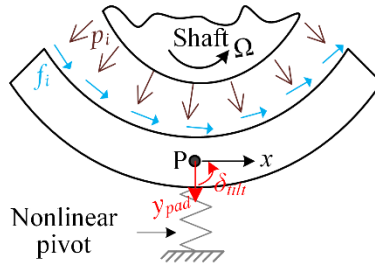
Fig. 7-1 Journal and rigid pad force diagram.

7.1.2 Thermal Model

The accurate prediction of rotor and bearing temperatures are important from a rotordynamic perspective for at least two reasons. First, the temperature rise may cause thermal expansion, reducing the operating bearing clearance which affects the bearing stiffness and damping. Secondly, in overhung machines, the ΔT across the journal circumference may bend the shaft and cause thermal imbalance and the ME. The test rig is designed to study the source of these responses, namely the asymmetric temperatures induced on the journal by rotor spinning and synchronous whirling. The 3D heat conduction equation applies to modeling both the rotor and bearing pads and is solved with the FEM using 3D, 8-node iso-parametric solid elements. The conduction equation is

$$\frac{\partial^2 T}{\partial x^2} + \frac{\partial^2 T}{\partial y^2} + \frac{\partial^2 T}{\partial z^2} = \frac{\rho c}{k}\frac{\partial T}{\partial t}$$

$Eq.\ 7\text{-}3$

, where k is heat conductivity, ρ is density, and c is the heat capacity. The lubricant and rotor & pad Eq. 7-3 thermal problems are solved as a coupled system with both internal and external boundary conditions. The internal boundary conditions include continuity of temperature and heat flux on the lubricant\journal and lubricant\pad surfaces. The lubricant/journal boundary condition is imposed considering that the shaft is spinning with speed ω, so θ in the rotor rotational frame corresponds to $(\theta + \omega t)$ in the lubricant fixed frame. The shaft and pad surfaces exposed to air have a heat convection boundary condition $q = \bar{h}(T - T^{\infty})$, where q is the heat flux, T^{∞} is the ambient temperature, and $\bar{h}$ is the heat convection coefficient. T^{∞} is set to $30°C$ for all simulations and $\bar{h}$ is set to the constant value $10 \text{ W}/m^2°C$. The latter was justified by varying $\bar{h}$ and finding that the resulting changes in the predicted rotor temperature varied by less than $1°C$. Fig. 7-2 illustrates the thermal boundary conditions and the cross-section temperature distribution for identifying the hot spot position. The thermal and vibrations problems are solved in a staggered manner for computational efficiency [42], so that the thermal solution is updated after the vibrations have reached steady state, and vice versa.
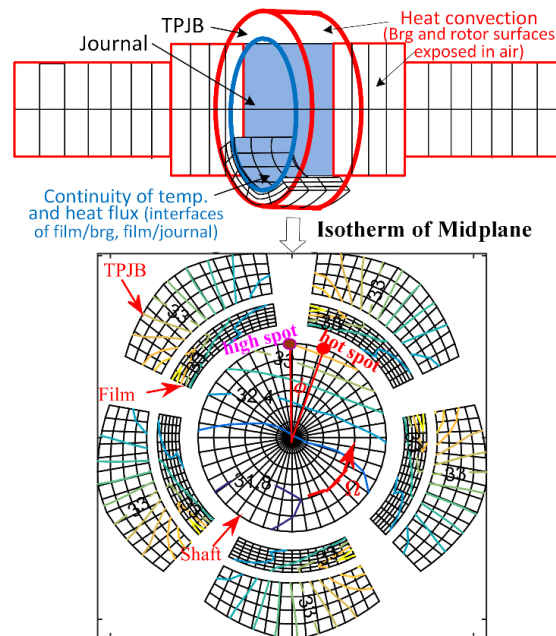
Fig. 7-2 Boundary conditions for the coupled journal/shaft/film/pad thermal model.

The thermally induced deformation of the shaft, journal and pads is modeled with a 3D solid, structural FEM model, sharing the same nodes as the 3D solid, thermal FEM model. The temperature solver calculates all nodal temperatures of the rotor and bearing forming the thermal load vector, which is applied to calculate thermally induced deformations. The hot bearing clearance and the film thickness distributions are then updated using these deformations. The test rig is designed to only measure the asymmetric journal temperature distribution and lacks an overhung mass which is needed for the synchronous instability response of the ME. For the more general case in modeling actual overhung machines, the shaft thermal bow also needs to be calculated and fed back to the rotordynamic solver to predict the transient dynamics of the rotor and bearing in the next integration cycle. In this case the transient numerical integration of the temperature and

150

dynamic solvers are coupled and successively solved in the time domain until convergence. The rotor speed is set to a constant value for predicting the steady state rotor and bearing temperatures and dynamics. Details of the ME simulation algorithm can be found in [43].

7.2 Simulation Results Using a High-Fidelity, Transient Modeling Approach

7.2.1 Comparison of Simulation and Experimental Results

Fig. 7-3 shows both prediction (dashed) and test (solid) temperatures. The average difference for $\max(T)$ between prediction and experiment over the speed range and with the 2 bearing eccentricities and 2 oil supply temperatures is about $1.9°C$. Similarly, the difference for $\max(\Delta T)$ is $0.6°C$, indicating that the prediction accuracy is quite satisfactory. The simulation for $e_1 = 0$ with both cool and hot supply oil in Fig. 7-3(b) over predicts $\max(\Delta T)$, while the prediction for $e_2 = 0.32C_b$ has better agreement with the test measurements. The phase lag between the journal high and hot spots shown in Fig. 7-3(c) indicates a generally lower prediction value relative to the measurement. The current test rig, by far has the most sensors for measuring the ME in the public domain, and yet still only has a resolution of $18°$, i.e., $\frac{360°}{\text{Sensor\_NO}}$. The trend of the measured and predicted phase lag vs. speed is in general agreement and the difference between the measured and predicted values typically falls within 10 degrees and even less for the centered journal case. Given the coarse resolution of the measurements this is considered a reasonable difference supporting the accuracy of the predictions. Simulations performed at speeds above the max test speed of 5454 rpm, which resulted from power and oil flow limits, indicate that the phase lag converges to about $40°$ as speed is increased.

151
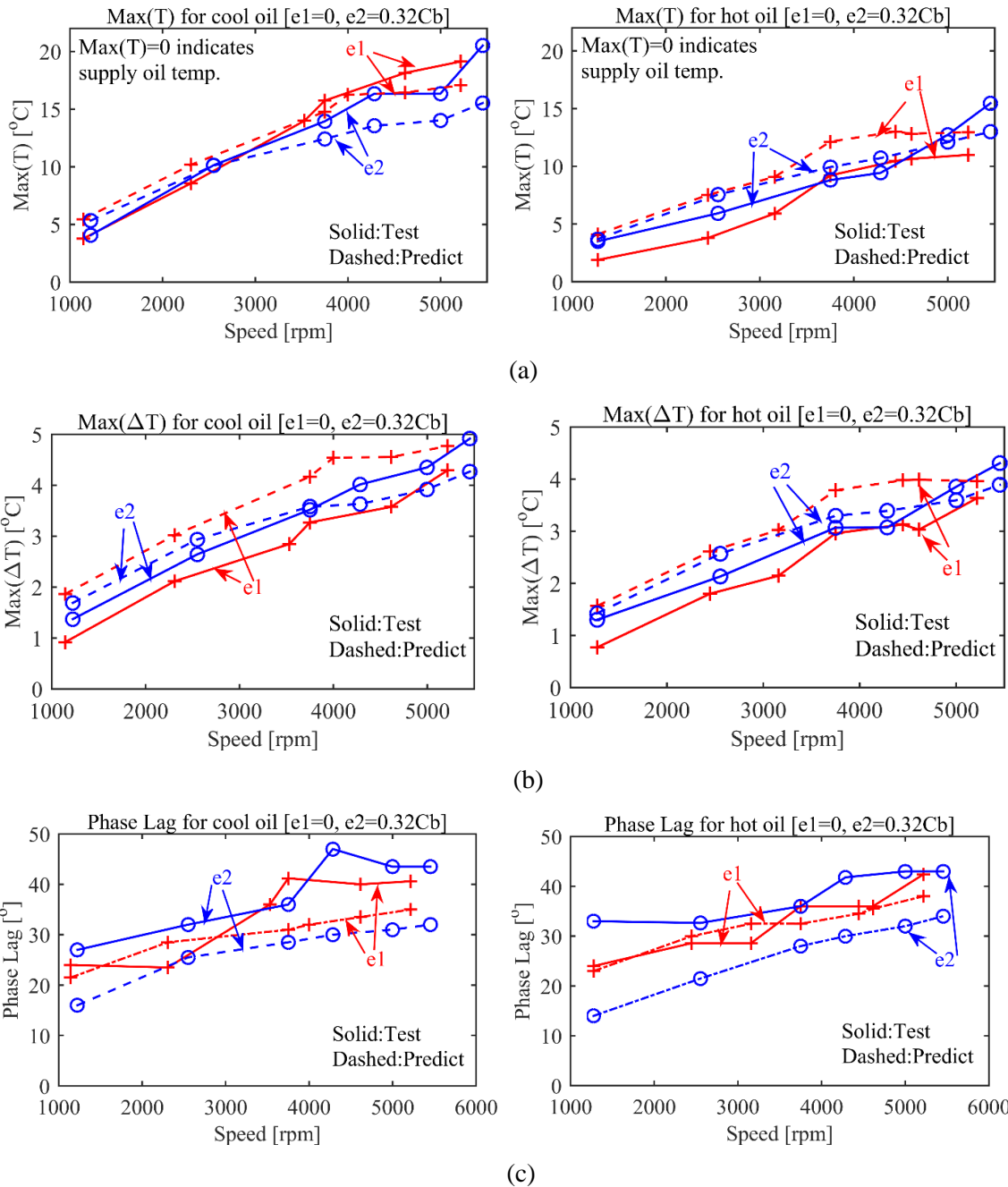
Fig. 7-3 Experimental and predicted journal temperature for cool/hot oil cases. (a) maximum temperature (b) peak-peak temperature difference (c) phase lag between high and hot spot.

152

Some possible reasons for the differences between prediction and experiment are (1) spatial resolution of the measurement, (2) the measurement tolerance of the bearing clearance and ball bearing stiffness, and (3) the simplified mixing coefficient model. Eighty percent of the inlet flow for each pad is assumed to be carried over from the previous pad's trailing edge and mixing together with 20% fresh supply oil, for all predictions. The mixing coefficient is estimated based on the measured flow rate and journal temperature. The actual mixing process is quite complex and is reported to change with rotor speed and bearing eccentricity.

7.2.2   Parametric Studies of Bearing Clearance and Mixing Coefficient

Bearing radial clearance C_b has been reported to affect the ME instability by changing the lubricant viscous shear stresses. In 1998, de Jongh [16] increased the C_b from 0.19% to 0.22% (ratio defined as C_b/R_{brg}) to successfully suppress a ME event. In 1997, Corcoran [30] reduced the C_b by 33% and found that although the rotor vibration was suppressed, overheating inside the bearing occurred. The mixing coefficient λ is another important parameter that affects the rotor, bearing and oil temperatures and is likely to change the ME instability [29]. The recent direct bearing lubrication results using spray-bars [68], inlet groove [69], etc., can reduce the carry-over flow ratio and thus cool the rotor and bearing. In this section, three different cases are simulated with (a) 85% C_b with λ=0.8, (b) C_b with λ=0.6 and (c) C_b with λ=0.8, where case c is consistent with the experimental condition and discussed in Section 6. Results are illustrated in Fig. 7-4 for the cold supply oil and zero static eccentricity case. Note that reducing C_b by 15% increases the max(ΔT) by 11%, indicating that the ME might become more severe.

Reducing λ suppresses both the journal $\max(T)$ and $\max(\Delta T)$ although the reduction of $\max(T)$ is more evident in this case. The influence of phase lag between the high spot and hot spot is quite similar to $\max(\Delta T)$, indicating that the hot spot will be closer to the high spot with more direct lubrication and larger C_b.
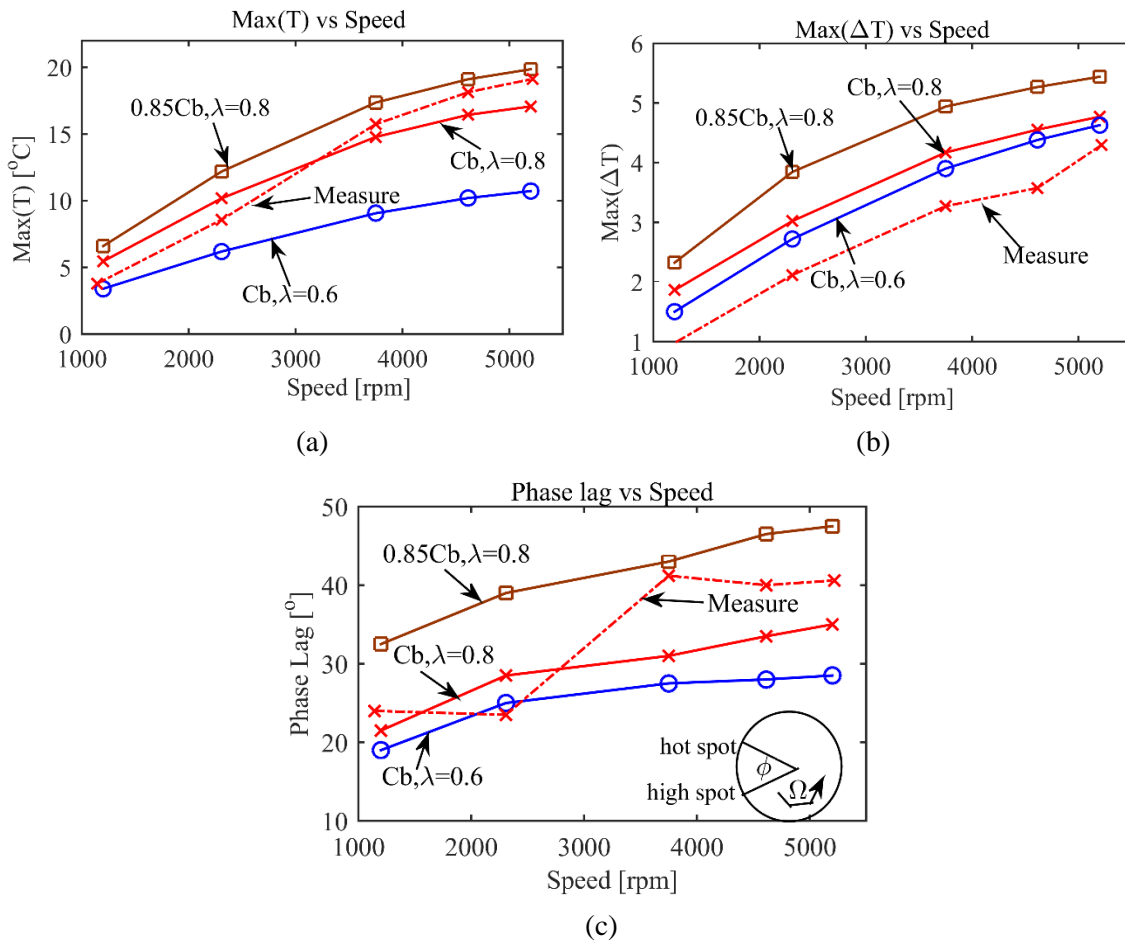
Fig. 7-4 Parametric studies of bearing clearance and mixing coefficient by predicting. (a) maximum journal temperature (b) peak-peak temperature difference on journal circumference (c) phase lag between high and hot spot.

154

7.3 Compare with Simplified Morton Effect Analysis

7.3.1 Version 1 of the Simplified Method

Murphy and Lorenz [38] proposed a faster, yet more approximate ME analysis for estimating rotordynamic, synchronous spiral stability with a frequency domain formulation. The relationships between synchronous vibration, imbalance and journal ΔT were assumed to be linear and expressed in terms of influence coefficients. In 2015, Panara, et al. [11] modified Murphy's method to predict the measured journal ΔT with an additional assumption on pad tilting angle to improve efficiency. This is discussed further in Step III below. The present paper only considers the journal differential temperature ΔT aspect of the overall ME phenomena. Thus, this is the only part of the Murphy and Lorenz' method considered for comparison.

Step I: run conventional bearing design software to get the static eccentricity, pad tilting angles and bearing dynamic coefficients,

Step II: specify a journal orbit and divide it into dozens of discrete points,

Step III: run the same bearing program to obtain the film temperature profile around the journal with its center positioned at each of the orbit points, note that the pad tilting angles can be updated accordingly (Murphy's method [38]), or simply set to be the angles in Step I with the journal positioned at the orbit center (Panara's method [11]).

Step IV: average the temperature profiles from all orbit points to get the asymmetric shaft surface temperature, noting that the shaft also rotates as it whirls around the orbit.

This simplified steady method is intuitive to implement and can be quite fast compared with the current high-fidelity method, which requires the numerical integration for the coupled, transient response of vibration and temperature. Nevertheless, the simplified process is a trade-off between execution speed and accuracy. The present high-fidelity method utilizes mainly 3D FEM component models, having minimal reliance on assumptions, which to some degree compromises the accuracy of the simplified method. These assumptions of the simplified method include;

(1) the journal ΔT is assumed to be proportional to vibration amplitude, which was proven to be inaccurate when the journal orbit size exceeded 20% of bearing clearance by Childs [26],

(2) the actual rotor thermal bow due to the ME is assumed to act as a thermally induced mass imbalance, which neglects the bending moment and has been shown to yield an inaccurate instability onset speed by Tong [42],

(3) most commercial bearing codes assume an insulated rotor surface outside of the journal so that the influence from the rotor thermal boundary conditions is neglected. However, this assumption can compromise the accuracy of the ME prediction which was shown to be quite sensitive to the rotor's heat exchange with its surroundings by Suh [29], and

(4) the ME is assumed to be only rotor speed dependent and not rotor acceleration dependent, which is inconsistent with several case studies where for instance de Jongh mentioned that any speed increase of 1000 rpm within 10 seconds directly triggered the

instability [16], however, in [12] for another compressor, he found that by quickly raising the rotor speed, it was possible to run through the unstable speed range.

The most difficult yet important step in the simplified method is the prediction of journal ΔT, where both the ΔT magnitude and the hot spot position (phase lag relative to the high spot) are important. An upgraded Murphy [38] ME analysis is developed here in order to improve the prediction of the journal ΔT. The framework of the Murphy approach is retained yet modifications are adopted for accuracy improvement. The upgraded approach is to some extent use of a higher fidelity modeling code in Step I and III but also employs a time saving assumption related to steady state tilt angles and pivot deflections.

The results from the upgraded simplified approaches are compared with the high fidelity approach in the results section. The (Version 1) upgraded Murphy method has the following features:

(1) utilize a 3D steady state energy equation to account for the film temperature variation in the axial direction,

(2) solve for the 3D steady state rotor and bearing temperature distribution with FEM including heat convection from the rotor external to the bearing.

(3) include bearing and rotor thermal expansion, which is used to update the hot bearing clearance, and

(4) include pivot flexibility using Hertzian contact theory [59] to calculate the nonlinear pivot deflection.

(5) the pad tilt angles and pivot displacements can be updated according to the journal orbit position (Murphy's method), or simply set to be the steady angles and displacements calculated with the journal fixed at the orbit center (Panara's method).

The predicted journal $\max(\Delta T)$ for various static eccentricities and supply oil temperature is shown in Fig. 7-5 The phase lag prediction is not shown because the simplified approach neglects all transient process and thus always predicts zero phase lag, i.e., the hot spot coincides with the high spot. Murphy's approach [38], uses a constant 20° phase lag between the hot spot and the high spot in a case study but also points out that the angle could be between 0° and 60°. Fig. 7-5 compares the test measurements of journal $\max(\Delta T)$ with predictions from the "Transient" (high fidelity transient based), "Murphy*" and "Panara*" methods. The Murphy method updates the pad angles at each orbit point and the Panara approach uses the pad angles that occur at the orbit center, for all orbit positions. It should be noted that the simplified approach results are obtained using a high-fidelity model including 3D thermal and deformation models and convective heat transfer on the shaft segments adjacent to the bearing. Most commercial codes utilize much simpler 2D or even 1D thermal models and neglect thermal and centrifugally induced deformations. Thus, we have implemented the simplified method with arguably the best available steady state model, for the sake of a fair comparison. The simplified method predicts relatively accurate journal $\max(\Delta T)$ at low speed. However, when the speed increases, both simplified methods "Murphy*" and "Panara*" deviate from the high-fidelity method and overpredicts the $\max(\Delta T)$ by almost 2℃ at 5454 rpm, while the high-fidelity method shows very good agreement with the experimental measurements.

158

The "Murphy*" method has a higher accuracy than the "Panara*" method because the former updates the pad tilt angles and pivot displacements at each point on the journal orbit, making the film thickness and temperature predictions more accurate. The above observations are based on the experimental test configuration, which has a relatively larger bearing clearance compared with industry practice due to machining limitations of the eccentric journal. A second comparison among the three prediction methods, without test data, is presented in Section 7.3.2 utilizing a bearing clearance that is more representative of industrial practice.
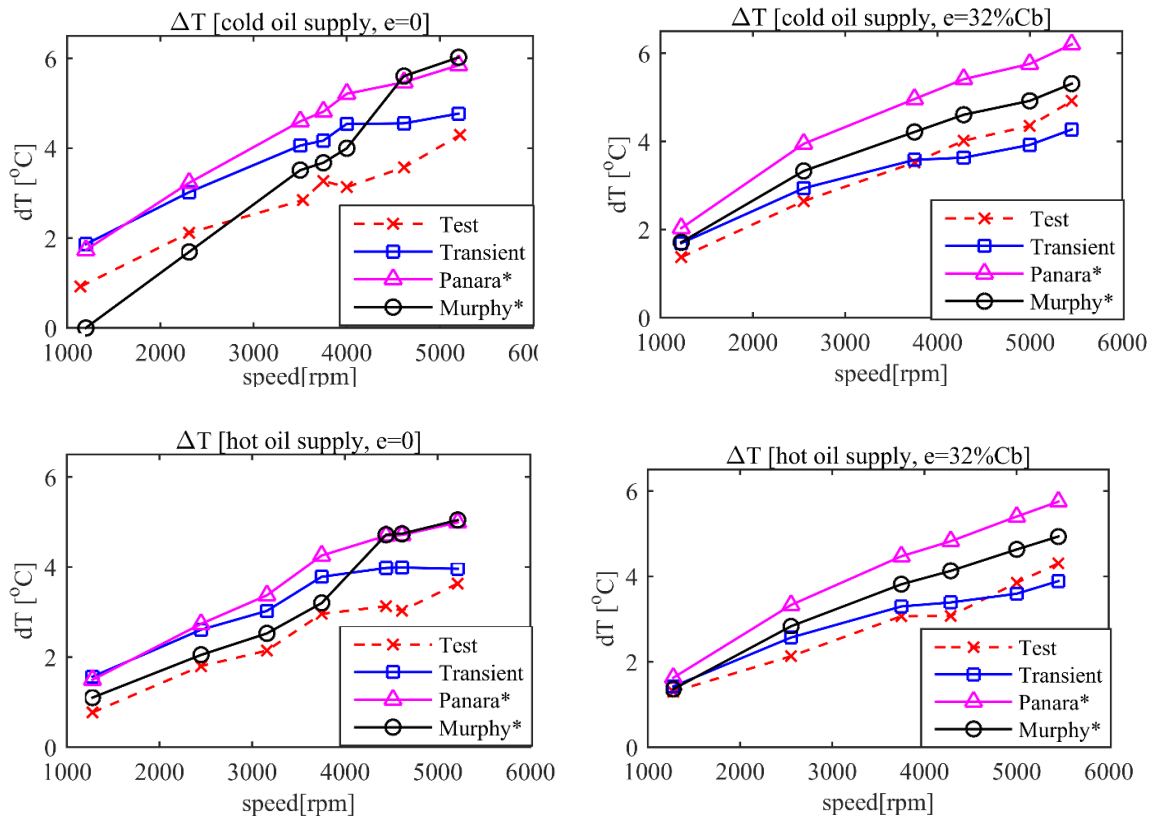
Fig. 7-5 Predictions of journal ΔT by the high-fidelity and simplified analysis.

159

7.3.2 Version 2 of the Simplified Method

The following assumptions contribute to the lower accuracy observed in the simplified approach results:

(1) In the "Panara*" method the same tilt angles calculated with the journal at O_{orbit} are imposed on the bearing pads when the journal is displaced at all points on the synchronous whirl orbit in Fig. 7-6.

(2) The shaft whirling velocity v along the orbit creates an additional source term in the Reynolds equation which is neglected in the steady state solution employed in the simplified approach. This influences the predictions of local pressures, velocities and temperatures, and also pad tilt angles and film thickness.
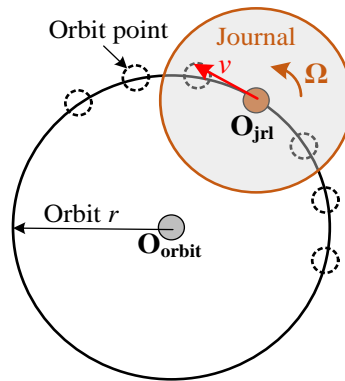
Fig. 7-6 Journal center whirling along an orbit with velocity v.

A further refined variation of the Murphy simplified approach is proposed to provide increased accuracy while still requiring significantly less computational time relative to the high fidelity transient approach.

160

Simplified approach–Version 2 differs from Version 1 in calculating updated pad tilt angles at each point along the orbit (i.e., abandon assumption 1), and including effects of the whirl velocity v in the Reynolds equation (i.e., abandon assumption 2). These alterations would most likely require minor code changes by a developer if a commercial bearing modeling code is employed. The Version 1 and Version 2 simplified method results are compared to each other and to the high fidelity transient method results below. A smaller clearance is employed in the comparison to be more consistent with industrial practice. The TPJB clearance is reduced to 0.003 inch (0.0762 mm, $\frac{C_b}{R_{shaft}} = 0.19\%$) with a preload of 0.3, and the journal orbit radius is reduced to 5E-4 inch (0.0127 mm). Fig. 7-7 shows the predicted journal $\max(\Delta T)$ for the cool supply oil and two eccentricity cases, i.e., zero and $17\% C_b$. The predictions are performed by the two simplified methods and the transient high-fidelity method, where "Murphy*" and "Murphy**" are the simplified version 1 and version 2. The phase lag plot is not shown because in the steady (simplified) analysis the hot spot always coincides with the high spot. The Version 1 simplified method significantly overpredicts the journal $\max(\Delta T)$, while the Version 2 method predicts results that are in much better agreement, compared to the high-fidelity approach. Nevertheless, the version 2 is much slower than version 1 because it needs to calculate the pad tilting angles along the journal orbit, which can be quite computational intensive for the case with multiple-pad TPJB and dozens of orbit points.
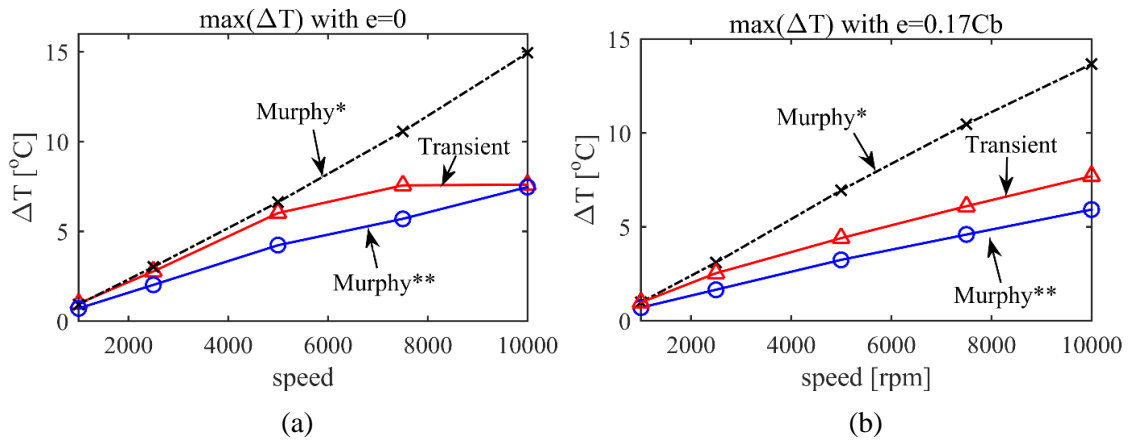
Fig. 7-7 Predicted TPJB journal ΔT for the simplified and high fidelity methods with reduced clearance. (a) eccentricity = 0 (b) eccentricity = $0.17C_b$.

8 CONCLUSION

The thermally induced synchronous instability (Morton effect) problem has been frequently reported in recent years. Great efforts have been devoted to modeling the Morton effect (ME) correctly so that potential instability can be predicted and suppressed effectively. The current dissertation provides a comprehensive summary of ME in Section 1 in terms of causes, symptoms, prediction theories, case studies and solutions. Note that most of the ME solutions are discussed based on individual cases, and due to the complicated nature of ME and diversity of rotor and bearing systems, no universal solutions are available to guarantee the effective suppression of ME in all cases. However, conclusions are listed below to provide some general guidance for turbomachinery designers and troubleshooters.

(1) ME instability may occur when operating away from the vicinity of a critical speed. However, ME is more likely to develop when operating close to a critical speed which has a large deflection at the rotor overhung or bearing node in its mode shape.

(2) ME is not always intensified when the speed increases. It is likely that the instability can be eliminated at high speed above a certain (unstable) speed band.

(3) Suppressing the ME may be accomplished with parameter changes that shift the instability speed band away from the operating speed range.

(4) Increasing the separation margin and damping for the dominant mode shape is likely to suppress the ME, though is not always effective in all cases.

(5) Enhancing the oil cooling and reducing the heat generation are recommended. In certain cases, using a reduced viscosity oil or reducing the bearing L/D ratio may mitigate the ME.

(6) An overhung mass attached at significant distance from the bearing plays a key role in ME development. Reducing the overhung mass and distance will suppress the ME in most cases.

(7) Bearing geometry, load conditions, lubricant properties, etc. all may influence the ME. However, due to the difference and complexity of each rotor-bearing system, the adjustment of these parameters to mitigate the ME may be quite different, or even contradictory between machines.

The high-fidelity transient ME prediction algorithm is proposed in Section 3, which is based on the thermal imbalance method and can be applied to any general rotor configuration with single-overhung on one rotor side or double-overhung masses on both rotor sides. Based on de Jongh's case study, the fully nonlinear double-overhung ME prediction is applied and results are compared to the simplified linear analysis and the single-overhung-wise method. Some useful conclusions are listed below:

(1) The fully nonlinear transient method gives the best accuracy in ME prediction considering that the linear method may overpredict the ME when the bearing orbit grows and the single-overhung-wise method may underpredict the ME by decoupling the ME at both rotor ends.

(2) The bearing pivot flexibility can dominate the pad flexibility in affecting the rotordynamics so the rigid pad model can be a good approximate for the discussed bearing.

The bowed rotor method is proposed in Section 4 to replace the traditional thermal imbalance method, which neglects the thermal bending moment. A hybrid finite element model is established to reduce the computational cost without sacrificing accuracy. Some important conclusions are given below.

(1) The thermal bow model method is more accurate than the thermal imbalance method, which overpredicts the ME in the example studied with larger vibration amplitude and temperature difference ΔT.

(2) the ME can be caused by permanent bow or disk skew in the absence of mechanical imbalance.

(3) Compared with the midspan excitation, the ME is more sensitive and evident when the bow or disk skew is located at the rotor overhung end.

(4) The coupling at the rotor overhung end can affect the thermal deformation, and increasing the radial stiffness of the coupling without changing the coupling mass will reduce the thermal bow at the overhung end and possibly reduce the ME.

The ME testing rig is set up in Section 6 to measure the journal circumferntial tempreature distribution with 20 RTDs, and testing conditions including the supply oil temperature, bearing eccentricity and operating speed are changed to investigate the influence on ME. The proposed high-fidelity ME analysis is applied and results are compared with measurements in Section 7. Some important conclusions are listed below.

(1) The measured maximum journal temperature and peak-peak differential ΔT increase nearly linearly with rotor speed under all conditions.

(2) The measured journal temperature varies in a sinusoidal manner around the circumference. The hot spot is close to but lags the high spot and the cold spot is out of phase with the hot spot. The hot spot lags the high spot by an angle which is speed dependent and increases from 20° at 1,200 rpm to 40° at 5,500 rpm and nearly levels off at high speeds.

(3) The predictions of journal ΔT and hot spot position by the high fidelity transient algorithm show good agreement with measurements.

(4) Simulations demonstrate that the journal ΔT is sensitive to the bearing clearance C_b and mixing coefficient λ. It was found that increasing C_b and reducing λ can reduce the journal ΔT and mitigate the ME under the condition of a constant journal orbit as in the test.

(5) The simplified ME analysis by Murphy and Lorenz [38] is much faster than the transient, high fidelity approach, but may predict significantly higher journal ΔT than the experimental and high fidelity model results, and predict a zero phase lag between the hot spot and high spot. An improved version of the simplified method including journal orbit velocity was developed and showed improved accuracy for journal ΔT prediction relative to the original simplified approach.

The future work includes:

(1) Optimize the high-fidelity Morton effect (ME) software to increase the execution speed. This includes adoption of C++ or FORTRAN, and optimized mesh for 3D lubricant, bearing, and shaft finite element model.

(2) Conduct parametric studies including bearing type, oil viscosity, supply oil temperature, etc. based on case studies to investigate solutions of ME. Criteria will be proposed to help eliminate ME.

(3) Mixing coefficient, i.e., hot oil carryover ratio, will be investigated with CFD software and its effect on rotor temperature distribution will be cautiously analyzed.

(4) Model the friction in the tiling pad spherical pivots and evaluate its influence on the rotor stability. Proper pivot geometries will be recommended to avoid ME.

(5) Investigate the ME in rolling element bearings, tilting pad gas bearings, foil bearings and ferrofluidic seals.

(6) Predict the rotor thermal bow caused by the asymmetric cooling, not heating, in compressors and turbines.

REFERENCES

[1]   Fillon, M., Bligoud J., and Frene J., 1992, "Experimental Study of Tilting-pad
       Journal Bearings-Comparison with Theoretical Thermoelastohydrodynamic
       Results," ASME J. Tribol., **114**(3), pp. 579-587.

[2]   Monmousseau, P., Fillon, M., and Frene J., 1997, "Transient
       Thermoelastohydrodynamic Study of Tilting-pad Journal Bearings—Comparison
       between Experimental Data and Theoretical Results," ASME J. Tribol., **119**(3), pp.
       401-407.

[3]   Dowson, D., Hudson, J., Hunter, B., et al., 1966, "Paper 3: An Experimental
       Investigation of the Thermal Equilibrium of Steadily Loaded Journal
       Bearings," Proc. Inst. Mech. Eng., **181**(2), pp. 70-80.

[4]   Morton, P.G., 1975, "Some Aspects of Thermal Instability in Generators," G.E.C.
       Internal Report No. S/W40 u183.

[5]   Hesseborn, B., 1978, "Measurements of Temperature Unsymmetries in Bearing
       Journal Due to Vibration," Internal report ABB Stal.

[6]   Dimarogonas, A., 1974, "A Study of the Newkirk Effect in Turbomachinery,"
       Wear, **28**(3), pp. 369-382.

[7]   Kellenberger, W., 1980, "Spiral Vibrations due to the Seal Rings in
       Turbogenerators Thermally Induced Interaction between Rotor and Stator,"
       Journal of Mechanical Design, **102**(1), pp. 177-184.

[8] Newkirk, B., 1926, "Shaft Rubbing: Relative Freedom of Rotor Shafts from Sensitiveness to Rubbing Contact When Running above Their Critical Speeds", Mechanical Engineering, **48**(8):830–832.

[9] Schmied, J., 1987, "Spiral Vibrations of Rotors," Proceedings of the ASME Design Technology Conference.

[10] de Jongh, F., 2008, "The Synchronous Rotor Instability Phenomenon-Morton Effect," 37th Turbomachinery Symposium, College Station, TX, pp. 159–167.

[11] Panara, D., Panconi, S., and Griffini, D., 2015, "Numerical Prediction and Experimental Validation of Rotor Thermal Instability," 44th Turbomachinery Symposium, Houston, TX.

[12] de Jongh, F. and Van Der Hoeven, P., eds., 1998, "Application of a Heat Barrier Sleeve to Prevent Synchronous Rotor Instability," 27th Turbomachinery Symposium, Houston, TX, pp. 17–26.

[13] Gomiciaga, R., and Keogh, P., 1999, "Orbit Induced Journal Temperature Variation in Hydrodynamic Bearings," ASME J. Tribol., 121(1), pp. 77–84.

[14] Berot, F., and Dourlens, H., 1999, "On Instability of Overhung Centrifugal Compressors," International Gas.

[15] Kocur, J., and de Jongh, F., 2000, "Thermal Rotor Instability in Gas Compressors," 14th International Gas Convention, Caracas, Venezuela.

[16] de Jongh, F. and Van Der Hoeven, P., eds., 1998, "Application of a Heat Barrier Sleeve to Prevent Synchronous Rotor Instability," 27th Turbomachinery Symposium, Houston, TX, pp. 17–26.

[17] Kirk, G., Guo, Z., and Balbahadur, A., 2003, "Synchronous Thermal Instability Prediction for Overhung Rotors," Proc. 32nd Turbomachinery Symp., Houston, TX, pp. 8-11.

[18] Lorenz, J., and Murphy, B., 2011, "Case Study of Morton Effect Shaft Differential Heating in a Variable-Speed Rotating Electric Machine," ASME Turbo Expo: Turbine Technical Conference and Exposition, Vancouver, Canada, pp. 257-269.

[19] Faulkner, H., Strong, W., and Kirk, R., 1997, "Thermally Induced Synchronous Instability of a Radial Inflow Overhung Turbine, Part II," ASME Design Engineering Technical Conferences, Sacramento, California, USA, Paper No. DETC97/VIB-4174.

[20] Schmied, J., Pozivil, J., and Walch, J., 2008, "Hot Spots in Turboexpander Bearings: Case History, Stability Analysis, Measurements and Operational Experience," ASME 2008 Turbo Expo: Power for Land, Sea, and Air, Berlin, Germany, pp. 1267-1277.

[21] Carrick, H.B., 1999, "Integrally Geared Compresssors and Expanders in the Process Industry," IMechE 7th European Congress on Fluid Machinery for the Oil, Petrochemical, and Related Industries, Hague, Netherlands.

[22] Marscher, W., and Illis, B., 2007, "Journal Bearing Morton Effect Cause of Cyclic Vibration in Compressors," Tribology Transactions, **50**(1), pp 104-113.

[23] Guo, Z., and Kirk, G., 2011, "Morton Effect Induced Synchronous Instability in Mid-Span Rotor–Bearing Systems—Part I: Mechanism Study," J. Vib. Acoust., **133**(6), p. 061004.

[24] Eckert, L., and Schmied, J., 2008, "Spiral Vibration of a Turbogenerator Set: Case History, Stability Analysis, Measurements and Operational Experience," ASME J. Eng. Gas Turbines Power, **130**(1), p. 012509.

[25] Paranjpe, R., and Han, T., 1995, "A Transient Thermohydrodynamic Analysis Including Mass Conserving Cavitation for Hynamically Loaded Journal Bearings," ASME J. Tribol., **117**(3), pp. 369-378.

[26] Childs, D., and Saha, R., 2012, "A New, Iterative, Synchronous-Response Algorithm for Analyzing the Morton Effect," ASME J. Eng. Gas Turbines Power, **134**(7), p. 072501.

[27] Tong, X., and Palazzolo, A., 2017, "Double Overhung Disk and Parameter Effect on Rotordynamic Synchronous Instability-Morton Effect: Part II: Occurrence and Prevention," ASME J. Tribol., **139**(1), p.011706.

[28] Tong, X., and Palazzolo, A., 2016, "The Influence of Hydrodynamic Bearing Configuration on Morton Effect," ASME Turbo Expo, Seoul, South Korea, pp. V07BT31A017.

[29] Suh, J. and Palazzolo, A., 2014, "Three-Dimensional Thermohydrodynamic Morton Effect Analysis—Part II: Parametric Studies," ASME J. Tribol., **136**(3), p. 031707.

[30] Corcoran, J., Rea, H., Cornejo, G., et al., 1997, "Discovering, the Hard Way, How a High Performance Coupling Influenced the Critical Speeds and Bearing Loading of an Overhung Radial Compressor—A Case History," Proc. 17th Turbomachinery Symp., College Station, TX. 1997.

[31] Balbahadur, A. C., and Kirk, R., 2004, "Part I—Theoretical Model for a Synchronous Thermal Instability Operating in Overhung Rotors," Int. J. Rotating Mach., **10**(6), pp. 469–475.

[32] API, 2005, "Tutorial on Rotordynamics: Lateral Critical, Unbalance Response, Stability, Train Torsional and Rotor Balancing," 2nd ed, API 684 Standard, API, Washington, DC.

[33] Kirk, G., and Guo, Z., 2013, "Design Tool for Prediction of Thermal Synchronous Instability," ASME International Design Engineering Technical Conferences and Computers and Information in Engineering Conference, Portland, Oregon, USA.

[34] Keogh, P., and Morton, P., 1993, "Journal Bearing Differential Heating Evaluation with Influence on RotorDynamic Behaviour," Proc. R. Soc. London, Ser. A: Math. Phys. Sci., **441**(1913), pp. 527–548.

[35] Keogh, P., and Morton, P., 1994, "The Dynamic Nature of Rotor Thermal Bending Due to Unsteady Lubricant Shearing Within a Bearing," Proc. R. Soc. London, Ser. A: Math. Phys. Sci., **445**(1924), pp. 273–290.

[36] Larsson, B., 1999, "Journal Asymmetric Heating—Part I: Nonstationary Bow," ASME J. Tribol., **121**(1), pp. 157–163.

[37] Larsson, B., 1999, "Journal Asymmetric Heating—Part II: Alteration of Rotor Dynamic Properties," ASME J. Tribol., **121**(1), pp. 164–168.

[38] Murphy, B., and Lorenz, J., 2010, "Simplified Morton Effect Analysis for Synchronous Spiral Instability," J. Vib. Acoust., **132**(5), p. 051008.

[39] Lee, J., and Palazzolo, A., 2012, "Morton Effect Cyclic Vibration Amplitude Determination for Tilt Pad Bearing Supported Machinery," ASME J. Tribol., **135**(1), p. 011701.

[40] Suh, J., and Palazzolo, A., 2014, "Three-Dimensional Thermohydrodynamic Morton Effect Simulation—Part I: Theoretical Model," ASME J. Tribol., **136**(3), p. 031706.

[41] Grigor'ev, B.S., Fedorov, A.E., and Schmied, J., 2015,"New Mathematical Model for the Morton Effect Based on the THD Analysis," Proc. 9th IFToMM Int. Conf. on Rotor Dynamics, Milan, Italy, pp. 2243-2253.

[42] Tong, X., Palazzolo, A., and Suh, J., 2016, "Rotordynamic Morton Effect Simulation With Transient, Thermal Shaft Bow," ASME J. Tribol., **138**(3), p. 031705.

[43] Tong, X. and Palazzolo, A., 2017, "Double Overhung Disk and Parameter Effect on Rotordynamic Synchronous Instability-Morton Effect: Part I: Theory and Modeling Approach," ASME J. Tribol., **139**(1), p. 011705.

[44] Tucker, P. and Keogh, P., 1996, "On the Dynamic Thermal State in a Hydrodynamic Bearing with a Whirling Journal Using CFD Techniques", ASME J. Tribol., **118**(2), pp. 356-363.

[45] Lund, J. and Tonnesen, J., 1984, "An Approximate Analysis of the Temperature Conditions in a Journal Bearing. Part II: Application," ASME J. Tribol., **106**(2), pp. 237-244.

[46] Lorenz, J., 2009, "Implementation of Fluid-Film Bearing Shaft Differential Heating Calculations Using Commerical CFD Software," M.S. thesis, University of Illinois at Urbana-Champaign.

[47] Balbahadur, A., 2001, "A Thermoelastohydrodynamic Model of the Morton Effect Operating in Overhung Rotors Supported by Plain or Tilting Pad Journal Bearings," Ph.D. thesis, Virginia Tech, Blacksburg, Virginia.

[48] API, 2002, "Axial and Centrifugal Compressors and Expander-Compressors for Petroleum, Chemical and Gas Industry Services," API 617 Standard, API, Washington, DC.

[49] Marin, M., 2012, "Rotor Dynamics of Overhung Rotors: Hysteretic Dynamic Behavior," ASME Turbo Expo 2012: Turbine Technical Conference and Exposition, Copenhagen, Denmark.

[50] Khonsari, M. and Beaman, J., 1986, "Thermohydrodynamic Analysis of Laminar Incompressible Journal Bearings," ASLE transactions, **29**(2): pp. 141-150.

[51] Kim, J., Palazzolo, A., and R. Gadangi, 1995, "Dynamic Characteristics of TEHD Tilt Pad Journal Bearing Simulation Including Multiple Mode Pad Flexibility Model," J. Vib. Acoust, **117**(1): pp. 123-135.

[52] Knight, J. and Barrett, L., 1988, "Analysis of Tilting Pad Journal Bearings with Heat Transfer Effects," ASME J. Tribol., **110**(1), pp. 128-133.

[53] Gadangi, R., Palazzolo, A., and Kim, J., 1996, "Transient Analysis of Plain and Tilt Pad Journal Bearings Including Fluid Film Temperature Effects," ASME J. Tribol., **118**(2), pp. 423-430.

[54] He, M., et al., 2005, "Thermohydrodynamic Modeling of Leading-edge Groove Bearings under Starvation Condition," Tribology transactions, **48**(3), pp. 362-369.

[55] Heinrich, J., et al., 1977, "An 'Upwind' Finite Element Scheme for Two-dimensional Convective Transport Equation," International Journal for Numerical Methods in Engineering, **11**(1): p. 131-143.

[56] Ettles, C., 1980, "The Analysis and Performance of Pivoted Pad Journal Bearings Considering Thermal and Elastic Effects," Journal of Lubrication Technology, **102**(2), pp. 182-191.

[57] Heshmat, H. and Pinkus, O., 1986, "Mixing Inlet Temperatures in Hydrodynamic Bearings," ASME J. Tribol., **108**(2): p. 231-244.

[58] Suh, J., 2014, "Nonlinear Transient Rotor-Bearing Dynamic Analysis Considering Shaft Thermal Bow Induced Instability Problem," Ph. D. thesis, TAMU, College Station, TX.

[59] Young, W.C. and Budynas, R.G., 2002, "Roark's formulas for stress and strain," Vol. 7: McGraw-Hill New York.

[60] Nicholas, J., Gunter, E., and Allaire, P., 1976, "Effect of Residual Shaft Bow on Unbalance Response and Balancing of a Single Mass Flexible Rotor—Part I: Unbalance Response," ASME J. Eng. Gas Turbines Power, **98**(2): p. 171-181.

[61] Nicholas, J., Gunter, E., and Allaire, P., 1976, "Effect of Residual Shaft Bow on Unbalance Response and Balancing of a Single Mass Flexible Rotor—Part II: Balancing," ASME J. Eng. Gas Turbines Power, **98**(2): p. 182-187.

[62] Salamone, D., 1977, "Synchronous Unbalance Response of a Multimass Flexible Rotor Considering Shaft Warp and Disk Skew," University of Virginia: Charlottesville, VA.

[63] Salamone, D., and Gunter, E., 1978, "Effects of Shaft Warp and Disk Skew on the Synchronous Unbalance Response of a Multimass Rotor in Fluid Film Bearings," Proc. of ASME Fluid Film Bearing and Rotor Bearing System Design and Optimization, pp. 79.107.

[64] Balbahadur, A., and Kirk, R., 2004, "Part II—Case Studies for a Synchronous Thermal Instability Operating in Overhung Rotors," Int. J. Rotating Mach., 10(6), pp. 477–487.

[65] Simmons, J. and Lawrence, C., 1996, "Performance Experiments with a 200 mm, Offset Pivot Journal Pad Bearing," Tribology Transactions, **39**(4): p. 969-973.

[66] DeCamillo, S. and K. Brockwell. 2001, "A Study of Parameters that Affect Pivoted Shoe Journal Bearing Performance in High-speed Turbomachinery," in Proc. of 30th Turbomachinery Symposium, Houston, TX.

[67] Tong, X. and Palazzolo, A., 2017, "A Review of the Rotordynamic Thermally Induced Synchronous Instability (Morton) Effect," Applied Mechanics Reviews, **69**(6): 060801.

[68] Carter, C.R. and Childs, D.W., 2009, "Measurements versus Predictions for the Rotordynamic Characteristics of a Five-pad Rocker-pivot Tilting-pad Bearing in Load-between-pad Configuration," Journal of Engineering for Gas Turbines and Power, **131**(1): p. 012507.

[69] Kulhanek, C.D. and Childs, D.W., 2012, "Measured Static and Rotordynamic

Coefficient Results for a Rocker-Pivot, Tilting-Pad Bearing With 50 and 60%

Offsets," Journal of Engineering for Gas Turbines and Power, **134**(5): p. 052505.

APPENDIX A

FINITE ELEMENT FORMULATION OF REYNOLDS EQUATION

This appendix deals with the derivation of finite element equations for the variable viscosity Reynolds equation. The governing equation and the boundary conditions are:

$$\nabla \cdot (D_1 \nabla P) + \nabla D_2 \cdot (U_2 - U_1) + (\nabla h) \cdot U_1 + \partial h / \partial t = 0 \tag{A.1}$$

Subject to the boundary conditions:

$$\begin{aligned} P &= P^* \text{ on } \Gamma_p \\ P &= q^* \ \text{ on } \Gamma_q \end{aligned} \tag{A.2}$$
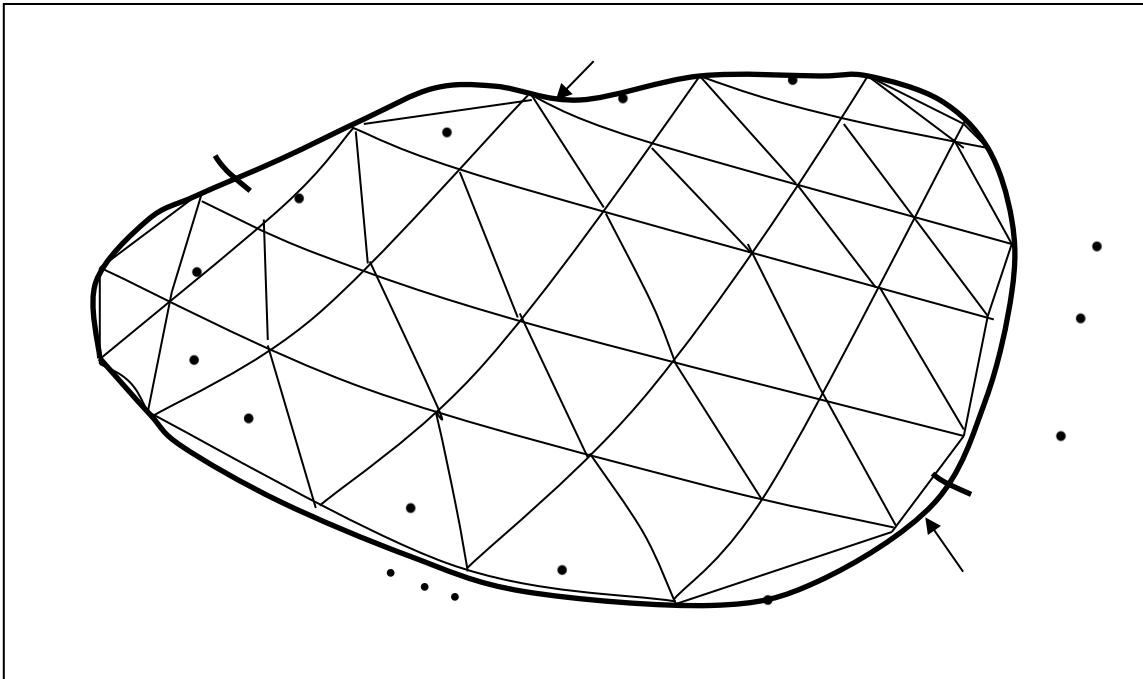

Fig. A.1 FEM Mesh Covering Lubricant Domain

The problem domain with boundaries marked is shown in Fig. A.1. The boundary comprises of two regions, on the first region Γ_p pressure is prescribed, and on the second region Γ_q, flow rate is prescribed. The regions are such that they do not overlap $\Gamma_p \cap \Gamma_q = 0$ and $\Gamma_p \cup \Gamma_q = \Gamma$. The functional for variable viscosity Reynolds equation with the boundary conditions mentioned above is obtained using variational principles.

$$J_p = \int_\Omega \left[-\frac{1}{2} D_1 \nabla P \cdot \nabla P + D_2 U \cdot \nabla P + P \frac{\partial h}{\partial t} \right] d\Omega + \int_{\Gamma_q} Pq \cdot n d\Gamma \tag{A.3}$$

The problem is to find a function P which minimizes the functional shown above. By utilizing the maxima and minima principles, the first derivative of the functional with respect to the function itself should vanish at the minimum. This is shown as:

$$\frac{\partial J_p}{\partial P} = 0 \tag{A.4}$$

The finite element method used while discretizing the problem domain is the Galerkin method. The approximated function P_{ap} is expressed in terms of vectors of shape functions and nodal values of approximated function as shown below;

$$P_{ap} = N \cdot P \tag{A.5}$$

In the above equation, vector N is the shape function vector and the vector P is the nodal pressure vector. The final global finite element matrices can then be expressed in the following way.

$$[K_f]\{P\} = \{F_f\} \tag{A.6}$$

Where,

$$[K_f] = -\int_\Omega D_1 \left(\frac{\partial N_i}{\partial x} \frac{\partial N_j}{\partial x} + \frac{\partial N_i}{\partial y} \frac{\partial N_j}{\partial y} \right) d\Omega$$

$$\{B\} = \int_\Omega D_2 U_x \frac{\partial N_i}{\partial x} d\Omega + \int_\Omega D_2 U_y \frac{\partial N_i}{\partial y} d\Omega$$

$$\{S\} = -\frac{\partial h}{\partial t} \int_\Omega N_i d\Omega$$

$$\{L\} = -\int_{\Gamma_q} q N_i d\Gamma$$

(A.7)

The above equations are in the final global form. The problem domain needs to be discretized into finite element as shown in Fig. A.1. Discretization of the domain implies the domain Ω is now represented by $\sum \Omega_e(i)$, where i=1 to n_{el}, and Ω_e is the domain of discretized finite element, and n_{el} is the total number of finite elements. The global matrix $[K_f]$ and the force vector $\{F_f\}$ are given by;

$$[K_f] = \sum_{i=1}^{n_{el}} [K_f^e]$$

$$\{F_f\} = \sum_{i=1}^{n_{el}} \{F_f^e\}$$

(A.8)

In the above equations, superscript 'e' implies that these matrices and vectors have been evaluated on the elemental domain. The simplex triangular element consists of linear shape functions shown in Fig A.2 are used.
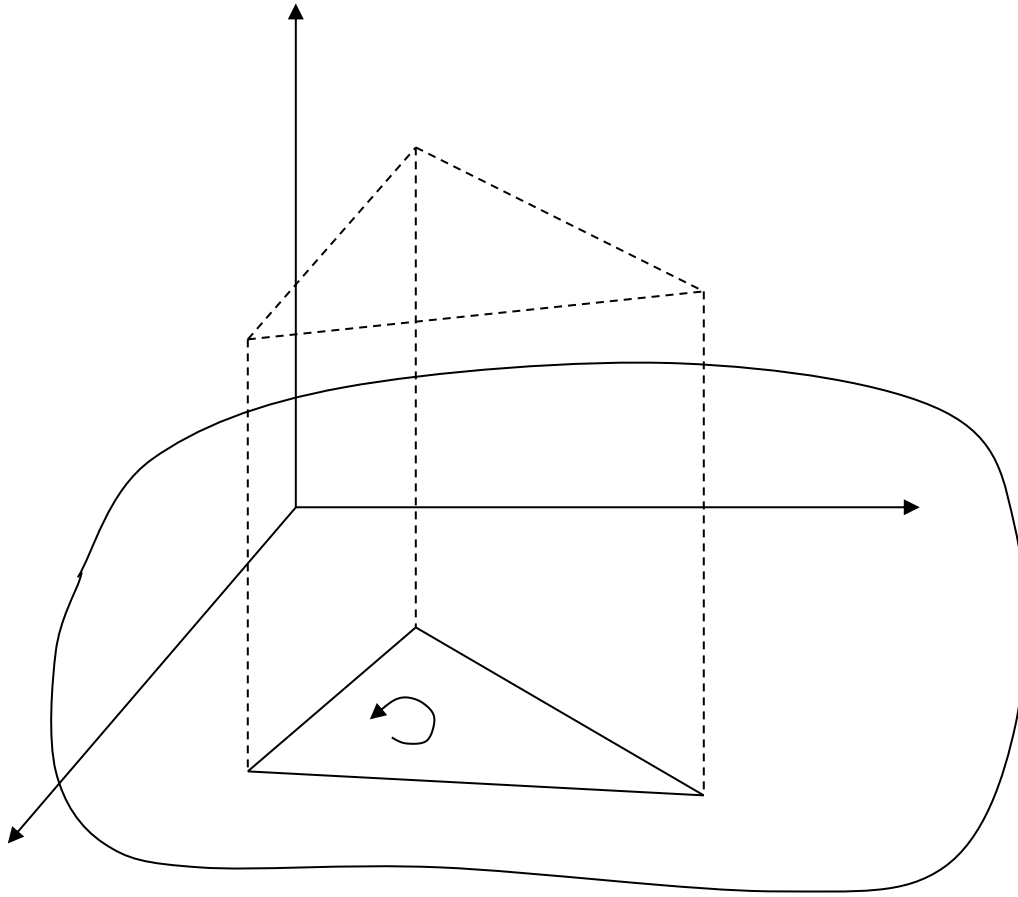
Fig. A.2 Linear Interpolation of Pressure in a 3 Node Simplex Element

The discretization of the Reynolds equation uses the simplex triangular elements, and the shape functions for a simplex triangular element are given by.

$$N_i = \left(\frac{1}{2A^e} \right) \left(a_i^e + b_i^e + c_i^e \right), \quad i = 1, 2, 3 \tag{A.9}$$

Where, $A^e = \frac{1}{2} \left[(x_2 y_3 - x_3 y_2) - (x_1 y_3 - x_3 y_1) + (x_1 y_2 - x_2 y_1) \right]$ \hfill (A.10)

$$\begin{bmatrix} a_1 & a_2 & a_3 \\ b_1 & b_2 & b_3 \\ c_1 & c_2 & c_3 \end{bmatrix} = \begin{bmatrix} x_2 y_3 - x_3 y_2 & x_3 y_1 - x_1 y_3 & x_1 y_2 - x_2 y_1 \\ y_2 - y_3 & y_3 - y_1 & y_1 - y_2 \\ x_3 - x_2 & x_1 - x_3 & x_2 - x_1 \end{bmatrix} \qquad (A.11)$$

The area and line integrals for these shape functions are performed using the following exact expressions

$$\int_{A^c} N_1^\alpha N_2^\beta N_3^\gamma \, dA = 2A^e \frac{\alpha!\beta!\gamma!}{(\alpha + \beta + \gamma + 2)!}$$

$$\int_{side1-2} N_1^\alpha N_2^\beta \, dL = L_{1-2} \frac{\alpha!\beta!}{(\alpha + \beta + 1)!} \qquad (A.12)$$

$$\int_{side1-2} N_3^\gamma \, dL = 0$$

where '!' denotes a factorial and L_{1-2} is the length of the element side from nodes 1 to 2. Substituting the shape functions into Eq. (A.7), applying the exact integration equations given above, the final elemental matrices and vectors are given by

$$[K_f] = -\int_\Omega D_1 \left(\frac{\partial N_i}{\partial x} \frac{\partial N_j}{\partial x} + \frac{\partial N_i}{\partial y} \frac{\partial N_j}{\partial y} \right) d\Omega = -(b_i b_j + c_i c_j) \frac{\bar{C}_1}{4A^e}$$

$$\{B\} = \int_\Omega D_2 U_x \frac{\partial N_i}{\partial x} d\Omega + \int_\Omega D_2 U_y \frac{\partial N_i}{\partial y} d\Omega = (U_x b_i + U_y c_i) \frac{\bar{C}_2}{2}$$

$$\{S\} = -\frac{\partial h}{\partial t} \int_\Omega N_i \, d\Omega = -\frac{\rho A^e}{3} \frac{\partial h}{\partial t} \qquad (A.13)$$

$$\{L\} = -\int_{\Gamma_q} q N_i \, d\Gamma = -q \frac{L_{i-j}}{2}$$

$$\bar{C}_i = \frac{1}{A^e} \int_{\Omega_e} D_i \, d\Omega_e$$

The coefficients defined in Eq. (A.13) are integrated over the elements and divided by their areas, to get an average.

APPENDIX B

FINITE ELEMENT FORMULATION OF ENERGY EQUATION

The solution of Reynolds equation gives pressure distribution throughout the fluid film. This pressure distribution is used in evaluating the velocity profile in the fluid film. The solution of energy equation requires the velocity profile. The problem domain for the energy equation with different boundaries is shown in Fig. B.1, and the boundary is comprised of three different regions. The first region is the region over which the temperature is prescribed Γ_T, the second region is the part of the boundary over which heat flux is prescribed Γ_f, and the third region is the one over which convection is prescribed Γ_h.
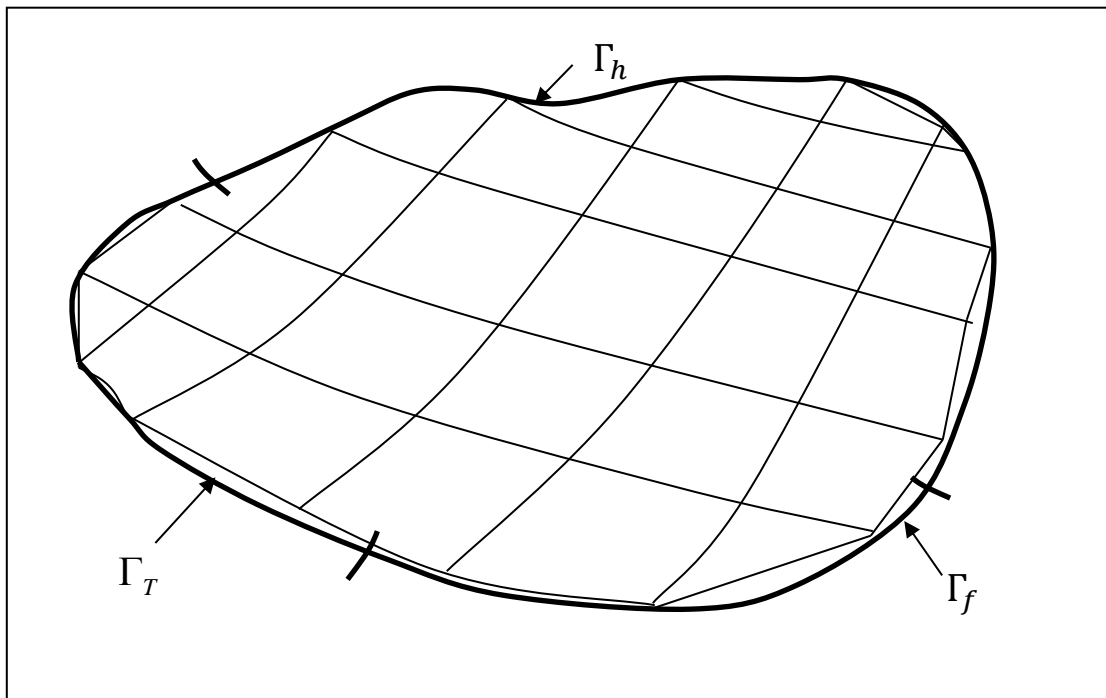

Fig. B.1 FEM mesh covering lubricant domain

The governing equation is given by;

$$\rho c_p \left(\frac{\partial T}{\partial t} + u \cdot \nabla T \right) = k \nabla \cdot \nabla T + \Phi \tag{B.1}$$

Subject to the following boundary conditions;

$$
\begin{aligned}
T &= T^* & &on \ \Gamma_T \\
q &= q^* & &on \ \Gamma_f \\
q &= -h(T - T_\infty) & &on \ \Gamma_T
\end{aligned}
\tag{B.2}
$$

Galerkin method is used to find the weighted residual equation for the solution of energy equation. On applying, the weighted residual to the governing equation gives

$$\int_\Omega \left(\rho c_p \left(\frac{\partial T}{\partial t} + u \cdot \nabla T \right) - Q - k \nabla \cdot \nabla T \right) W d\Omega = 0 \tag{B.3}$$

Where W is the weight function. Applying Gauss theorem and applying the boundary condition, Eq. (B.1) becomes;

$$
\int_\Omega \rho c_p \frac{\partial T}{\partial t} W d\Omega + \int_\Omega \rho c_p u \cdot \nabla T W d\Omega - \int_\Omega Q W d\Omega + \int_\Omega k \nabla T \cdot \nabla W d\Omega
$$
$$
- \int_{\Gamma_T} (kTW) \cdot n d\Gamma + \int_{\Gamma_f} (q^* W) \cdot n d\Gamma - \int_{\Gamma_h} h T_\infty W d\Gamma + \int_{\Gamma_h} h T W d\Gamma = 0
\tag{B.4}
$$

The solution to the Eq. (B.4) is interpolated over an element using the shape functions as follows

$$T = \widehat{N} \times \widehat{T} \tag{B.5}$$

In the above equation the vector $\widehat{N}$ contains the shape functions and the vector $\widehat{T}$ contains the nodal values of temperatures on that particular element. Substituting the interpolated temperature into Eq. (B.4), and factoring out T;

$$\left[\int_{\Omega} \rho c_p W N_j d\Omega\right]\{\dot{T}_j\} + \left[\int_{\Omega} (\rho c_p W u \cdot \nabla N_j + k \nabla W \cdot \nabla N_j) d\Omega + \int_{\Gamma_h} h W N_j d\Gamma\right]\{T_j\}$$

$$= \int_{\Omega} Q W d\Omega + \int_{\Gamma_f} q W d\Gamma + \int_{\Gamma_T} (k\nabla T) \cdot n W d\Gamma + \int_{\Gamma_h} h T_{\infty} W d\Gamma \qquad (B.6)$$

The weight functions are selected such that their values on the boundary Γ_T vanish. Hence, from the above equation, the following integration on the temperature prescribed boundary vanishes;

$$\int_{\Gamma_T} (k\nabla T) \cdot n W d\Gamma = 0 \qquad (B.7)$$

The system of equations can be represented as matrices and vectors in the following way;

$$[K_m] = \int_{\Omega} \rho c_p W_i N_j d\Omega$$

$$[K_v] = \int_{\Omega} \rho c_p W_i u \cdot \nabla N_j d\Omega$$

$$[K_c] = \int_{\Omega} k \nabla W_i \cdot \nabla N_j d\Omega$$

$$[K_h] = \int_{\Gamma_h} h W_i N_j d\Gamma d\Omega \qquad (B.8)$$

$$\{F_Q\} = \int_{\Omega} Q W_i d\Omega$$

$$\{F_h\} = \int_{\Gamma_h} h T_{\infty} W_i d\Gamma$$

$$\{F_f\} = \int_{\Gamma_f} (q W_i) d\Gamma$$

On elemental basis each of the vectors and matrix is expressed as:

$$[K_m^e] = \int_{\Omega^e} \rho c_p W_i^e N_j^e d\Omega^e$$

$$[K_v^e] = \int_{\Omega^e} \rho c_p W_i^e u \cdot \nabla N_j^e d\Omega^e$$

$$[K_c^e] = \int_{\Omega} k \nabla W_i^e \cdot \nabla N_j^e d\Omega^e$$

$$[K_h^e] = \int_{\Gamma_h} h W_i^e N_j^e d\Gamma d\Omega^e \qquad (B.9)$$

$$\{F_Q^e\} = \int_{\Omega^e} Q W_i^e d\Omega^e$$

$$\{F_h^e\} = \int_{\Gamma_h^e} h T_\infty W_i^e d\Gamma^e$$

$$\{F_f^e\} = \int_{\Gamma_f^e} \left(q W_i^e \right) d\Gamma^e$$

Discretization of the problem is done with 8-node cubic iso-parametric elements. The 1D two-node iso-parametric shape function for each natural coordinate is shown in Eq. (B.9), and the 3D eight-node isoparametric shape functions are the product of 1D two-node shape functions in three directions, as shown in Eq. (B.10).

$$\psi_{1\xi}(\xi) = \frac{1}{2}(1-\xi) \quad \psi_{1\eta}(\eta) = \frac{1}{2}(1-\eta) \quad \psi_{1\tau}(\tau) = \frac{1}{2}(1-\tau) \quad N_1 = \psi_{1\xi}(\xi)\psi_{1\eta}(\eta)\psi_{1\tau}(\tau)$$

$$\psi_{2\xi}(\xi) = \frac{1}{2}(1+\xi) \quad \psi_{2\eta}(\eta) = \frac{1}{2}(1-\eta) \quad \psi_{2\tau}(\tau) = \frac{1}{2}(1-\tau) \quad N_2 = \psi_{2\xi}(\xi)\psi_{2\eta}(\eta)\psi_{2\tau}(\tau)$$

$$\psi_{3\xi}(\xi) = \frac{1}{2}(1-\xi) \quad \psi_{3\eta}(\eta) = \frac{1}{2}(1+\eta) \quad \psi_{3\tau}(\tau) = \frac{1}{2}(1-\tau) \quad N_3 = \psi_{3\xi}(\xi)\psi_{3\eta}(\eta)\psi_{3\tau}(\tau)$$

$$\psi_{4\xi}(\xi) = \frac{1}{2}(1+\xi) \quad \psi_{4\eta}(\eta) = \frac{1}{2}(1+\eta) \quad \psi_{4\tau}(\tau) = \frac{1}{2}(1-\tau) \quad N_4 = \psi_{4\xi}(\xi)\psi_{4\eta}(\eta)\psi_{4\tau}(\tau)$$

$$\psi_{5\xi}(\xi) = \frac{1}{2}(1-\xi) \quad \psi_{5\eta}(\eta) = \frac{1}{2}(1-\eta) \quad \psi_{5\tau}(\tau) = \frac{1}{2}(1+\tau) \quad N_5 = \psi_{5\xi}(\xi)\psi_{5\eta}(\eta)\psi_{5\tau}(\tau)$$

$$\psi_{6\xi}(\xi) = \frac{1}{2}(1+\xi) \quad \psi_{6\eta}(\eta) = \frac{1}{2}(1-\eta) \quad \psi_{6\tau}(\tau) = \frac{1}{2}(1+\tau) \quad N_6 = \psi_{6\xi}(\xi)\psi_{6\eta}(\eta)\psi_{6\tau}(\tau)$$

$$\psi_{7\xi}(\xi) = \frac{1}{2}(1-\xi) \quad \psi_{7\eta}(\eta) = \frac{1}{2}(1+\eta) \quad \psi_{7\tau}(\tau) = \frac{1}{2}(1+\tau) \quad N_7 = \psi_{7\xi}(\xi)\psi_{7\eta}(\eta)\psi_{7\tau}(\tau)$$

$$\psi_{8\xi}(\xi) = \frac{1}{2}(1+\xi) \quad \psi_{8\eta}(\eta) = \frac{1}{2}(1+\eta) \quad \psi_{8\tau}(\tau) = \frac{1}{2}(1+\tau) \quad N_8 = \psi_{8\xi}(\xi)\psi_{8\eta}(\eta)\psi_{8\tau}(\tau)$$

$$(B.10)$$

The convection term in the energy equation causes an oscillation of temperature. To get rid of this problem, the classic Galerkin scheme (B.11) is modified by adopting the upwinding scheme. The new weight function (B.12) is updated based on the direction and amplitude of the fluid flow velocity.

$$W_i(\xi, \eta, \tau) = N_i(\xi, \eta, \tau) = \psi_{i\xi}(\xi)\psi_{i\eta}(\eta)\psi_{i\tau}(\tau), \quad i = 1, \ldots, 8 \tag{B.11}$$

$$W_i(\xi, \eta, \tau) = [\psi_{i\xi}(\xi) - \alpha_{ij}\frac{3}{4}(1 - \xi^2)] \cdot [\psi_{i\eta}(\eta) -$$

$$\beta_{ij}\frac{3}{4}(1 - \eta^2)] \cdot [\psi_{i\tau}(\eta) - \gamma_{ij}\frac{3}{4}(1 - \tau^2)] \tag{B.12}$$

The upwinding parameters α_{ij}, β_{ij} and γ_{ij} depend on the velocity component u_{ij} along element line $i - j$, the mesh line size h_{ij} between node number i and j, and the thermal diffusivity k. The parameter Pe_{ij} is called a local Peclet number and is defined as:

$$Pe_{ij} = \frac{u_{ij}h_{ij}}{k} \tag{B.13}$$

The velocity u_{ij} along element line $i - j$ is defined as follows:

$$u_{ij} = \frac{1}{2}(\boldsymbol{u_i} + \boldsymbol{u_j}) \cdot \boldsymbol{l_{ij}} \tag{B.14}$$

Where, $\boldsymbol{u_i}$ denotes the velocity vector at the node i, and $\boldsymbol{l_{ij}}$ is the unit vector along the direction $i - j$. The optimum parameters of α_{ij}, β_{ij} and γ_{ij} can be determined by Pe_{ij} as follows:

$$\alpha_{ij} = \coth\left(\frac{Pe_{ij}}{2}\right) - \frac{2}{Pe_{ij}}$$

$$\beta_{ij} = \coth\left(\frac{Pe_{ij}}{2}\right) - \frac{2}{Pe_{ij}} \tag{B.15}$$

$$\gamma_{ij} = \coth\left(\frac{Pe_{ij}}{2}\right) - \frac{2}{Pe_{ij}}$$

Note that although α_{ij}, β_{ij} and γ_{ij} have similar expressions, the corresponding Pe_{ij} is different due to different velocity components.

With the shape function N_i in Eq. (B.10), the integration domain in Eq. (B.9) can be mapped into the natural coordinate and the integration can be simplified with Gauss-Quadrature numerical integration method. The Gauss quadrature points and the corresponding weight factors are shown in Table B.1. The Gauss quadrature then can be applied on an elemental basis, and the elemental values of the matrices and vectors can be represented as;

$$[K_m^e] = \sum_{\tau=1}^{2}\sum_{\eta=1}^{2}\sum_{\xi=1}^{2} \rho c_p W_i^e N_j^e J w_\xi w_\eta w_\tau$$

$$[K_v^e] = \sum_{\tau=1}^{2}\sum_{\eta=1}^{2}\sum_{\xi=1}^{2} \rho c_p W_i^e u \cdot \nabla N_j^e J w_\xi w_\eta w_\tau$$

$$[K_c^e] = \sum_{\tau=1}^{2}\sum_{\eta=1}^{2}\sum_{\xi=1}^{2} k \nabla W_i^e \cdot \nabla N_j^e J w_\xi w_\eta w_\tau$$

$$[K_h^e] = \sum_{\tau=1}^{2}\sum_{\eta=1}^{2}\sum_{\xi=1}^{2} h W_i^e N_j^e J w_\xi w_\eta w_\tau \qquad \text{(B.11)}$$

$$\{F_Q^e\} = \sum_{\tau=1}^{2}\sum_{\eta=1}^{2}\sum_{\xi=1}^{2} Q W_i^e J w_\xi w_\eta w_\tau$$

$$\{F_h^e\} = \sum_{\tau=1}^{2}\sum_{\eta=1}^{2}\sum_{\xi=1}^{2} h T_\infty W_i^e J w_\xi w_\eta w_\tau$$

$$\{F_f^e\} = \sum_{\tau=1}^{2}\sum_{\eta=1}^{2}\sum_{\xi=1}^{2} q W_i^e J w_\xi w_\eta w_\tau$$

where J is the Jacobian matrix.

The shape functions and weight functions are evaluated at each Gauss point. These element matrices and vectors are now assembled together in a global form following the element and nodal connectivity. The global form of the set of equations is

$$[K_m]\{\dot{T}\} + [K_T]\{T\} = \{F_T\} \tag{B.12}$$

Where,

$$[K_m] = \sum_{e=1}^{n_{el}} [K_m^{\,e}] \tag{B.13}$$

$$[K_T] = \sum_{e=1}^{n_{el}} \left\{ [K_v^{\,e}] + [K_c^{\,e}] + [K_h^{\,e}] \right\} \tag{B.14}$$

$$[F_T] = \sum_{e=1}^{n_{el}} \left\{ \{F_Q^{\,e}\} + \{F_h^{\,e}\} + \{F_f^{\,e}\} \right\} \tag{B.15}$$

The mass or distribution matrix $[K_m]$ is symmetric and banded but it should be noted that matrix $[K_T]$ is an asymmetric banded matrix.

Table B.1 Gauss Quadrature Points and Weight Factors

Gauss point $(\dot{x}_I, \dot{y}_J)$	Gauss Weights w_ξ	Gauss Weights w_η	Gauss Weights w_τ
$(-1/\sqrt{3}, -1/\sqrt{3}, -1/\sqrt{3})$	1	1	1
$(-1/\sqrt{3},\ 1/\sqrt{3}, -1/\sqrt{3})$	1	1	1
$(\ 1/\sqrt{3}, -1/\sqrt{3}, -1/\sqrt{3})$	1	1	1
$(\ 1/\sqrt{3},\ 1/\sqrt{3}, -1/\sqrt{3})$	1	1	1
$(-1/\sqrt{3}, -1/\sqrt{3},\ 1/\sqrt{3})$	1	1	1
$(-1/\sqrt{3},\ 1/\sqrt{3},\ 1/\sqrt{3})$	1	1	1
$(\ 1/\sqrt{3}, -1/\sqrt{3},\ 1/\sqrt{3})$	1	1	1
$(\ 1/\sqrt{3},\ 1/\sqrt{3},\ 1/\sqrt{3})$	1	1	1

FINITE ELEMENT FORMULATION FOR THERMAL DEFORMATION

(1) The stiffness matrix of a 3D hexahedron element.

$$K = \int_{-1}^{1}\int_{-1}^{1}\int_{-1}^{1} B_e^T (\xi_1,\xi_2,\xi_3) E_e B_e(\xi_1,\xi_2,\xi_3) \times \det(J(\xi_1,\xi_2,\xi_3))d\xi_1 d\xi_2 d\xi_3$$

, where, ξ_1,ξ_2,ξ_3 are the natural coordinate axis, x_1, x_2, x_3 are the physical coordinate axis,

B_e is the coefficient matrix in $\varepsilon = B_e u_e$, where $u_e = (u_{1,1}^e, u_{2,1}^e, u_{3,1}^e, \dots, u_{1,8}^e, u_{2,8}^e, u_{3,8}^e)^T$,

$\varepsilon = (\frac{\partial u1}{\partial x1}, \frac{\partial u1}{\partial x2}, \frac{\partial u1}{\partial x3}, \frac{\partial u2}{\partial x1}, \frac{\partial u2}{\partial x2}, \frac{\partial u2}{\partial x3}, \frac{\partial u3}{\partial x1}, \frac{\partial u3}{\partial x2}, \frac{\partial u3}{\partial x3})^T$. E is the constitutive relation matrix and

for an isotropic material can be expressed by

$$E_e = \frac{E}{(1+v)(1-2v)}\begin{bmatrix} P & 0_{3\times3} \\ 0_{3\times3} & Q \end{bmatrix},$$

where $P = \begin{bmatrix} 1-v & v & v \\ v & 1-v & v \\ v & v & 1-v \end{bmatrix}, Q = \begin{bmatrix} 1-2v/2 & 0 & 0 \\ 0 & 1-2v/2 & 0 \\ 0 & 0 & 1-2v/2 \end{bmatrix}$

$J(\xi_1,\xi_2,\xi_3)$ is the Jacobian matrix and can be expressed as

$$J = \begin{bmatrix} \frac{\partial x1}{\partial \xi1} & \frac{\partial x2}{\partial \xi1} & \frac{\partial x3}{\partial \xi1} \\ \frac{\partial x1}{\partial \xi2} & \frac{\partial x2}{\partial \xi2} & \frac{\partial x3}{\partial \xi2} \\ \frac{\partial x1}{\partial \xi3} & \frac{\partial x2}{\partial \xi3} & \frac{\partial x3}{\partial \xi3} \end{bmatrix}. \quad J^* = J^{-1} = \begin{bmatrix} J_{11}^* & J_{12}^* & J_{13}^* \\ J_{21}^* & J_{22}^* & J_{23}^* \\ J_{31}^* & J_{32}^* & J_{33}^* \end{bmatrix}.$$

$B_e = A_1 A_2$, where A_1 and A_2 can be expressed below.

$$A_1 = \begin{bmatrix} J_{11}^* & J_{12}^* & J_{13}^* & 0 & 0 & 0 & 0 & 0 & 0 \\ 0 & 0 & 0 & J_{21}^* & J_{22}^* & J_{23}^* & 0 & 0 & 0 \\ 0 & 0 & 0 & 0 & 0 & 0 & J_{31}^* & J_{32}^* & J_{33}^* \\ J_{21}^* & J_{22}^* & J_{23}^* & J_{11}^* & J_{12}^* & J_{13}^* & 0 & 0 & 0 \\ 0 & 0 & 0 & J_{31}^* & J_{32}^* & J_{33}^* & J_{21}^* & J_{22}^* & J_{23}^* \\ J_{31}^* & J_{32}^* & J_{33}^* & 0 & 0 & 0 & J_{11}^* & J_{12}^* & J_{13}^* \end{bmatrix}_{6\times9},$$

$$A_2 = \begin{bmatrix} N_{1,1} & 0 & 0 & N_{2,1} & 0 & 0 & & N_{8,1} & 0 & 0 \\ N_{1,2} & 0 & 0 & N_{2,2} & 0 & 0 \cdots & & N_{8,2} & 0 & 0 \\ N_{1,3} & 0 & 0 & N_{2,3} & 0 & 0 & & N_{8,3} & 0 & 0 \\ 0 & N_{1,1} & 0 & 0 & N_{2,1} & 0 & & 0 & N_{8,1} & 0 \\ 0 & N_{1,2} & 0 & 0 & N_{2,2} & 0 \cdots & & 0 & N_{8,2} & 0 \\ 0 & N_{1,3} & 0 & 0 & N_{2,3} & 0 & & 0 & N_{8,3} & 0 \\ 0 & 0 & N_{1,1} & 0 & 0 & N_{2,1} & & 0 & 0 & N_{8,1} \\ 0 & 0 & N_{1,2} & 0 & 0 & N_{2,2} \cdots & & 0 & 0 & N_{8,2} \\ 0 & 0 & N_{1,3} & 0 & 0 & N_{2,3} & & 0 & 0 & N_{8,3} \end{bmatrix}_{9 \times 24}$$

(2) The thermal load vector $F_{\Delta T}$ of a 3D hexahedron element

$$F_{\Delta T} = \int_{-1}^{1} \int_{-1}^{1} \int_{-1}^{1} B_e^T(\xi_1, \xi_2, \xi_3) E_e \varepsilon_0(\xi_1, \xi_2, \xi_3) \det(J(\xi_1, \xi_2, \xi_3)) d\xi_1 d\xi_2 d\xi_3$$

Where $\varepsilon_0(\xi_1, \xi_2, \xi_3) = \alpha(T - T_{ref})[1,1,1,0,0,0]^T$

APPENDIX D

VITA

Name: Xiaomeng Tong

Address: 37 XueYuan Rd, Haidian Dist., Beijing, China, 100191

Email: tongxiaomeng1989@gmail.com

Education: Ph.D., Mechanical Eng., Texas A&M University, May, 2018.
            M.S., Mechanical Eng., Beijing University of Aeronautics and
            Astronautics, 2013
            B.S., Mechanical Eng., Nanjing University of Aeronautics and
            Astronautics, 2007

Interest: Professional interest includes research in rotor-bearing system dynamic
            modeling and lubrication modeling with an emphasis on finite element
            method, thermal distortion of bearing and spinning journal, heat
            conduction as well as thermo-fluid dynamics.